UNIVERSITY OF CALIFORNIA,
IRVINE

Spatial Awareness: how Cells Respond and Control Extracellular Matrix Stiffness Topography

DISSERTATION

submitted in partial satisfaction of the requirements
for the degree of

DOCTOR OF PHILOSOPHY

in Biomedical Engineering

by

Abhishek Kurup

Dissertation Committee:
Associate Professor Elliot L. Botvinick, Chair
Associate Professor Lorenzo Valdevit
Assistant Professor Michelle A. Digman
Professor Arthur D. Lander

2015

DEDICATION

To

My parents

without your continuous support mentally, emotionally, and financially, this achievement would not be possible. I thank you for always keeping me grounded and focused, and most importantly, I thank you for always believing in me

"To raise new questions, new possibilities, to regard old problems from a new angle, requires creative imagination and marks real advance in science"
-Albert Einstein

"Live as if you were to die tomorrow. Learn as if you were to live forever"
-Mahatma Gandhi

TABLE OF CONTENTS

LIST OF FIGURES

LIST OF TABLES

ACKNOWLEDGMENTS

I would like to express the deepest appreciation to my committee chair, Professor Elliot Botvinick, whose innovative capacity and focused drive never ceases to amaze. He has been an absolutely wonderful mentor, who helped me grow both as an individual as well as a scientist. He somehow managed to always make himself available when I have needed him, regardless of how late it is, whether it's a weekend or even if he's on vacation, for which I will be ever grateful. Perhaps what I'm most thankful for is Elliot's steadfast belief in his students, which is demonstrated in his constantly encouraging attitude. When I had first met him, I knew nothing about optics. He took me under his wing and made me the scientist I am today. Importantly, he made me someone that I can be proud of. I will truly miss his mentorship, but am happy to gain his friendship.

I would also like to thank my committee members, Professors Arthur Lander, Lorenzo Valdevit and Michelle Digman. Dr. Lander was very influential in my graduate school career both as a professional mentor and as a teacher. He taught me how to critically view published articles, to never take conclusions at face value, and to always look for the bigger systems biology picture. I had the wonderful opportunity to spend a few days with him in our trip to Japan. Our many lengthy discussions provided me direction for my future endeavors. Dr. Valdevit and I worked together for the breast cancer portion of my dissertation. He was vital in providing us with insight on the project and transformed the paper with his results. Dr. Digman was always supportive of my work and very resourceful in her knowledge of microscopy.

I extend my thanks to the Tlsty lab as well. They trained me in 3D acinar cell culture, and oversaw my progress throughout the project Dr. Thea Tlsty was instrumental in exposing the clinical aspect of breast cancer and teaching me that “hitting the wall” is part of the process. A sincere thank you goes to Dr. Philippe Gascard, who worked tirelessly through the submission and review process with us. Another professor who had a profound impact on my dissertation is Dr. Weiss, and I thank him for exposing me to the importance of cell control of it pericellular rigidity.

In addition, a thank you to my lab coworkers for making my PhD journey so much more engaging. They have all, in one way or the other, helped my journey. I was fortunate enough to make strong friendships who pushed me to be a better scientist. A special thanks to Shreyas Ravindranath and Mark Keating, who made major contributions to my dissertation both experimentally as well as intellectually. My diligent undergraduate researchers Tim Tran, Alejandra Turcios, Anthony Pham and Kristen Macneal all played a big role in this dissertation, as well. They also taught me how to mentor different personalities and work with their strengths and weaknesses to achieve my dissertation goals. I also thank Dr. Bhupinder Shergill for our many discussions that kept me sane through the whole process. I would also like to thank lab alumni Drs. Martha Alvarez, Max Kotlarchyk and Samir Shreim, for guiding me through my initial years in the BEAMS lab and teaching me optical tweezers. Additionally, I thank Karen Martin, Linda McCarthy and Ann Fain for going above and beyond to make sure students like me were dealt with fairly and on different occasions took it upon themselves to fix administration issues that were hindering my work.

A big thank you to my family and friends for their continuous support during my dissertation and bearing my frequent social hiatuses. In particular, I want to extend my

sincere gratitude to my parents who immigrated from a perfectly comfortable and stable life in India to the United States in efforts of providing a better future for my brother and me. Fighting through financial and social issues, they stood strong by us and never let our education be interrupted. Through their many sacrifices, this PhD is just as much a story of success for them as it is for me. I also want to thank my brother whose diligence and strong work ethic inspired me to always work harder and longer. This was especially critical in the last year of my dissertation, where I learned to work with a single minded focus. Finally, I want to thank my beautiful fiancé, who has been my rock throughout graduate school. Her constant reminders to stay focused and to never stop trying, helped me process the many failures that come with experiments. She kept my spirits high and stress low. It was easy to get through rough weeks knowing I'd see her at the end of it. Additionally, I want to thank Drs. Rajni Garg and Sunil Kumar. As university professors and family friends, they provided me a unique perspective that helped me stick it out through the "hill" phase of the PhD.

Last but not least, I want to thank my undergraduate advisor Dr. Joyce Keyak, who guided me away from the M.S. track and towards the PhD track. This was single-handedly one of the most important decision of my life. And I'll always be in her debt for the right nudge at the right time.

Financial support for this work was provided by NSF Physical and Engineering Sciences in Oncology Grant CMMI-1233697, National Institute of Health (NIH)/National Institute of Child Health and Human Development (NICHD) T32 Pre-doctoral Training Grant HD060555-05, NIH/National Heart, Lung, and Blood Institute (NHLBI) T32 pre-doctoral Training Grant HL116270, and the Laser Microbeam and Medical Program, a National

Biomedical Technology Resource (NIH P41-EB015890). The content is solely the responsibility of the authors and does not necessarily represent the official views of the NCI, NIH, NSF, NICHD or NHLBI. This work also does not necessarily represent the official views of publishers where portions of this dissertation have been published/accepted. I thank Elsevier for grating me permission to use copyrighted material for this dissertation in Chapter 2. Chapter 3 of this work is currently in review at *Scientific Reports* and Chapter 4 has been submitted to *Nature Communications*, but not yet accepted. No changes have been made in this dissertation from the original manuscripts. Both journals are open access under the creative commons license allowing anyone to use the copyrighted material as long as appropriate credit is provided and it is indicated whether changes were made.

CURRICULUM VITAE

EDUCATION

University of California, Irvine, CA

Ph.D. Candidate, Biomedical Engineering – GPA: 3.97 September 2015

Awards: T-32 pre-doctoral training grant (NIH/NICHD), 2013-2014; Travel award for Global Science Week Conference, Japan, 2013; Graduate student travel grant, 2015;

M.S. Biomedical Engineering– GPA: 3.95 2013

Awards: Graduate student researcher aid, 2011; MCSB research training fellowship, 2010; MCSB best lab notebook, 2010;

B.S. Biomedical Engineering, minor in Material Science – Engineering GPA: 3.484 2010

Awards: Dean's Honor List, 2009-2010;

DESIGN & ENGINEERING PROJECTS

Project Development: Shear Gradient Device

Jun 2014 – Mar 2015

- Directed team of undergraduates to redesign shear gradient device to include multi-well plate functionality.
- Fabricated multi-well adaptor with rotating element for NEMA stepper motor using SolidWorks and 3D printer.
- Tracked team progress to ensure project milestones were completed on time and within budget.
- Conducted controlled validation testing for experimental procedures.

Technology Automation: Active Microrheology System (AMR)

Jun 2014 – Mar 2015

- Devised image processing algorithms for centroid detection and intensity line profiling coupled with motor control for piezo and stepper stage movement in LabVIEW to map matrix stiffness around cells in real time.
- Coordinated all phases of development including code design, implementation, and experimental testing to achieve a 10-fold improvement in measurements.
- Implemented automated AMR system to study mechanical interactions between cells and their extra cellular matrix in migration, differentiation, homeostasis and cancer.
- Conducted optical path design, alignment, and troubleshooting for optical tweezers.

Medical Device Design: Novel Basket Sheath and Controller for Ureteroscopy

Apr – Jun 2012

- Conceived medical device to reduce operation time for Ureteroscopy procedures.
- Chief SolidWorks designer of 6 member team comprised of graduate students.

Design and Build: Customized On-Stage Incubator for Inverted Microscope

Jun 2011 – Oct 2011

- Designed on-stage incubation chamber for long term microscopy experiments.
- Engineered incubator using polycarbonate sheets and screws, silicone adhesive mats, ceramic strip heaters coupled with heat sinks, thermocouple, P.I.D. temperature controller, and a 5% CO_2 gas housing through an Erlenmeyer flask for humidified gas exchange.
- Performed iterative measurement and analysis for validation and standardization

RESEARCH EXPERIENCE

Graduate Researcher
Jul 2011 – Sep 2015
Department of Biomedical Engineering, BEAMS Lab, UC Irvine

- Investigated the progression of invasive cancer as a result of HER2 signaling in combination with crosslinking on mammary ducts grown within natural hydrogels via phenotype classification, immunofluorescence techniques, finite element analysis, and western blots.
- Created a LabVIEW-mediated automated active microrheology system to map pericellular rigidity in real time between cells and their ECM during migration, differentiation, homeostasis and cancer.
- Discovered that MT1-MMP deficient mesenchymal stem cells lost their ability to tune local ECM stiffness in order to direct differentiation down osteoblast lineages.
- Assessed protease-mediated degradation of Geltrex in time.
- Quantified complex shear modulus of fibrin polymerized with platelet rich and platelet poor plasma to study wound healing.
- Collaborations: *Weiss Lab* (University of Michigan), *Tlsty Lab* (UC San Francisco), *Valdevit Lab* (UC Irvine), *Trevigen Inc.* (Gaithersburg, Maryland), *Lam Lab* (Georgia Tech)

Graduate Researcher Rotation
Jan – Mar 2011
Department of Pathology, Monuki Laboratory, UC Irvine

- Trained in extracting mice embryos and harvesting postnatal mouse brains.
- Designed cost-effective apparatus to deform harvested mouse brains for OCT imaging.

Graduate Researcher Rotation
Mar – Dec 2010
UCI Department of Biomedical Engineering, BEAMS Lab, UC Irvine

- Developed a video particle tracking software in MATLAB.
- Formulated a LabVIEW routine to control a microscope stepper stage and piezo stage with micrometer and nanometer accuracy, respectively.

PROFESSIONAL EXPERIENCE

Mentor – CardioStart
Jun – Aug 2014
Edwards Lifescience Center for Advanced Cardiovascular Technology (ELCACT), UC Irvine

- Formulated 6 week program for high school students introducing 3D cell culture, SolidWorks design, 3D printing, and cell morphology quantification via ImageJ.

Manuscript Reviewer
Apr 2013 – Nov 2014
Biomedical Optics Express Journal

- Critiqued scientific articles and provide thorough feedback on the strengths and weaknesses of the experimental design and analysis methods.

Program Coordinator – CardioStart
Apr – Sep 2013
ELCACT, UC Irvine

- Developed a productive and stimulating program for the education and training of young (high school/college) scientists involving guest lectures, group discussions, and mentored research projects.
- Discussed program layout and logistics in weekly meetings with the Center's administrator, Miss Ann Fain, and/or Center chair, Dr. Steve George.
- Pioneered program agenda and arranged for guest lectures in topics like "Making an Effective Poster Presentation," "Ethics and Safety in Research, Literature Research Strategies," and "Maintaining a Good Lab Notebook."
- Conducted workshop on scientific lab notebook etiquette.

Undergraduate Supervisor
Nov 2013 – Feb 2014
ELCACT, UC Irvine

- Supervised undergraduates from different labs to ensure daily laboratory tasks in the shared facility were completed bi-weekly.

Laboratory Instructor – "Single Cell" Course
Jul 2013
Cold Spring Harbor Laboratory, New York

- Charted a 2-day laboratory workshop on 3D durotaxis of fibroblasts in fibrin with and without stiffness gradients.
- Trained chemists and microbiologists ranging from graduate students to professors in making fluorescent fibrin gels with embedded fibroblasts and tracking stained cells with confocal microscopy.

Teaching Assistant – Cell and Molecular Engineering Course
Jan – Apr 2012
Department of Biomedical Engineering, UC Irvine

- Led weekly discussion sections for a class of 60 students.
- Organized extra sessions to help students review before the midterm and final.

Tutor – Mathematical and Computational Systems Biology Boot Camp
Aug – Sep 2011
Center of Complex Systems Biology, UC Irvine

- Mentored first year graduate student in critically reviewing assigned journal article for oral presentation.
- Trained mentee in presenting effective oral presentation.

PUBLISHED ABSTRACTS

Botvinick, E., Alvarez, M., **Kurup, A.**, Keating, M. "Mapping Mechanical Properties of The Extra Cellular Matrix Surrounding Cells Cultured in 3D." *Biophysical Journal*. 2014.106(2):235a

Kurup, A., Botvinick, E. "Mapping Matrix Mechanics in 3D to Study the Role of Stiffness in Breast Tumor Progression." *Cancer Research*. 2013.73(8)

PUBLICATIONS

Kurup, A. & Keating, M., Alvarez, M., Botvinick, E. "Method to measure pericellular stiffness in natural extracellular matrices." *PNAS*. [Submitted]

Kurup, A., Tran, T., Keating, M., Gascard, P, Valdevit, L., Tlsty, T., Botvinick, E. "Novel Insights from 3D Models: the Pivotal Role of Physical Symmetry in Epithelial Organization." *Scientific Reports*. [In Review]

Tang, Y., Rowe, G., Botvinick, E.L., **Kurup, A**., et. al. "MT1-MMP-Dependent Control of Skeletal Stem Cell Commitment via a β-1 integrin/YAP/TAZ Signaling Axis." *Dev Cell*. 2013

Pandey, A., **Kurup, A**., et. al. "Cancer Testes Antigens in Breast Cancer: Biological Role, Regulation, and Therapeutic Applicability." *Int Rev Immunol*. 2012.

ORAL PRESENTATIONS

Kurup, A., Tlsty, T., Botvinick, E. "*The Third Dimension: Mechanics and Mammary Morphogenesis*." Tissue Engineering and Regenerative Medicine International Society (TERMIS). Washington, DC. December 2014.

Kurup, A. & Keating, M., Alvarez, M., Botvinick E. "*Quantifying Change in Stiffness Heterogeneity in 3D Around Cells Embedded in Natural ECMs Over Time*." International Society of Optics Photonics: Nanoscience + Engineering. San Diego, CA. August 2014.

Kurup, A., Yu, C., Tlsty, T., Botvinick, E. "*ECM Stiffening Potentiates ErbB2-Mediated Invasion as Observed in 3D Scaffolds of Identical Composition*." Global Science Week. Tsukuba, Japan. October 2013.

Alvarez, M., **Kurup, A**., Keating, M, Botvinick E. "*Automatic Optical Tweezers Based Active Microrheology*." Biomedical Engineering Society Annual Conference 2013. Seattle, WA. September 2013.

Kurup, A., Yu, C., Tlsty, T., Botvinick, E. "*ECM Stiffening Potentiates ErbB2-Mediated Invasion as Observed in 3D Scaffolds of Identical Composition*." 14th UC Systemwide Bioengineering Symposium. San Diego, CA. June 2013.

Kurup, A., Tlsty, T., Botvinick, E. "*Mapping Matrix Mechanics in 3D to Study the Role of Stiffness in Breast Tumor Progression*." AACR Annual Meeting. Washington, DC. April 2012.

Kurup, A., Botvinick, E. "*Using Active Microrheology to Map Matrix Mechanics in 3D*." BMES Annual Meeting. Atlanta, GA. October 2012.

Kurup, A., Botvinick, E. "*Using Active Microrheology to Map Matrix Mechanics in 3D*." UC Systemwide Bioengineering Symposium. Berkeley, CA. June 2012.

POSTER PRESENTATIONS

Kurup, A., Tlsty, T., Botvinick, E. "*The Third Dimension: Mechanics and Mammary Morphogenesis*." UC Systemwide Bioengineering Symposium. Irvine, CA. June 2014

Kurup, A. & Keating, M. Alvarez, M., Botvinick, E. "*Quantifying Change in Stiffness Heterogeneity in 3D Around Cells Embedded in Natural ECMs*." UC Systemwide Bioengineering Symposium. Irvine, CA. June 2014.

Kurup, A., Yu, C., Tlsty, T., Botvinick, E. "*ECM Stiffening Potentiates ErbB2-Mediated Invasion as Observed in 3D Scaffolds of Identical Composition*." Biomedical Engineering Society Annual Conference 2013. Seattle, WA. September 2013.

Kurup, A., Yu, C., Tlsty, T., Botvinick, E. "*ECM Stiffening Potentiates ErbB2-Mediated Invasion as Observed in 3D Scaffolds of Identical Composition*." PS-OC NIH Site Visit. Salk Institute, San Diego, CA. September 2013.

Kurup, A., Yu, C., Tlsty, T., Botvinick, E. "*ECM Stiffening Potentiates ErbB2-Mediated Invasion as Observed in 3D Scaffolds of Identical Composition*." PS-OC 4th Annual Meeting. Phoenix, AZ. April 2013.

Weidling, J., **Kurup, A.**, Shreim S., Alvarez-Elizondo, M., Botvinick. E. "*Characterizing the Mechanical Relationship Between Cells and ECM Using Laser Tweezer Active Microrheology in 3D Hydrogels*." Edwards Lifesciences Center Open House. Irvine, CA. October 2011.

AFFILIATIONS

American Association of Cancer Research (AACR), Biomedical Engineering Society (BMES), International Society of Optics and Photonics (SPIE), Orange County Science Fair

MENTEES

PhD Rotational Students
Shreyas Raj Ravindranth (Spring 2012), Renu Jayakrishnan (Spring 2012), Mark Keating (Fall 2013)
Undergraduate Students
Kevin Vu (Fall 2011 – Fall 2012), Kristen MacNeal (Winter 2012 – Spring 2013), Horacio Michael Estabridis (Fall 2012, Mark Keating (Winter 2012-Spring 2013), Thi Nha Timothy Tran (Summer 2013 – Summer 2015) , Anthony Pham (Summer 2013-Summer 2015)

CERTIFICATION & TRAINING

Mammalian Cell Culture; HIPAA 101, Information Security; Bloodborne Pathogens; Fume Hood Safety; Fire Extinguisher Safety; Hazardous Waste; Formaldehyde Safety; Compressed Gas Safety; Shipping Hazardous Materials: Dry Ice; UC Ethical Values and Conduct; Laboratory Core Safety; Laser Safety; Radiation Safety; TANGO (Teaching Assistant & New Graduate student Orientation) to Safety;

MISCELLANEOUS

Skills:	MATLAB, LabVIEW, Mathematica, ImageJ, SolidWorks, Origin, LaTex, Basic Java, 3D Printing with MakerBot, Photoshop
Mechanical:	Active/Passive Microrheology, Parallel Plate Rheology, Tensile/Compression Test, Fatigue Test, 3-point Flexural Test, Impact Test, Rockwell Hardness Test.
Cell Culture:	Aseptic techniques (BSL-2), Mammalian cell culture (stem, breast, fibroblast, endothelial, epithelial), 3D cell culture, Hydrogels (Matrigel, Collagen, Fibrin, Gelatin), PDMS.
Microscopy:	Fluorescence and Reflection Confocal, Multi-photon. Familiar with STICS, RICS, SHG and FLIM
Laboratory:	Western Blot, SDS-PAGE, qPCR. Working knowledge of RNA Isolation, cDNA synthesis, IR Spec, Mass Spec, NMR, Liquid Chromatography, and FACS.
Activities:	Co-captain of team performing in *I Just Want to Dance* charity show (2014). Starred on NBC's *Superstars of Dance* (2009), *Good Morning America* (2009) and *E! Red Carpe*t (2009). Captain of UC Irvine *Bollywood Dance* Team (2006-2007).

ABSTRACT OF THE DISSERTATION

Spatial awareness: how cells respond and control extra cellular matrix stiffness topography

By

Abhishek Kurup

Doctor of Philosophy in Biomedical Engineering

University of California, Irvine, 2015

Professor Elliot L. Botvinick, Chair

The mechanical properties of the extracellular matrix (ECM) have shown to regulate key cellular processes. However, current tools studying cell-ECM biophysical interactions revolve around cell-mediated traction forces, which, as I will show, are not appropriate in natural matrices due to matrix remodeling. I used active microrheology (AMR) to, instead, measure ECM stiffness in order to quantify these interactions in various cell-ECM systems.

In the first system, I evaluated a commonly used 3D cell-culture method in breast cancer research. I show that this model produces a large physical asymmetry in ECM stiffness, which resulted in altered cellular morphology, adhesion-mediated signaling, and phenotype. Importantly, a hallmark result obtained in this culture method was not repeatable once the asymmetry was removed, highlighting the importance of considering biophysical interactions in cell-culture models.

In the second system, my work, in collaboration with Dr. Stephen Weiss, led to the discovery that stem cells are not passive recipients of ECM stiffness signals as previously thought.

Rather they can deliberately alter local (pericellular) stiffness with matrix metalloproteinases as a control for cellular functions. In particular, we found that skeletal stem cells competent in their ability to degrade collagen, increased pericellular stiffness via matrix remodeling to activate β1 integrin signaling pathways and thus controlled their own lineage commitment to osteogenic fates. Cells without the ability to degrade their local matrix lost this functionality and were restricted in lineage commitment to adipogenic or chondrogenic fates.

For the third system, I quantified the contributions of cell contractility and matrix metalloproteinases in matrix remodeling for developing a normal mechanical topography in smooth muscle cells. I also provide evidence that it is the distribution of pericellular stiffness rather than a bulk value that instructs cellular behavior. In order to accomplish this task, I automated the AMR system (aAMR) for a tenfold decrease in measurement time. Importantly, aAMR reduces the complexity of AMR to a few mouse clicks, can create stiffness maps over large distances and provides metrics to assess the distribution of stiffness in the pericellular space within the volume of a natural, fibrous hydrogel.

Chapter 1

Introduction

1.1 Overview and significance

An important aspect of the physical component of the extracellular matrix (ECM), and a prime focus of this dissertation, is the biophysical interaction between the cell and ECM. However, current tools studying cell-ECM biophysical interactions are focused on cell-mediated traction forces, but do not account for matrix remodeling and degradation. The focus of this dissertation is to *quantify the distribution of ECM stiffness, cell-mediated changes to it, and the resultant effects on cellular behavior*. In **Chapter 2**, I describe microrheology tools that enable local measurements of ECM stiffness as a readout of cell-ECM interactions. Specifically, I first studied how cell-mediated ECM stiffness is an important control point for driving stem cell differentiation. In **Chapter 3**, I use microrheology to study the physical asymmetry produced in the overlay protocol, which is commonly used for *in vitro* models of breast cancer research, and its dominant effect in observed phenotype. The combined work presented in **Chapter 2** and **Chapter 3** underscored the importance of incorporating biophysical interactions in cell culture models to gain a systems understanding of cell-ECM interactions. But, available microrheology tools are too slow and cumbersome to test complex mechanical hypothesis. Thus, in **Chapter 4**, I detail improved microrheology methods to achieve this task around cells within the volume of a type 1 Collagen gel.

My thesis provides four main contributions. The first is establishing pericellular stiffness as a readout for cell-ECM interactions. The second is evidence that stem cells can remodel their

matrix as a control to drive their own differentiation. The third, for the breast cancer research community, is to not discount the role of ECM mechanics when choosing *in vitro* 3D culture models. The fourth, to the larger biophysics community, is aAMR, a tool that can finally quantify cell-ECM biophysical interactions in the volume of a natural, fibrous hydrogel in a manner conducive to testing cellular processes like migration, differentiation, and matrix remodeling.

1.2 The extra cellular matrix

The ECM is a major component of the cellular microenvironment comprised of a variety of proteins and proteoglycans with diverse functionality and structure that provide both chemical and physical context to cells (**Fig. 1.1**) [1]. It is involved in the most basic cellular processes like growth, migration, and apoptosis[2] as well as complex hierarchical ones like mammary gland development[4], maturation of the nervous system[5], and development of limbs[6]. Chemically, the ECM can regulate growth factors presented to cells and thus provide context to cells. For instance, by binding to certain growth factors, the ECM can create concentration gradients such as those found in bone morphogenic protein (BMP) [7]. Conversely, by not binding to other proteins, the ECM can selectively bias cellular process, a requirement for directing development[1]. Physically, the ECM is involved in scaffolding, adhesion, and force transmission[2]. In addition, it can both present a physical barrier to impede migration[8] while providing fibrous tracks to facilitate migration[9]. Physical confinement by the ECM has been shown to activate YAP/TAZ mediated transcription[10] and alter actin cytoskeleton distribution[11]. Cells can regulate their degree of confinement by degrading the local ECM with matrix metalloproteinases (MMPs). Degradation in this manner is important in both remodeling as well as creating functional ECM fragments[12]. The mechanical

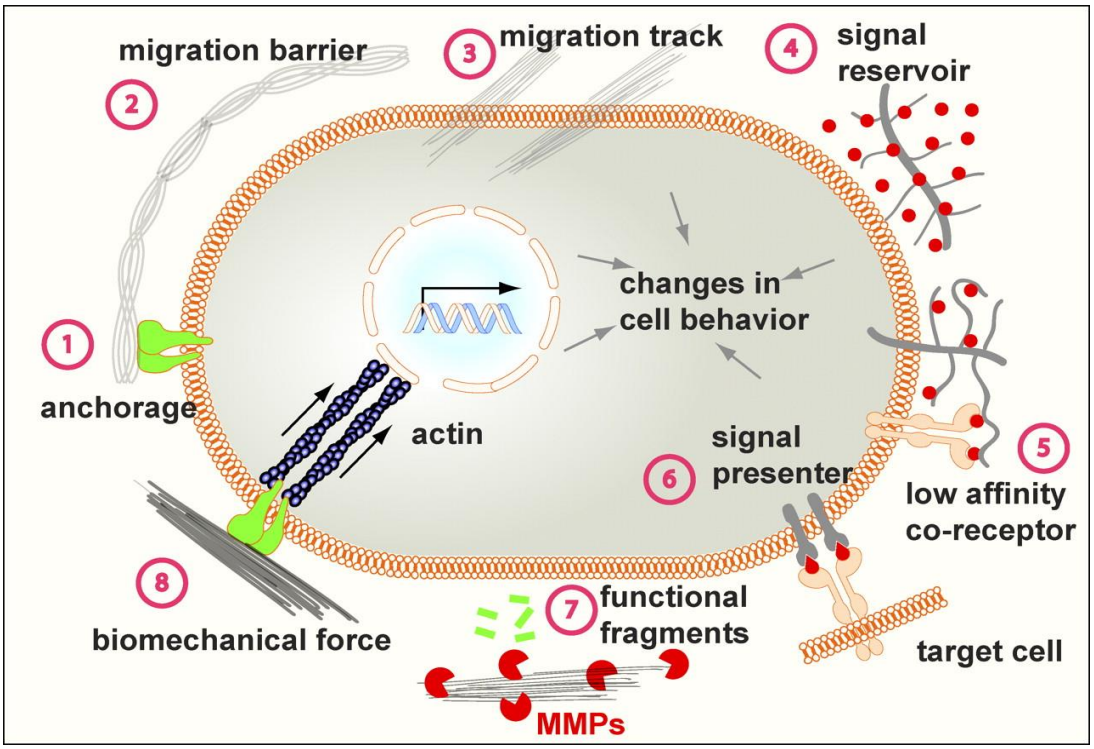

Figure 1.1: *Interactions between the cell and extra cellular matrix. The extra cellular matrix provides many biophysical and biochemical cues that are important for cellular processe*[1].

changes related with degradation and remodeling, namely ECM stiffness, provide an important feedback loop for cellular processes.

That ECM stiffness plays an implicit role in disease was realized with the observation that diseased tissues are considerably stiffer compared to their normal counterpart[13]. In fact, mammographic density, which is the ratio of protein and connective (stiff) tissue concentration to fatty (soft) tissue, correlates positively with the risk of developing breast cancer[14]. *In vitro*, ECM stiffness has been shown to instruct a range of cellular processes ranging from development to metastasis[15]. For example, human mesenchymal stem cells were found to differentiate preferentially into osteocytes when cultured atop stiffer ECM and into neurons on compliant ones[16]. Similarly, stiff substrates have even been shown to drive metastasis in breast cancers as compared to softer ones[17]. These findings highlight the importance of studying ECM mechanics

to understand cellular response in physiological and pathological conditions. In the next section, I will describe how cells gauge the mechanical properties of the ECM

1.3 Mechanotransduction

Cells sense their local ECM stiffness via mechanical linkers called integrins, which are heterodimeric transmembrane glycoproteins[18]. The extracellular end of the integrin recognizes specific ECM components[19] while the intercellular end is connected to the actin cytoskeleton by linker proteins, thus creating a mechanical bridge across the plasma membrane. Integrins cluster in response to ECM mechanics and generate chemical responses by activating downstream pathways in a complex feedback process called mechanotransduction[13]. For example, applying transient tensile forces on smooth muscle cells can upregulate the cytokine TGF-β, whereas constant tensile force can upregulate TGF-β and Collagen I production[20]. Likewise, static and dynamic ECM loading in fibroblasts results in upregulation of different MMPs[21]. External tensile force can also alter cellular expression of signaling molecules such as Wnt, β-catenin, Stat1/3, and others[13].

Integrin activation is both inside-out and outside-in. Inside out activation requires interaction with intercellular protein talin[22]. The α-subunit of the integrin is believed to sterically hinder the β tail[23] and both are in a kinked position[24] before activation. Interaction of the β tail with talin leads to a conformational change in the integrin structure releasing it from its kinked position and priming it for ligand binding[24]. Talin also activates via conformational change that opens docking sites for vinculin, which in turns binds to actin, thus completing the link between integrins and actin[2]. Outside-in signaling begin with integrins binding to ECM proteins. As cells contract, the integrin link feels tension depending on the compliance of the ECM to which it is

anchored. Increased forced, in this manner, on the actin cytoskeleton results in increased assembly of focal adhesion complexes (FAs), creating larger and stronger adhesions[15]. In fact, exposure to stiff 2D substrates has been documented to result in increased FA size[25].

FAs are macromolecular complexes that strengthen the link between the ECM and the cellular cytoskeleton and are initiated by integrin clustering[26]. FAs are also responsible for coordinating mechanotransduction through protein-protein interaction and signaling cascades[27]. Focal adhesion kinase (FAK) signaling is a major component of FAs and is closely related to integrin clustering[13]. Integrin clustering leads to FAK auto phosphorylation at tyrosine 397 (Y397) and thereby its activation[28]. It is important to point out that the complete details of integrin activation and ordering of events are not known. For example, only in 2012, it was found that while FAK is necessary for talin recruitment in nascent FAs, talin is necessary for FAK recruitment in mature FAs[29]. Nevertheless, FAK phosphorylated at Y397 creates a high affinity site for binding with Src proteins to form a FAK-Src complex[30]. However, evidence suggests that Src may also be able to bind FAK independent of FAK phosphorylated at Y397[31]. Upon binding, Src trans-phosphorylates FAK at multiple sites including Y576 and Y577, which elevate the Src-FAK complex to its highest catalytic state and unfolds binding sites for scaffold and adaptor proteins like paxillin and CAS[30]. This process leads to downstream activation of Rho-family of GTPases: Rac, Ras and Rho[22]. Rac activation leads to actin polymerization[32] and activation of MMPs[28]. Activation of Ras induces the extra cellular signal-related kinase (ERK)/ mitogen-activated protein kinase (MAPK) pathway, which stimulates mitogenesis, proliferation, and MMP secretion[28]. Rho is a regulator of adhesion and cytoskeleton dynamics, cellular contractility, proliferation and migration[26]. Rho can also regulate localized MMP secretion for matrix remodeling[33]. Through its ability to activate Rho-associated kinase (ROCK), Rho can also inhibit myosin light chain

phosphatase (MLCP) and activate myosin light chain kinase (MLCK), thereby increasing actomyosin contractility[26], an important factor of cell-mediated traction forces on the ECM. Like ROCK, ERK also activates MLCK, leading to heightened actomyosin contractility[22]. In addition, the FAK-Src complex can activate Phosphatidylinositol 3-kinase (PI3K) which signals downstream to second messenger phosphatidlyinositol-3,4,5-trisphosphate (PIP3). PIP3 activates the serine/threonine-specific protein kinase Akt[28], which is a key factor in regulation of proliferation, survival, and cell/colony size[34].

By controlling these essential pathways and more, FAs can regulate many critical processes and generate a multitude of responses from the cell. It is not surprising that cell-ECM mechanical interactions are critical in sculpting the organism during embryogenesis and organ development[26]. In particular, these interactions play a major role in tensional homeostasis, which is a dynamic force balance maintained between the cells and ECM. Tensional homeostasis was first documented less than two decades ago when tensional force monitors on hydrogels seeded with fibroblasts recorded cell-mediated forces responding opposite to external increase or decrease of force[21]. This study underlined the ability of cells to monitor ECM elasticity and respond with compensatory contractile forces such that a defined level of internal cellular tension is maintained. Cells can also utilize MMPs, both tethered and secreted, to tailor ECM stiffness, although the full extent of their role in tensional homeostasis has not been well established. Recent studies have shown that large increases in ECM stiffness, as is found in desmoplastic tissue[13], can cause abnormally high intercellular tension resulting in aberrant cellular behavior[35] and even disease progression[15]. Breast cancer, in particular, has strongly been linked to ECM mechanics[17].

1.4 Breast Cancer

Breast malignancy is characterized by a significant increase in mammary gland tension as a result of altered vasculature, tumor growth, and stiffening of ECM due to fibrosis[3]. In fact, the stroma in a malignant lesion is often desmoplastic and presents a densely packed ECM[36]. Tumor stroma also suffers from a dramatic reduction in adipocyte volume, aberrant vasculature, immune response, and invasion[36]. Even in normal tissue, mammographic density, and thereby matrix mechanics, is a strong independent factor for the risk of developing breast cancer[37]. Women with high mammographic density are 4-6 fold more likely to develop tumor[38]. Further supporting the critical role of ECM stiffness in breast cancer, *in vitro* culture of mammary epithelial cells (MECs) has found them to be more proliferative in stiffer matrices and upregulate genes implicated in human breast carcinoma[35].

Immortalized MEC lines, such as MCF10As are often used to study tumor progression *in vitro* because of their ability to recapitulate physiological conditions. When grown in a three-dimension reconstituted basement membrane culture, such as Matrigel, these cells adopt a phenotype similar to the hollow, growth arrested, and polarized spheroids called acini found within the mammary gland[39]. Even the process of the acinar formation *in vitro* is similar to that found *in vivo*. The cultures start as single cell suspensions, proliferate into masses of cells, create apico-basal polarity, undergo apoptosis in the center, create a hollow lumen and reach a growth-arrested phase (**Fig 1.2**) [40]. Loss of polarity, reinitiation of proliferation, and filling of the hollow lumen are all markers of a tumor phenotype[17]. A few polarization markers are listed in **Table 1.1**. Most integrins in epithelial cells are β1 containing heterodimers[23]. $\alpha_1\beta1$, $\alpha_2\beta1$, $\alpha_6\beta1$, and $\alpha_3\beta1$ all bind to collagen and laminin[23]. $\alpha_6\beta1$ is important in early epithelial differentiation and β4 integrins play an important role in epithelial cells for anchoring to the underlying tissue and polarization[23].

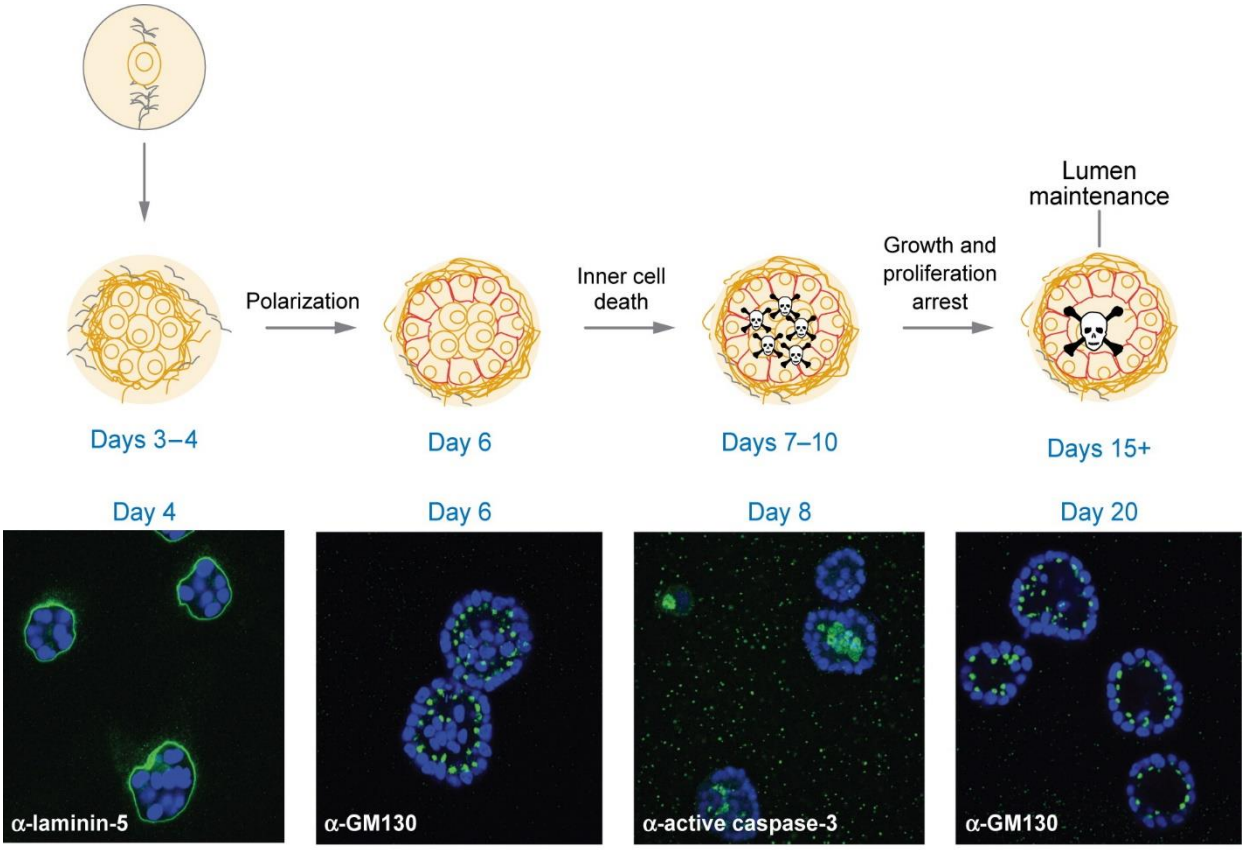

Hebner C, et al. 2008.
Annu. Rev. Pathol. Mech. Dis. 3:313–39

Figure 1.2*: Mammary epithelial cell morphogenesis into acinar structures in reduced basement membrane (rBM). Cells culture in rBM, such as Matrigel, start as single cells and over the course of 2 weeks form hollow acini (top). Polarization markers Laminin and GM130 are shown. Active caspace-3 expression represents apoptosis. Adapted from*[3].

In 2005, the Weaver lab showed that MCF10A acini assumed an increasingly transformed phenotype when cultured in matrices of increasing stiffness[17]. Later studies suggested that matrix stiffness correlation with tumor progression is mediated by β1 and β4 integrin signaling[41]. In fact, blocking β1 activity in malignant acini rescued the normal phenotype[41]. Later, another hallmark paper[41] utilized MCF10A chimeras that could be transformed by a synthetic ligand that forced activation of the epidermal growth factor receptor tyrosine kinase ErbB2[42]. The study found that a significant increase in invasive colonies was only observed when the ErbB2 pathway was activated

in an already cross-linked gel, but not in ErbB2 activation or matrix crosslinking conditions alone[41]. These results suggest that changes in matrix stiffness can alter mechanotransduction and sensitize cells towards the malignant phenotype. Nevertheless, most 3D culture studies relating to MECs are conducted with the overlay protocol which may present acini with non-physiological mechanics as I will show as part of this dissertation.

Table 1.1: Markers of polarity in mammary epithelial cells[23, 39, 43].

Protein markers	***Location of expression***
α6 integrin, β1 integrin, β-catenin	Baso-lateral
GM130, Endoplasmic Reticulum	Apical
Laminin V, Collagen IV, β4 integrin	Basal
E-Cadherin, Tight Junctions	Lateral

1.4 References

1. Lu, P., Takai, K., Weaver, V.M. & Werb, Z. Extracellular matrix degradation and remodeling in development and disease. *Cold Spring Harbor perspectives in biology* **3** (2011).
2. Humphrey, J.D., Dufresne, E.R. & Schwartz, M.A. Mechanotransduction and extracellular matrix homeostasis. *Nature reviews. Molecular cell biology* **15**, 802-812 (2014).
3. Hebner, C., Weaver, V.M. & Debnath, J. Modeling morphogenesis and oncogenesis in three-dimensional breast epithelial cultures. *Annu Rev Pathol* **3**, 313-339 (2008).
4. Fata, J.E., Werb, Z. & Bissell, M.J. Regulation of mammary gland branching morphogenesis by the extracellular matrix and its remodeling enzymes. *Breast cancer research : BCR* **6**, 1-11 (2004).
5. Zimmermann, D.R. & Dours-Zimmermann, M.T. Extracellular matrix of the central nervous system: from neglect to challenge. *Histochem. Cell Biol.* **130**, 635-653 (2008).
6. Bastow, E.R. *et al.* Hyaluronan synthesis and degradation in cartilage and bone. *Cell. Mol. Life Sci.* **65**, 395-413 (2008).
7. Rozario, T. & DeSimone, D.W. The extracellular matrix in development and morphogenesis: a dynamic view. *Dev. Biol.* **341**, 126-140 (2010).
8. Charras, G. & Sahai, E. Physical influences of the extracellular environment on cell migration. *Nature reviews. Molecular cell biology* **15**, 813-824 (2014).
9. Wolf, K. *et al.* Compensation mechanism in tumor cell migration: mesenchymal-amoeboid transition after blocking of pericellular proteolysis. *J. Cell Biol.* **160**, 267-277 (2003).
10. Dupont, S. *et al.* Role of YAP/TAZ in mechanotransduction. *Nature* **474**, 179-183.
11. Balzer, E.M. *et al.* Physical confinement alters tumor cell adhesion and migration phenotypes. *FASEB J.* **26**, 4045-4056 (2012).
12. Rhodes, J.M. & Simons, M. The extracellular matrix and blood vessel formation: not just a scaffold. *Journal of cellular and molecular medicine* **11**, 176-205 (2007).

13. Lopez, J.I., Mouw, J.K. & Weaver, V.M. Biomechanical regulation of cell orientation and fate. *Oncogene* **27**, 6981-6993 (2008).
14. Martin, L.J. & Boyd, N.F. Mammographic density. Potential mechanisms of breast cancer risk associated with mammographic density: hypotheses based on epidemiological evidence. *Breast Cancer Research* **10**, 201.
15. Provenzano, P.P. & Keely, P.J. Mechanical signaling through the cytoskeleton regulates cell proliferation by coordinated focal adhesion and Rho GTPase signaling. *J. Cell Sci.* **124**, 1195-1205 (2011).
16. Keung, A.J., Kumar, S. & Schaffer, D.V. Presentation Counts: Microenvironmental Regulation of Stem Cells by Biophysical and Material Cues. *Annu. Rev. Cell Dev. Biol.* **26**, 533-556.
17. Paszek, M.J. *et al.* Tensional homeostasis and the malignant phenotype. *Cancer Cell* **8**, 241-254 (2005).
18. Katsumi, A., Orr, A.W., Tzima, E. & Schwartz, M.A. Integrins in mechanotransduction. *J. Biol. Chem.* **279**, 12001-12004 (2004).
19. Yamada, K.M., Pankov, R. & Cukierman, E. Dimensions and dynamics in integrin function. *Braz. J. Med. Biol. Res.* **36**.
20. Gutierrez, J.A. & Perr, H.A. Mechanical stretch modulates TGF-beta1 and alpha1(I) collagen expression in fetal human intestinal smooth muscle cells. *Am. J. Physiol.* **277**, G1074-1080 (1999).
21. Brown, R.A., Prajapati, R., McGrouther, D.A., Yannas, I.V. & Eastwood, M. Tensional homeostasis in dermal fibroblasts: mechanical responses to mechanical loading in three-dimensional substrates. *J. Cell. Physiol.* **175**, 323-332 (1998).
22. Schedin, P. & Keely, P.J. Mammary gland ECM remodeling, stiffness, and mechanosignaling in normal development and tumor progression. *Cold Spring Harbor perspectives in biology* **3**, a003228 (2011).
23. Matlin, K.S., Haus, B. & Zuk, A. Integrins in epithelial cell polarity: using antibodies to analyze adhesive function and morphogenesis. *Methods* **30**, 235-246 (2003).
24. Askari, J.A., Buckley, P.A., Mould, A.P. & Humphries, M.J. Linking integrin conformation to function. *J. Cell Sci.* **122**, 165-170 (2009).
25. Engler, A.J., Shamik, Sweeney, H.L. & Discher, D.E. Matrix Elasticity Directs Stem Cell Lineage Specification. *Cell* **126**, 677-689.
26. Kumar, S. & Weaver, V.M. Mechanics, malignancy, and metastasis: the force journey of a tumor cell. *Cancer Metast Rev* **28**, 113-127 (2009).
27. Wozniak, M.A., Modzelewska, K., Kwong, L. & Keely, P.J. Focal adhesion regulation of cell behavior. *Biochim. Biophys. Acta* **1692**, 103-119.
28. Guarino, M. Src signaling in cancer invasion. *J. Cell. Physiol.* **223**, 14-26.
29. Serrels, B. & Frame, M.C. FAK and talin: who is taking whom to the integrin engagement party? *J. Cell Biol.* **196**, 185-187 (2012).
30. Mitra, S.K. & Schlaepfer, D.D. Integrin-regulated FAK-Src signaling in normal and cancer cells. *Curr. Opin. Cell Biol.* **18**, 516-523 (2006).
31. McLean, G.W., Fincham, V.J. & Frame, M.C. v-Src induces tyrosine phosphorylation of focal adhesion kinase independently of tyrosine 397 and formation of a complex with Src. *J. Biol. Chem.* **275**, 23333-23339 (2000).
32. Abreu, M.T. *et al.* Gab2 regulates cytoskeletal organization and migration of mammary epithelial cells by modulating RhoA activation. *Mol. Biol. Cell* **22**, 105-116.
33. Wolf, K. *et al.* Multi-step pericellular proteolysis controls the transition from individual to collective cancer cell invasion. *Nature Cell Biology* **9**, 893-904.
34. Debnath, J. *et al.* The role of apoptosis in creating and maintaining luminal space within normal and oncogene-expressing mammary acini. *Cell* **111**, 29-40 (2002).
35. Provenzano, P.P., Inman, D.R., Eliceiri, K.W. & Keely, P.J. Matrix density-induced mechanoregulation of breast cell phenotype, signaling and gene expression through a FAK-ERK linkage. *Oncogene* **28**, 4326-4343 (2009).
36. DeFilippis, R.A. *et al.* CD36 repression activates a multicellular stromal program shared by high mammographic density and tumor tissues. *Cancer discovery* **2**, 826-839.
37. Vachon, C.M. *et al.* Mammographic density, breast cancer risk and risk prediction. *Breast cancer research : BCR* **9**, 217 (2007).
38. Byrne, C. *et al.* Mammographic Features and Breast Cancer Risk: Effects With Time, Age, and Menopause Status.
39. Debnath, J., Muthuswamy, S.K. & Brugge, J.S. Morphogenesis and oncogenesis of MCF-10A mammary epithelial acini grown in three-dimensional basement membrane cultures. *Methods* **30**, 256-268 (2003).

40. Imbalzano, K.M., Tatarkova, I., Imbalzano, A.N. & Nickerson, J.A. Increasingly transformed MCF-10A cells have a progressively tumor-like phenotype in three-dimensional basement membrane culture. *Cancer Cell Int* **9**, 7 (2009).
41. Levental, K.R. *et al.* Matrix crosslinking forces tumor progression by enhancing integrin signaling. *Cell* **139**, 891-906 (2009).
42. Muthuswamy, S.K., Li, D., Lelievre, S., Bissell, M.J. & Brugge, J.S. ErbB2, but not ErbB1, reinitiates proliferation and induces luminal repopulation in epithelial acini. *Nat Cell Biol* **3**, 785-792 (2001).
43. Berdichevsky, F., Alford, D., D'Souza, B. & Taylor-Papadimitriou, J. Branching morphogenesis of human mammary epithelial cells in collagen gels. *J. Cell Sci.* **107 (Pt 12)**, 3557-3568.

Chapter 2

Microrheology

2.1 Introduction

While many studies have correlated cell phenotype changes with bulk material properties, there remains a critical need to quantify the local mechanical microenvironment on a length scale relevant for cells and their adhesive complexes in 3D culture systems. Microrheology is the study of how fluid or solid-like a material is on a micron scale and has previously been used to look at the mechanical properties of the cytoplasm[2-4], as well as ECM polymers like hyaluronan[5] and collagen[6]. Because microrheology can characterize the elastic and viscous moduli in viscoelastic systems at the micron level[7], it can be especially useful in characterizing interactions between cells and their extra cellular matrix (ECM). In viscoelastic systems, even though stress and strain are related nonlinearly, stiffness relates linearly with stress[8]. Therefore, studying cell-mediated stresses on the ECM is equivalent to measuring ECM stiffness[8]. Unlike bulk methods which provide an averaged ensemble of the measured sample, microrheology is sensitive to the micro scaled spatial heterogeneities that are inherent within natural matrices like collagen and fibrin[9].

In microrheology, probe particles are embedded in the medium and their motion is monitored in time. The size of the probe and its external chemistry can be tailored depending on the material being investigated. The probe size must be equal to or slightly greater than the pore size of the mesh otherwise embedded particles would undergo Brownian motion in pockets and not engage the material. Because natural hydrogels exhibit large mesh sizes, probes can be carboxylated to promote adhesion between fibers. Probes whose surface chemistry allows

adhesion with network fibers have been shown to recover the viscoelastic properties of the matrix better than those probes whose chemistry did not allow adhesion. For instance, McGrath *et al*. found that treating probes to anchor to F-actin networks allowed accurate measurement of the elastic properties of the networks, as compared to those beads whose coating prevented adsorption, which diffused freely through, and did not provide useful elastic information[10].

In studying the likes of viscoelastic gel, two techniques exist: passive microrheology (PMR) and active microrheology (AMR). PMR is much easier to implement experimentally and can be much cheaper than AMR[11] because it only requires tracking bead motion via video[11] or laser[12]. The theory of PMR relies on Stokes-Einstein relationship which correlates thermal fluctuations of freely diffusing particles to the rheological properties of the surrounding material. However, in the study of cell-ECM interactions, the use of PMR is severely limited. First, if the system is not in equilibrium, PMR underestimates the viscoelastic properties of the medium[12]. Unfortunately, cell-ECM systems are almost always out of thermodynamic equilibrium due to non-thermal fluctuations such as mechanical and chemical changes[11]. Second, PMR measurements are limited to soft gels on the order of a few pascals[13, 14], which is significantly softer than naturally derived matrices. AMR, on the other hand, does not depend on the equilibrium conditions of the material[12] and can measure materials with stiffness up to 1 kPa. Additionally, AMR is less noise-sensitive within a bandwidth of 0.1 Hz to 100 kHz[12]. Therefore, AMR is more suitable for measuring cell-ECM interactions and will be a prime focus of discussion in this thesis.

The full tweezers theory has been described previously[15, 16]. Briefly, optical tweezers employ a Gaussian beam that is tightly focused through a high numerical aperture objective lens to trap transparent particles[15]. As light from the laser collides with the particle, its momentum exerts a force, called the scattering force, pushing the bead along the optical axis[16]. As rays from

the focus beam impinge upon the particle, light refracts within the particle and results in a force that acts in the direction of light gradient[17]. In order to maintain a stable trap, the gradient force must be greater or equal to the scattering force. The higher the numerical aperture, the steeper the incoming rays and the stronger the gradient force, thus the more stable the trap[7]. Because the rays entering and exiting the bead are symmetric, the gradient forces acting on a stably trapped particle are equal and opposite, resulting in a single average position[15]. Small-scale displacement from this position can be modeled with a linear Hookean spring[7].

Viscoelastic materials under dynamic stress exhibit a nonlinear, time-dependent behavior depending on the applied stress. As a microsphere is forced to oscillate under influence of the oscillating trapping beam, the local matrix resists the sphere's oscillation through both elastic storage and viscous dissipation. Consequently, the amplitude and phase of the sphere's oscillation is modulated with respect to the oscillating laser trap. The phase-amplitude relationships between the sinusoidal input signal (driving laser position) and the resultant output signal (bead position) are used to calculate the complex shear modulus G^* for the medium (Equation 8). G^* comprises of a real component G', the bulk modulus and an imaginary component G'', the loss modulus. G' corresponds to matrix stiffness and G'' to viscosity.

2.2 Description of the AMR system

Our manual AMR system has been described previously[9] and is illustrated in **Figure 2.1**. The optical tweezers are generated by a continuous-wave fiber laser with emission at 1064 nm Ytterbium fiber laser (IPG Photonics), hereafter referred to as the trapping beam. Trapping laser power was cut from 2.2 W at emission to 300 mW (as measured before entering the microscope) using a calcite polarizer and horizontally polarized via a half wave plate. The trapping beam is

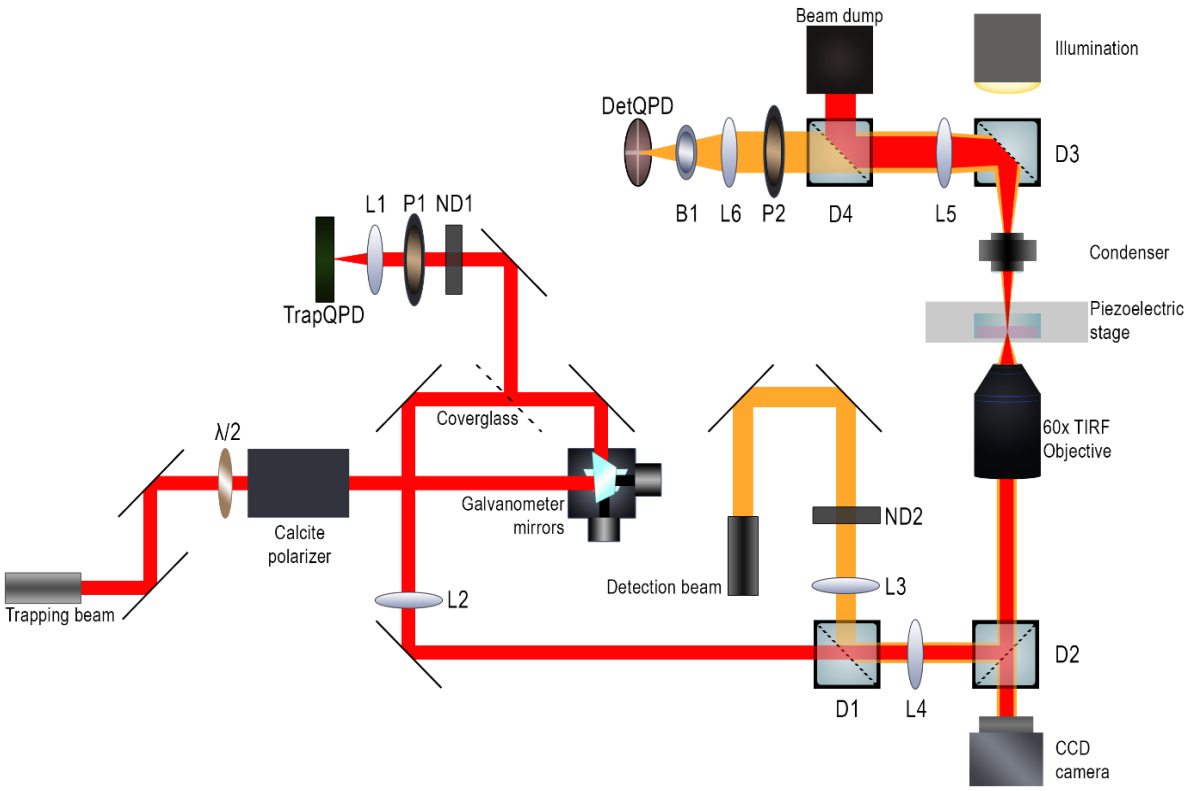

Figure 2.1: *Depiction of optical tweezers AMR system. The optical system comprises of two lasers beams* (1064 nm and 785 nm)*, a half wave plate* (λ/2)*, lenses* (L#)*, polarizers* (P#)*, dichroic mirrors* (D#)*, and neutral density filters* (ND#)*. Quadrant photo diodes* (QPDs)*, galvanometer mirrors, a CCD camera, a 60x oil objective and a condenser are also used.*

steered in the transverse plane by a pair of galvanometer mirrors (ThorLabs) placed conjugate to the back focal plane of the objective lens. Keeping the mirrors in the image plane allows beam steering without effecting alignment[7]. A small fraction of laser beam power is reflected by the cover glass and directed onto a quadrant photo Diode (QPD, Newport) labeled as trapQPD in **Figure 2.1**. A neutral density filter (ND1) and polarizer (P1) are used in conjunction to minimize the laser power before focusing it onto the trapQPD with lens L1 (50 mm). The trapQPD outputs analog signals proportional to the deflection of the trapping beam in the transverse plane. A position sensitive detector can be also be used if oscillations are uniaxial.

Particle detection is achieved by a low power laser diode with emission at 785 nm (World Star Technologies), hereafter referred to as the detection beam. A neutral density filter (ND2) is utilized to minimize the trapping power of the detection beam such that only the trapping beam influences rheological measurements. The two laser beams are combined by a long pass dichroic beam splitting mirror (D1, Semrock) and introduced into the white light path of an IX81 inverted microscope (Olympus), which is equipped with the Zero Drift Compensation package (Olympus) comprising an external laser/detector unit and a filter cube placed just below the microscope objective lens (D2 in **Fig. 2.1**). Laser wavelengths were selected to minimize photo damage in biological samples[15] and to avoid overlap with fluorescent laser lines. We removed the laser/detector unit and replaced the stock dichroic beam splitting mirror with a short pass dichroic beam splitting mirror (Chroma) designed to reflect our laser beams into the microscope objective lens while passing visible light for confocal and brightfield microscopy. The trapping beam is expanded by lenses L2 (400 mm) and L4 (500 mm) and detection laser by lenses L3 (150mm) and L4 to overfill the back aperture of the objective lens. L2 and L3 are placed such that their front focal plane is coincident with the back focal plane of L4 to collimate the beams before entering the objective. Both beams are focused by a high numerical aperture microscope objective lens (60x-oil PlanApo TIRFM 1.45 NA, Olympus) into the hydrogel. The trapping beam is expanded by lenses L2 (400 mm) and L4 (500 mm) and detection laser by lenses L3 (150mm) and L4 to overfill the back aperture of the objective lens. The focused light is collected by the microscope condenser lens (0.55 NA, Olympus) and reflected by a 50/50 beam splitter (ThorLabs), labeled D3 in **Figure 2.1**. The movement of the bead position as a result of trapping beam oscillation can be detected by observing the detection laser light transmitted through the particle for it acts as a lens and projects the forward scattering light. The interference pattern of the transmitted light and the

light not deflected by the bead is detected in the back focal plane of the condenser[18] by another quadrant photo detector (detQPD, Newport). detQPD is mounted on a manual XYZ movement mount for micrometer positioning during calibrations (*described below*). The detection beam is focused on the detQPD by lenses L5 (f = 50 mm) and L6 (f = 75 mm). To reflect the trapping beam away from the detQPD, a short pass dichroic beam splitting mirror D4 (Chroma Technologies) is placed before the detQPD. A band pass filter (B1) centered at 785 nm is placed directly in front of the detQPD to remove noise from non-laser sources. A microbead oscillating in the hydrogel will steer the detection beam across the surface of the detQPD, which outputs analog signals proportional to the position of that microbead. For AMR measurements, signals are sampled at 10 kHz using an NIPXI M series data acquisition board (National Instruments).

The entire optical system is mounted on a vibration dampening SMART table (Newport). Samples are placed into a motorized XY stepper motor stage (MS-2000, Applied Scientific Instruments) with micrometer resolution. A piezoelectric XY stage (P-733.2CL, Physik Instrumente) insert is placed within the stepper motor stage for sub-nanometer resolution movements over an area of (100 x 100) μm^2. The microscope is also equipped with a FluoView 1200 laser scanning confocal unit (Olympus) with laser lines at 405, 488, 559 and 635 nm for confocal fluorescence and reflection microscopy.

2.3 System alignment and calibration

Before each experiment, the optical tweezers and particle detection laser beams are co-aligned. First, a microbead is optically trapped by the detection beam alone in water so that the bead exhibits Brownian motion in the trap. The stiffness of the detection beam optical trap is at least one order of magnitude weaker than the optical trap and has negligible influence on our measurements of *G'*

(empirically observed). Next, the position of detQPD is adjusted so the mean position of the microbead in the trap corresponds to 0 V on the detector. Specifically, the position of the detQPD is adjusted in the transverse plane by micrometers until $<Vdet, x> = < Vdet, y> = 0$ V, where $<Vdet, x>$ and $<Vdet, y>$ are the mean x and y analog outputs of the detQPD. Next, in order to co-align both beams, the same microbead is trapped by the trapping beam. The position of the trapping beam is then adjusted by rotating the galvanometers with LabVIEW (National Instruments) until once again $<Vdet, x> = < Vdet, y> = 0$ V. Laser co-alignment is improved by adjusting the galvanometers until a linear response is observed in the detQPD signal as the trapping beam is oscillated in either the x or y axis in a triangle wave around the center of the detection beam. The mean position of the oscillation is adjusted until the detQPD is devoid of nonlinear aberrations such as flattened peaks and valleys or amplitude inversions at the peaks and valleys.

Next, the trapping beam stiffness κ_t is calculated from the Brownian motion of a trapped microbead using the power spectrum method[19]. Briefly, a microbead is trapped and placed in the center of the detection beam focus. Then, detQPD signals are sampled for 30 seconds at 100 kHz. The power spectra of those signals are then fit to a Lorentzian function. κ_t is determined from the corner frequency f_c of the Lorentzian with the following relationships:

$$\kappa_t = f_c 2\pi\gamma \tag{1}$$

$$\gamma = 6\pi\eta r \tag{2}$$

where γ is the viscous drag coefficient, η the viscosity of water and r the radius of the bead.

Following trap stiffness calculation, both detQPD and trapQPD are calibrated by a triangle wave oscillation of a trapped bead in water with frequency 0.1Hz and amplitude 4 mV over the course of 60 seconds. A bead trapped in a stationary beam displays a symmetric interference

pattern and movement creates an asymmetric interferences which results in a proportional voltage change in the QPD. Thus, by comparing the resultant linear regions of the detection and trapping QPD signals, a volts-to-meter conversion factor can be determined. Lastly, AMR is conducted to

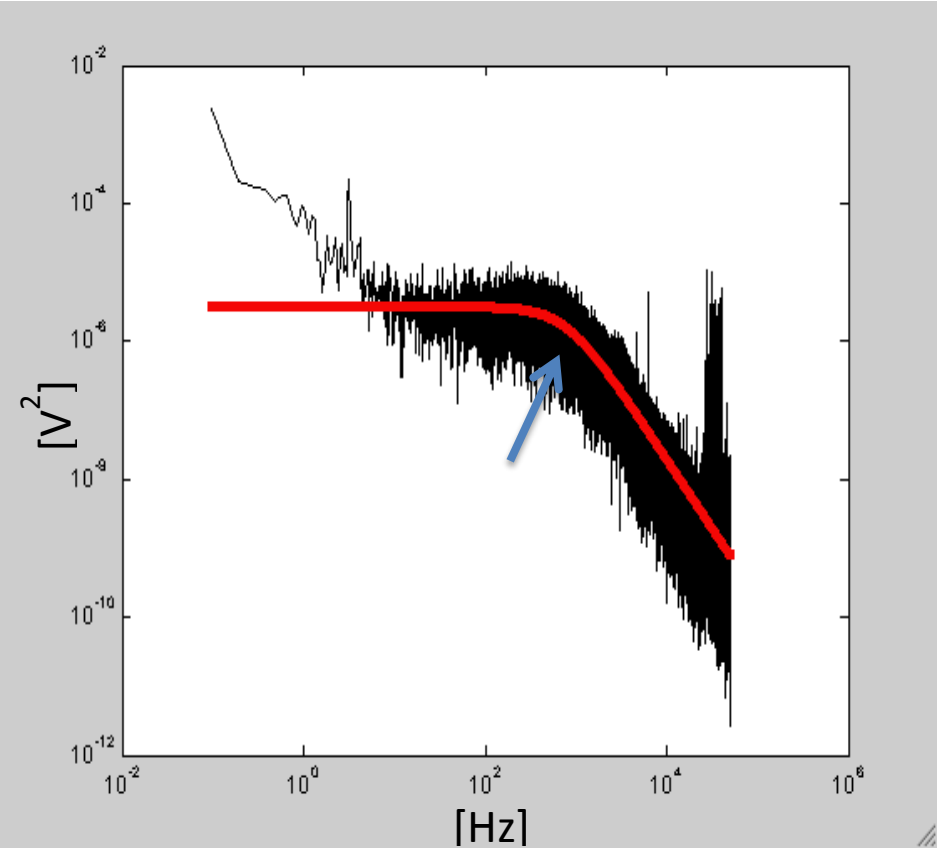

Figure 2.2: *Power spectral density of a 2 μm carboxylated bead captured within a trapping beam in water. Red line is a Lorentzian fit to raw data (black) and blue arrow denotes the corner frequency*

ensure experimental η measured matches within 10% of theoretical η of water (0.001 Pa s at 25 °C), where

$$\eta = \frac{G''}{2\pi f} \tag{3}$$

Calibrations are conducted between 30-40 μm above glass, the height at which experimental samples are measured and glass effects are negligible[19]. **Figure 2.2** shows a typical power spectrum for the position of a 2 μm-silica bead held by optical tweezers in water.

2.4 Measurement of the complex shear modulus

In optical tweezers AMR, the transverse position of the optical trap focus is oscillated as a sinusoid by with galvanometer mirrors. The extracellular matrix surrounding the bead resists bead motion through both elastic storage and viscous dissipation. This modulates the amplitude and phase of the bead oscillation relative to the optical trap. The pointing position of the trapping beam is detected by the trapQPD (Supplementary Fig. 2). The local complex shear modulus *G*, which is representative of the local matrix surrounding the bead[11], is then computed from trapQPD and detQPD signals. More details can be found in our previous publication[2] and seminal papers in the field[12, 20]. Briefly, two waveforms are extracted from QPD signals, which correspond to the bead position $x_B(t)$ and trapping beam position $x_T(t)$. The force waveform $f(t)$ is then computed as:

$$f(t) = \kappa_t(x_T(t) - x_B(t)) \tag{4}$$

Taking the Fourier transforms of $x_B(t)$ and $f(t)$ we can compute the complex valued material response function $A(\omega)$ [20]

$$X(\omega) = A(\omega)F(\omega) \tag{5}$$

Accounting for the influence of the optical trap, a corrected material response function α is determined[12]

$$\alpha(\omega) = {A(\omega)}\Big/{1 - \kappa_t A(\omega)} \tag{6}$$

It is important to note that detection beam trap stiffness is an order of magnitude lower than the trapping beam stiffness and has negligible effect on the bead (data not shown). Therefore, only the trapping beam is used to adjust the material response. Lastly, the complex shear modulus *G* can be computed from the generalized Stokes equation[12], which relates the drag force on a spherical object to complex material properties so that

$$G(\omega) = {}^{1}/_{6\pi r\alpha(\omega)} \quad (7)$$

$$G(\omega) = G'(\omega) + iG''(\omega) \quad (8)$$

where *G'* and *G''* are the elastic and loss modulus, respectively.

2.5 Roles of pericellular rigidity in stem cell lineage commitment

It has long been known that ECM stiffness can influence many cellular processes, a key one being differentiation. In a hallmark study, Engler et al. demonstrated that mesenchymal stem cells (MSC) differentiation was dependent on ECM stiffness. He cultured MSCs atop polyacrylamide gels whose elasticity roughly matched different tissues in the body. Namely, soft gels (0.1 – 1 kPa) mimicked brain elasticity, gels of medium stiffness (8 – 17 kPa) mimicked striated muscles, and lastly very stiff gels (25 – 40 kPa) were used to mimic the cross-linked collagen of bone matrix[21]. MSCs cultured in these conditions displayed morphology similar to neurons, muscles, and osteoblasts, respectively. Lineage specific markers supported these results[21]. Other studies have also followed suit and demonstrated that ECM elasticity influences stem cell differentiation[22-24].

Nevertheless, these studies have all been conducted in 2D settings with or without natural matrices. It is a given that synthetic matrices do not recapitulate the complex mechanical and physical properties of natural matrices, which are fibrous, viscoelastic, exhibit strain hardening and non-linear stress strain relationships[8, 25]. Importantly, cells within natural matrices can rearrange the fiber architecture, degrade their matrix, and exert forces[26]. These interactions are part of a larger more complicated feedback system that isn't well understood. Nevertheless, cell-ECM interactions must be accounted for when determining the role of ECM mechanics on cellular behavior.

My curiosity for understanding cell-ECM interactions was triggered in my collaboration with Dr. Stephen Weiss from the University of Michigan. His lab works primarily with matrix metalloproteinases, in particular MT1-MMP, to understand their roles in cellular processes like differentiation[1] and migration[27]. MT1-MMP is a membrane tethered matrix metalloproteinase (MMP) [28]. It is the primary operative for type I collagen degradation and is of particular importance in physiology because it is the only MMP whose global deletion in mice results in early prenatal death[1].

Interestingly, MT1-MMP expression is upregulated in skeletal stem cell (SSC) differentiation into bone precursors, but downregulated in adipogenic and chondrogenic pathways[1]. Thus, the Weiss group investigated the role of MT1-MMP in controlling stem cell commitment down bone, fat, and cartilage lineages. Our results were published in *Development Cell*[1]. Briefly, they found that deletion of MT1-MMP in the SSC population of mice resulted in increased cartilage and fatty tissue. The MT1-MMP knockout (KO) mice had distinct skeletal phenotypes. They were smaller and displayed short snouts and dome-shaped skulls as compared to MT1-MMP wild type (WT) mice. In support, mRNA levels of osteogenic markers were significantly lower and chondrogenic markers significantly higher in KO mice. Furthermore, none of the KO mice survived past 10 months. These result clearly indicate that MT1-MMP plays a role in SSC lineage control.

To study this phenomenon further, the Weiss lab isolated KO and WT SSCs from mice populations. Surprisingly, isolated KO cells cultured on plastic dishes were able to differentiate into osteoblast lineages at similar frequency as the WT. Taking into consideration the role of MT1-MMP as a collagenase, they cultured both cell types on top of collagen (still 2D) and exposed to differentiation media as before. Still, the KO cells maintained their ability to differentiate into

osteoblast linages like the WT cells. Only, when the KO cells were embedded within the collagen, did they display a significant decrease in osteoblast differentiation in comparison to WT. Similar to *in vivo* results, KO cells embedded in collagen displayed stronger differentiation towards adipocyte lineages and chondrocyte lineages compared to WT. Even though the morphology in embedded WT and KO cells looked similar, WT cells displayed higher active β-1 integrin levels, phosphorylated focal adhesion kinase, and Rho GTPase activity. Further implicating adhesion mediated mechanotransduction, inhibiting β-1 activity in WT cells prevented osteogenic lineage commitment while constitutively active β-1 integrin transfection in KO cells rescued the osteogenic lineage commitment. It is worth noting that levels of these markers are indistinguishable for WT and KO cells cultured in planar conditions, supporting the importance of careful selection of *in vitro* culture models in order to recapitulate physiological conditions.

Next, the role of ECM remodeling in controlling stem cell commitment was investigated. WT and KO cells were cultured within PEG hydrogels containing sites that could or could not be hydrolyzed by MT1-MMP. WT cells switched from osteogenic commitment to adipogenic commitment in PEG gels with MT1-MMP resistant sites. An important difference here, however, was that in MT1-MMP resistant gels, WT cells were not able to spread, and as such, unable to activate adhesion mediated signaling.

But, simple degradation of the matrix should not trigger adhesion mediated signaling and increase rhoGTPase signaling, as observed. At this point, Dr. Weiss approached our lab to measure the pericellular rigidity around these cells. I cultured both WT and KO cells in type 1 collagen gels with embedded micro breads and conducted active microrheology *near* and *far* from cell bodies.

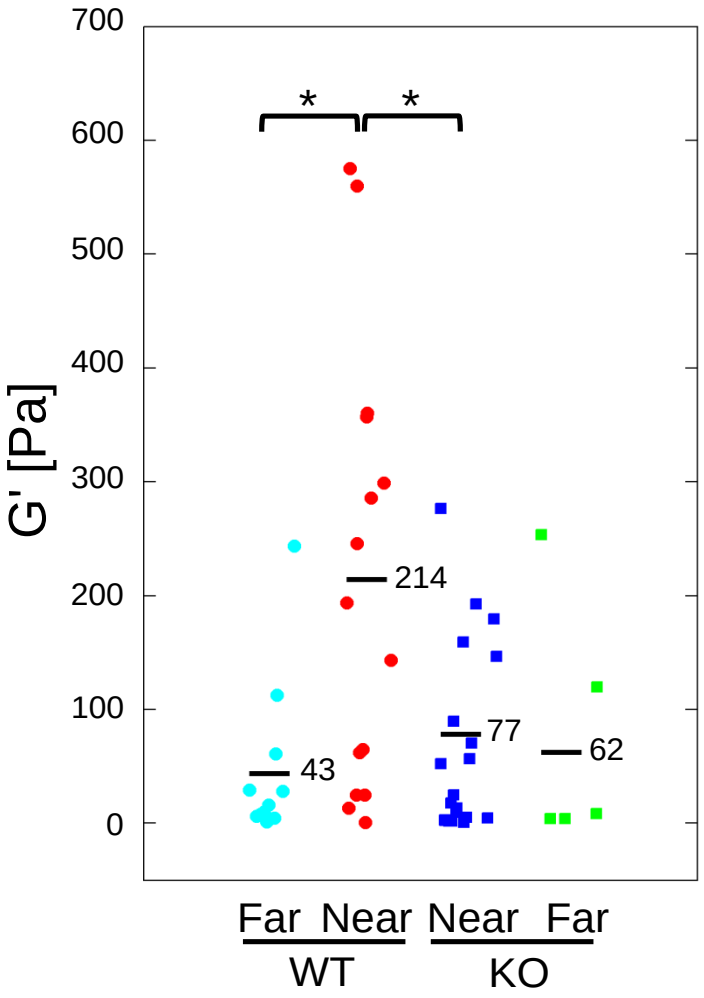

Figure 2.3: *G' measurements in collagen gels near and far from skeletal stem cells wild type* (WT) *or knockouts* (KO) *for MT1-MMMP. WT cells were able to significantly increased pericellular stiffness compared to KO cells*[1].

Beads within 50 μm of a cell body were classified as *near* and those farther than 100 μm were classified as *far*. *G'* values reported that WT cells were able to significantly stiffen their pericellular matrix (**Fig. 2.3**) as compared to KO cells, who had lost this functionality. Further supporting cell-ECM mechanical interactions in this process, reducing cytoskeleton tension in WT cells by inhibiting ROCK with Y27632, resulted in lineage commitment similar to KO cells. Thus, we demonstrated that MT1-MMP activity controls stem cell lineage by increasing pericellular rigidity via remodeling, thus activating β1 integrin pathways and cellular contractility. These findings reveal that cells are active manipulators of their surrounding ECM stiffness, not passive

bystanders, as previous studies had modeled[21-24]. Clearly, understanding the role of pericellular stiffness can provide insight into cell-ECM interactions.

2.6 References

1. Tang, Y., Rowe, G., Botvinick, E.L., Kurup, A,. *et al.* MT1-MMP-dependent control of skeletal stem cell commitment via a beta1-integrin/YAP/TAZ signaling axis. *Dev Cell* **25**, 402-416 (2013).
2. Rogers, S.S., Waigh, T.A. & Lu, J.R. Intracellular microrheology of motile Amoeba proteus. *Biophys. J.* **94**, 3313-3322 (2008).
3. Thompson, M.S. & Wirtz, D. Chapter 18: Sensing cytoskeletal mechanics by ballistic intracellular nanorheology (BIN) coupled with cell transfection. *Methods Cell Biol.* **89**, 467-486 (2008).
4. Panorchan, P., Lee, J.S., Kole, T.P., Tseng, Y. & Wirtz, D. Microrheology and ROCK signaling of human endothelial cells embedded in a 3D matrix. *Biophys. J.* **91**, 3499-3507 (2006).
5. Nijenhuis, N., Mizuno, D., Schmidt, C.F., Vink, H. & Spaan, J.A. Microrheology of hyaluronan solutions: implications for the endothelial glycocalyx. *Biomacromolecules* **9**, 2390-2398 (2008).
6. Velegol, D. & Lanni, F. Cell traction forces on soft biomaterials. I. Microrheology of type I collagen gels. *Biophys. J.* **81**, 1786-1792 (2001).
7. Shaevitz, J.W. A Practical Guide to Optical Trapping. *Retrieved Jul* **30**, 2010 (2006).
8. Humphrey, J.D., Dufresne, E.R. & Schwartz, M.A. Mechanotransduction and extracellular matrix homeostasis. *Nature reviews. Molecular cell biology* **15**, 802-812 (2014).
9. Kotlarchyk, M.A. *et al.* Concentration Independent Modulation of Local Micromechanics in a Fibrin Gel. *PloS one* **6**, e20201.
10. McGrath, J.L., Hartwig, J.H. & Kuo, S.C. The mechanics of F-actin microenvironments depend on the chemistry of probing surfaces. *Biophys. J.* **79**, 3258-3266 (2000).
11. Squires, T.M. & Mason, T.G. Fluid Mechanics of Microrheology. *Annu Rev Fluid Mech* **42**, 413-438 (2010).
12. Mizuno, D., Head, D.A., MacKintosh, F.C. & Schmidt, C.F. Active and Passive Microrheology in Equilibrium and Nonequilibrium Systems. *Macromolecules* **41**, 7194-7202 (2008).
13. Schultz, K.M. *et al.* Electrospinning covalently cross-linking biocompatible hydrogelators. *Polymer* **54**, 363-371 (2013).
14. Nijenhuis, N., Mizuno, D., Spaan, J.A. & Schmidt, C.F. High-resolution microrheology in the pericellular matrix of prostate cancer cells. *Journal of the Royal Society, Interface / the Royal Society* **9**, 1733-1744 (2012).
15. Neuman, K.C. & Block, S.M. Optical trapping. *Rev. Sci. Instrum.* **75**, 2787-2809 (2004).
16. Nieminen, T.A., Knoner, G., Heckenberg, N.R. & Rubinsztein-Dunlop, H. Physics of optical tweezers. *Method Cell Biol* **82**, 207-236 (2007).
17. Ashkin, A. Forces of a Single-Beam Gradient Laser Trap on a Dielectric Sphere in the Ray Optics Regime. *Biophys. J.* **61**, 569-582 (1992).
18. Visscher, K. & Block, S.M. Versatile optical traps with feedback control. *Methods Enzymol.* **298**, 460-489.
19. Gittes, F. & Schmidt, C.F. Signals and noise in micromechanical measurements. *Methods Cell Biol.* **55**, 129-156 (1998).
20. Brau, R.R. *et al.* Passive and active microrheology with optical tweezers. *Journal of Optics a-Pure and Applied Optics* **9**, S103-S112 (2007).
21. Engler, A.J., Shamik, Sweeney, H.L. & Discher, D.E. Matrix Elasticity Directs Stem Cell Lineage Specification. *Cell* **126**, 677-689.
22. Mullen, C.A., Haugh, M.G., Schaffler, M.B., Majeska, R.J. & McNamara, L.M. Osteocyte differentiation is regulated by extracellular matrix stiffness and intercellular separation. *Journal of the mechanical behavior of biomedical materials* **28**, 183-194 (2013).
23. Eroshenko, N., Ramachandran, R., Yadavalli, V.K. & Rao, R.R. Effect of substrate stiffness on early human embryonic stem cell differentiation. *Journal of biological engineering* **7**, 7 (2013).
24. Wen, J.H. *et al.* Interplay of matrix stiffness and protein tethering in stem cell differentiation. *Nature materials* **13**, 979-987 (2014).

25. Miroshnikova, Y.A. *et al.* Engineering strategies to recapitulate epithelial morphogenesis within synthetic three-dimensional extracellular matrix with tunable mechanical properties. *Physical Biology* **8**, 026013.
26. Lopez, J.I., Mouw, J.K. & Weaver, V.M. Biomechanical regulation of cell orientation and fate. *Oncogene* **27**, 6981-6993 (2008).
27. Sabeh, F., Shimizu-Hirota, R. & Weiss, S.J. Protease-dependent versus -independent cancer cell invasion programs: three-dimensional amoeboid movement revisited. *J. Cell Biol.* **185**, 11-19 (2009).
28. Rowe, R.G. & Weiss, S.J. Navigating ECM barriers at the invasive front: the cancer cell-stroma interface. *Annu. Rev. Cell Dev. Biol.* **25**, 567-595 (2009).

Chapter 3

Novel insights from 3D models: the pivotal role of physical symmetry in epithelial organization

Abhishek Kurup[1], Shreyas Ravindranath[1], TimTran[1], Mark Keating[1], Philippe Gascard[2], Lorenzo Valdevit[3], Thea D. Tlsty[2], Elliot L. Botvinick[1, 4]

[1] University of California Irvine, Department of Biomedical Engineering, Irvine, USA
[2] University of California San Francisco, Department of Pathology, San Francisco, USA
[3] University of California Irvine, Department of Mechanical and Aerospace Engineering, Irvine, USA
[4] University of California Irvine, Department of Surgery, Irvine, USA

In Review at Scientific Reports

3.1 Introduction

Over the past decade it has become apparent that the mechanical properties of the extra cellular matrix (ECM) play important roles in breast cancer[1-3]. One way in which cells can gauge these properties is through transmembrane receptors such as integrins[4], which are activated by mechanical tension leading to downstream molecular signaling in a process called mechanotransduction[5]. Changes in integrin signaling and expression can drive epithelial to mesenchymal transition[6], regulate cell-adhesion and migration[7], and promote tumor progression[8]. Furthermore, blocking integrin activity with an exogenous ligand has been shown to reverse the malignant phenotype in mammary epithelial cells (MECs) *in vitro*[9]. Just as cells mechanically interact with the ECM via integrins, they interact with neighboring cells via specialized protein scaffolds including cadherins, which play a key role in cell-cell adhesion and force transmission[10]. Cadherins also play a prominent role in maintaining MEC polarization and homeostasis[11]. Similar

to integrins, cadherin-mediated force transduction correlates with substrate rigidity and has been implicated in cancer[10, 12, 13].

In order to better understand both biochemical and mechanical cell-ECM and cell-cell interactions in a physiologically relevant context, 2D cell culture has been largely replaced with 3D cell culture[14]. While 3D tissue culture models are no substitute for animal models, they do allow engineering control over system architecture, molecular transport, mechanical stresses, growth factors, and other aspects found *in vivo*, and in that regard, are superior to 2D culture[15-17]. 3D culture methods are also compatible with multi-well plate arrays and lab-on-a-chip formats for use in high-throughput screening studies[16, 18]. For example, it has been shown that 3D hepatocyte culture was superior to 2D in drug toxicity testing and recapitulated the results found *in vivo*[19].

3D cell culture is commonly used in breast cancer biology. In these studies MECs are cultured within or on a hydrogel containing laminin-rich reconstituted basement membrane (rBM), such as Matrigel[14]. MECs cultured with rBM form 3D, hollow, growth-arrested and polarized acini that resemble the glandular milk producing lobules of the breast *in vivo*[20]. Importantly, they do not form these structures in 2D[21]. Relating these studies to physiological relevance, the processes of acinus disruption within *in vitro* 3D models have been shown to be similar to those observed *in vivo*[21]. During acinus disruption, *in vitro* growth-arrested acini exhibit initiation of proliferation, apoptosis evasion, and polarization loss[22]. Downstream of acinus disruption, upon progression towards metastasis, cancerous cells invade the nearby matrix via increased matrix metalloproteinase (MMP)-mediated remodeling, cell-generated forces and migration[9, 22, 23].

There are two predominant 3D culture methods in the field of breast cancer: the overlay protocol (OP) and the embedded protocol (EP) (**Fig. 3.1a**). What is not yet clear is which of these two methods of 3D cell culture is the most appropriate for investigating the effects of the ECM on

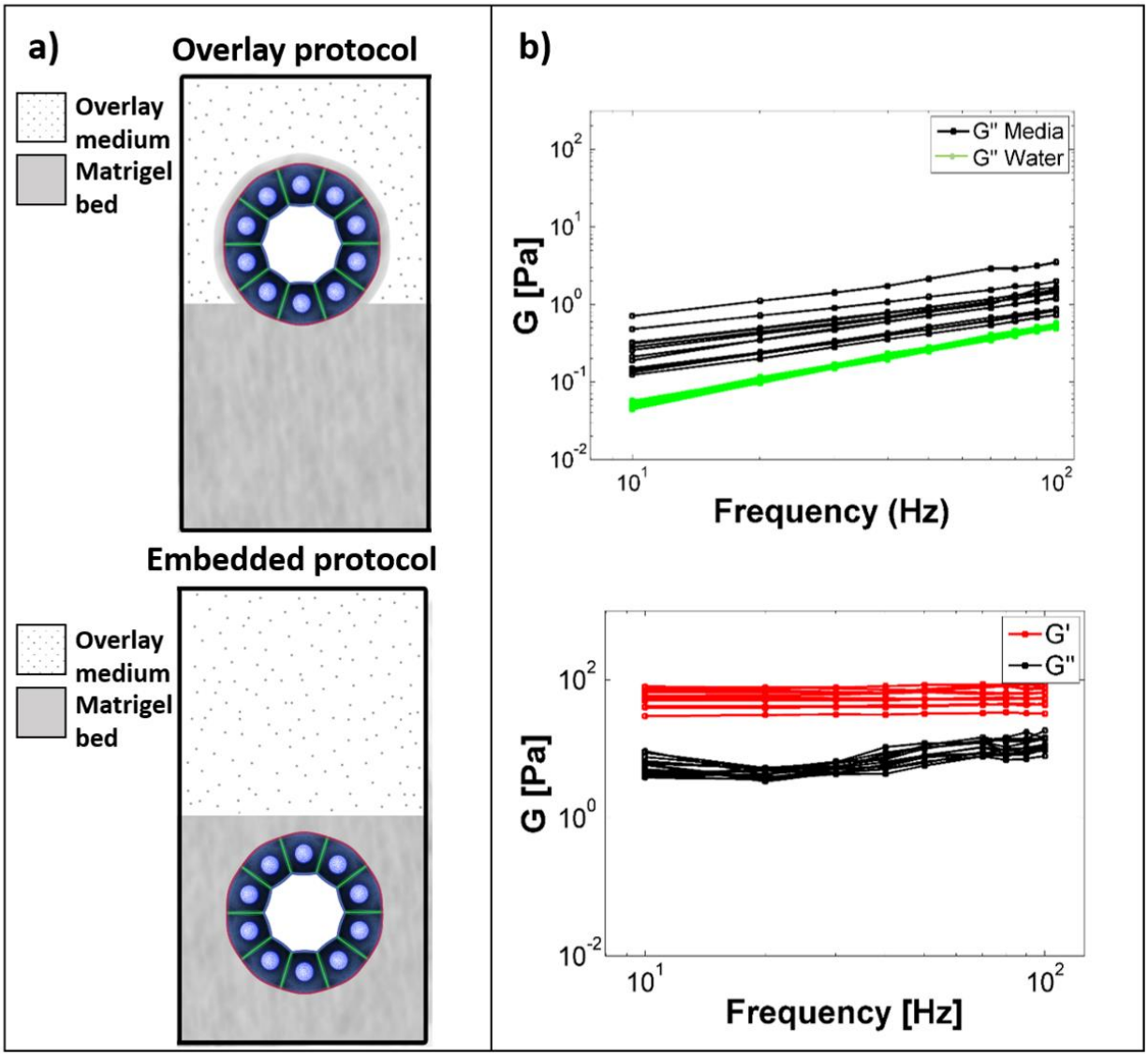

Figure 3.1: *Mechanical properties of EP and OP. (a) Schematic representation of the overlay and embedded culture methods. Red corresponds to β4 integrin, green to cadherin, and light blue circles are representative of the nuclei. (b) Frequency spectra for the complex shear modulus G of water, OM and the Matrigel bed as determined by AMR. G' and G'' frequency sweeps of 10, 20, 30, 40, 50, 70, 80, 90, and 100 Hz are shown. Each line represents a different bead. 10, 13, and 13 beads were measured for water, OM and Matrigel, respectively. Statistical significance was determined with one-sided Mann-Whitney U tests with $p < .025$ deemed significant.*

MEC acini phenotype. Indeed, these methods differ in the way acini interact with the ECM. In OP, the more commonly used of the two, cell colonies are cultured atop a thin film of ECM, typically comprised of Matrigel and extracellular molecules such as type 1 collagen. The culture is

supplemented with overlay medium (OM) consisting of assay medium plus 2-4% Matrigel (see methods). Matrigel in the OM forms a thin membrane around the otherwise free surfaces of the acini such that cells are in a 3D ECM environment (**Fig. 3.1a**, *top*) [20]. On the other hand, in EP, cells are completely submerged within the ECM (**Fig. 3.1a**, *bottom*). While acini form in both conditions, EP is used infrequently in the literature compared to OP because the OM can be easily washed off allowing direct access to the cells for staining, imaging, and harvesting[20].

Experimentally, acini are slightly submerged within the ECM in OP. This is an important aspect of OP because the interface between the ECM bed and OM introduces a discontinuity in the mechanical environment. Therefore, when investigating ECM resistance to deformation under cell contractile forces one cannot consider the mechanical properties of the ECM alone, but must also consider the geometry of the system. In OP, the fluid surface of the laminin-rich OM creates a 3D biochemical, but a 2D mechanical microenvironment. In this study, we sought to determine whether the physical natures of OP and EP could influence MEC acini homeostasis and disruption. We find that physical symmetry is dominant over ErbB2 signaling and/or matrix crosslinking in influencing acinar phenotype.

3.2 Significant differences between OP and EP for cell-ECM and cell-cell mechanical stresses

Cell-cell and cell-ECM mechanical stresses depend on the resistance of the ECM to deformation, which in turn depends on both material properties and the geometry of the system. To understand stresses acting on and within an acinus cultured according to either OP or EP, we first used optical tweezers active microrheology (AMR) [24] to measure the viscoelastic shear modulus (*G*, a material

property) of OM and Matrigel. *G* is a complex parameter with $G = G' + iG''$, where *G'* and *G''* are the shear storage (elastic) and loss moduli (viscous), respectively. We first investigated whether the addition of Matrigel to culture medium (to form OM) would transform the purely viscous medium into a material capable of storing elastic energy that could react to cell contractile forces and sustain stresses acting through cell-ECM adhesions. Our results showed that G' was equal to zero for OM, indicating that OM could not store elastic energy. Furthermore, G'' was linearly dependent on frequency, indicating that OM behaved as a viscous fluid (**Fig. 3.1b**, *top*) [25]. In contrast, Matrigel exhibited a *G'* ~ 60 Pa (**Fig. 3.1b**, *bottom*), confirming that, unlike OM, Matrigel could store elastic energy. Values for *G''* across tested frequencies of oscillations were insensitive to frequency, which is typical for hydrogel systems. These results demonstrated that the OM could not resist static tensile stresses, whereas Matrigel (conditions found in EP) could.

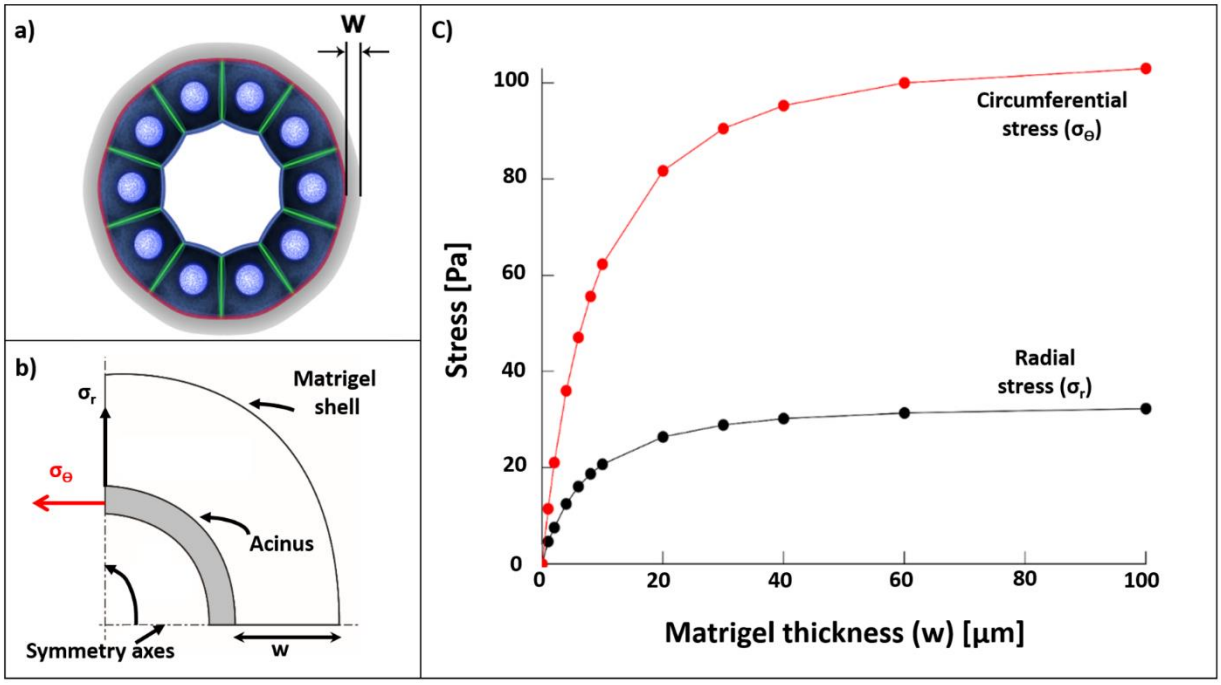

Figure 3.2: *Finite Element Analysis of adhesive and cell-cell stresses as a function of Matrigel thickness.* ***(a)*** *An acinus surrounded by Matrigel with thickness w.* ***(b)*** *Schematic of the acinus quadrant analyzed by FEA with outer radial* (σ_r) *and midpoint circumferential* (σ_Θ) *stresses.* σ_r *represents adhesive stresses between acinus and surrounding Matrigel.* σ_Θ *represents stresses acting with the wall of the acinus along cell-cell adhesions.* ***(c)*** *Computed stresses with 10% contraction of acinus when w is increased from 0 – 100 µm.*

In the first of two models, we examined the effect of the volume of Matrigel surrounding an acinus on cell-cell and cell-ECM stresses by formulating and solving models by Finite Element Analysis (FEA) in Abaqus (Dassault Systemes, U.S.). The acinus was modelled as a thick-walled spherical shell having a defined internal diameter D=100μm and wall thickness t=10μm. The acinus was surrounded by a spherical shell of Matrigel with thickness (w) ranging from 1 to 100 μm (**Fig. 3.2a**). Our model imposes a 10% uniform contraction of the acinus and computes the resulting normal stresses in the radial and circumferential directions. In the figure, the radial stress (σ_r) is probed at the outer surface of the acinus and acts in the radial direction and the circumferential stress (σ_θ) is probed at the midpoint of a cross-section of the acinus wall and acts in the circumferential direction (**Fig. 3.2b**). σ_r and σ_θ are representative of cell-ECM adhesion and cell-cell junction stresses, respectively.

Fig. 3.2c plots values of σ_r and σ_θ with increasing Matrigel shell thickness, w. Both σ_r and σ_θ are asymptotic at large values of w, where stresses are no longer sensitive to changing values of w. In other words, at large values of w (Matrigel thickness), OP system converges to EP model. Thus, this simulation compares stresses between OP and EP. Of particular note, when w is ~1μm (typical for OP), σ_r and σ_θ are one order of magnitude weaker than their asymptotic values. Thus, when viscoelastic properties of the Matrigel are held constant, the thickness of the Matrigel shell alone can modulate stresses to a large degree, highlighting an important difference between OP and EP.

In the second model, we included the ECM bed on which an acinus would form in OP. We computed σ_r and σ_θ, for an acinus partially submerged within the Matrigel bed with the free surface coated by a 1 μm-thick shell of Matrigel, as found in OP (**Fig. 3.3a**). The depth of submersion, d, was varied between zero (acinus just touching the Matrigel bed) and 2 x D (acinus

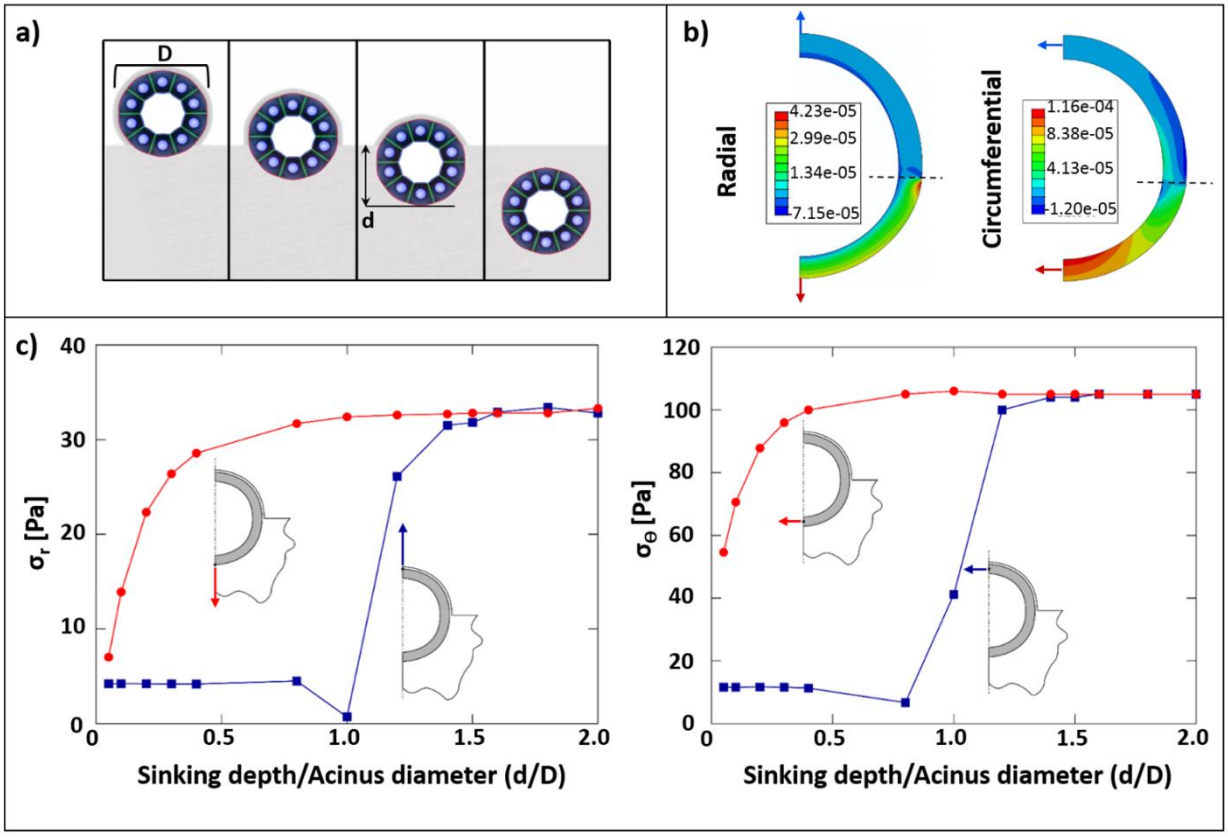

Figure 3.3: *Finite Element Analysis of OP, where the free surface of an acinus is coated by a 1 μm thick film of Matrigel. The bottom surface of the acinus is resting on or submerged* (partially or completely) *within Matrigel.* ***(a)*** *An acinus of diameter D was modelled with varying sinking depths d inside the Matrigel bed. Outer radial* (σ_r) *and midpoint circumferential* (σ_Θ) *stresses following a 10% contraction were computed for a half circle.* ***(b)*** *Color maps of stresses for* (d/D = 0.4)*. Hashed lines indicate the Matrigel-OM boundary. Units are in Megapascals. (c)* σ_r *and* σ_Θ *are shown as a function of sinking depth (D/d). Red lines* (and arrows) *correspond to the bottom of the acinus and blue lines* (and arrows) *to the top.*

deeply submerged, as in the case for EP). As shown in **Fig. 3.3b,** stresses changed with respect to both the radial and circumferential coordinates. Values of σ_r and σ_θ at the top and bottom surfaces of the acinus as a function of increasing values of *d/D* are plotted in **Fig. 3.3c**. At large values of *d/D*, σ_r and σ_θ at both surfaces increased asymptotically. Asymptotic values of stress are representative of EP and in agreement with the first model (**Fig. 3.2c**). For intermediate values of *d/D*, both σ_r and σ_θ increased with *d/D* at the bottom surface of the acinus. In contrast, stresses at the top surface were insensitive to *d/D* until *d/D* = 1, i.e. when the top surface of the acinus first

entered the bed. For *d*/D = 0.4, σ_r and σ_θ were an order of magnitude larger at the bottom surface as compared to the top.

Taken together, these two analyses indicated that stresses acting on cells in an acinus are significantly different between OP and EP both in terms of stress magnitude as well as distribution. Consequently, cell-cell and cell-ECM mechanical stresses are in fact different between OP and EP, which may result in differences in acinus morphology and phenotype.

3.3 Dimensionality is as potent as cross-linking and oncogenic activation in determining phenotype

To test further for the effects of culture dimensionality on cell biology, we cultured MECs in OP and EP under three experimental conditions previously shown to promote hyperplastic or invasive phenotypes[22, 26]. In our experiments, the OM was as described above and the bed comprised a 1:1 mixture of Matrigel and type I collagen. The first experimental condition was type 1 collagen crosslinking, a condition chosen because covalent collagen crosslinking of the stroma mediated by lysyl-oxidase (LOX) has been found to promote tumor progression in mice[27]. Clinically, breast cancer patients with ER-negative tumors and overexpression of LOX have poor survival[27]. *In vitro*, non-covalent crosslinking by collagen glycation (i.e. ribose-mediated[28]) was used to test the impact of stromal crosslinking on MEC acini structure and invasiveness[29]. The second experimental condition relied on activation of ectopic avian erythroblastosis oncogene B (ErbB2), a proto-oncogene up-regulated in 25% of metastatic breast cancers and 20-80% of Ductal Carcinoma in Situ (DCIS) [22, 30]. As a model of ErbB2 activation, we cultured MCF10A.ErbB2 cells, a line developed by the Muthuswamy laboratory. This cell line expresses a chimaeric ErbB2 receptor

which can be dimerized and activated upon addition of an exogenous synthetic ligand[22]. The third experimental condition was a combination of collagen crosslinking and ErbB2 activation, a condition that has been shown to promote acini invasion in OP using the same cell lines and ECM as those described in our experiments[26].

MCF10A.ErbB2 were cultured in OP or EP within 12-well plates for 14 days. On day 15 the medium was substituted to generate three experimental conditions: *(1) Ribose*: ribose-mediated collagen crosslinking, *(2) ErbB2*: ErbB2 signaling activation, and *(3) ErbB2 + Ribose*: both ErbB2 activation and collagen crosslinking. Cells were cultured in each experimental condition from days 15 to 30. On day 30, cells were fixed in formalin and imaged to assess acinus polarization (after staining for β4 integrin), lumen filling (after DAPI staining), and morphology (by fluorescence laser scanning confocal microscopy and transmitted light imaging). Four acinus categories were defined as summarized in **Table 3.1**.

Table 3.1: *Acinus categories and their corresponding description. Confocal fluorescence imaging was used to create the categories based on β-4 integrin polarization and the presence of a hollow lumen, as determined by immunocytochemistry and DAPI staining, respectively. Morphology was assessed manually from transmitted light images. A shape threshold of 1.3 was determined empirically.*

Category	Description			
	Morphology	Polarization (β4 Integrin)	Lumen (DAPI)	Shape
Normal (Fig. 3.4c)	Round	Yes	Yes	$\frac{Major\ Axis}{Minor\ Axis} < 1.3$
Disrupted (Fig. 3.4d)	Oval, irregular shape, bulgy	Partial	Partial	$\frac{Major\ Axis}{Minor\ Axis} \geq 1.3$
Multi-Acinar (Fig. 3.4e)	Berry-shaped; multiple lobules	Partial	Partial	
Invasive (Fig. 3.4f)	Protrusion(s). General loss of spherical geometry	Loss	Loss	

Acini in OP are larger and less round as compared to acini in EP

In total, transmitted light images for over 1900 colonies were analyzed by processing via algorithms developed with MATLAB (Mathworks) to calculate the cross-sectional area and roundness of each acinus and to categorize each acinus according to **Table 3.1**. For each image, the boundary of an acinus, imaged at its midsection, was manually traced. We defined *perimeter*

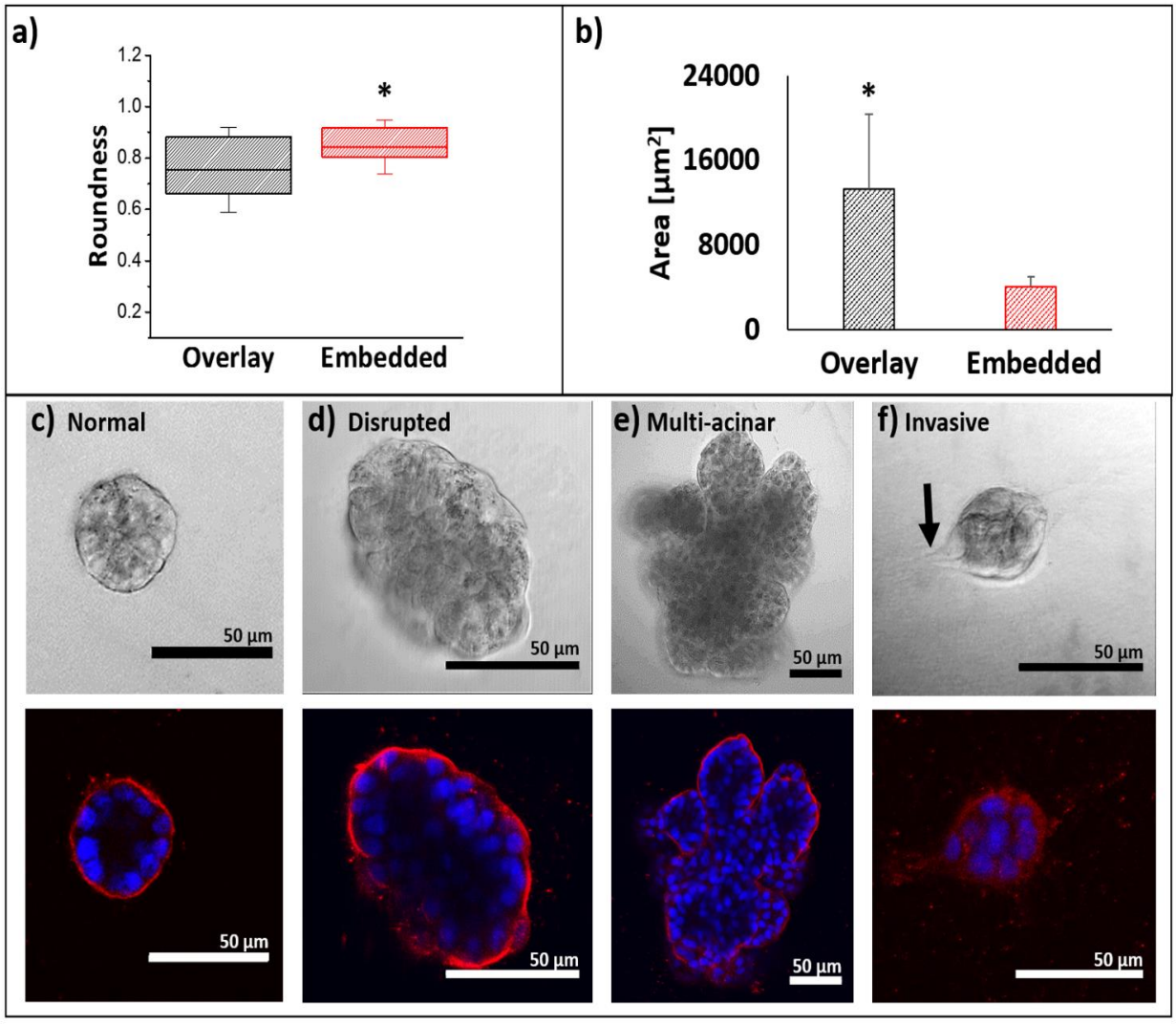

Figure 3.4: *Acinus morphology in EP and OP. Roundness **(a)** and area **(b)** of acini in EP and OP. Acini were classified from images according to 4 categories: Normal **(c)**, Disrupted **(d)**, Multi-acinar **(e)**, and Invasive **(f)**. Representative transmitted light* (top row) *and confocal fluorescence* (bottom row) *images are shown; β4 integrin immunocytochemical staining* (red) *and nuclear staining of DAPI* (blue). *Black arrow in **(f)** denotes an invasive protrusion. Scale bars are 50 µm. Samples sizes for OP and EP: 791 and 1141 acini, respectively. Statistical significance was assessed using one-sided Mann-Whitney U tests. p values < .05 are noted with an asterisk.*

as the length of the trace, *area* as the area within the traced region, and *roundness* as 4*π**area* / (*perimeter*^{2}). Acini in EP were found to be more round (**Fig. 3.4a**) and smaller **(Fig. 3.4b**) than in OP. Furthermore, acini in EP exhibited less variability in *roundness* and *area* than in OP, consistent with previous reports of smaller and more uniform acini in EP as compared to OP[20]. Our results are not surprising from a mechanical perspective because EP offers a symmetrical physical environment with greater resistance to expansion, which is predicted to limit acinus growth and to promote a more spherical phenotype.

Matrix crosslinking coupled with ErbB2 activation in OP promotes invasion and growth

The percentage of *normal, disrupted, invasive and multi-acinar* colonies cultured in OP are shown in **Fig. 3.5a** *(top)*. The percentage of normal acini was independent of culture condition (*control, ribose, ErbB2,* and *ErbB2 + ribose*). In contrast, the percentage of disrupted colonies decreased significantly ($p < 0.01$) with ErbB2 activation. Additionally, the percentage of *invasive* colonies was greater for *ErbB2 + ribose* as compared to the other conditions, a finding consistent with published work[26] that supports cooperation between the ErbB2 and collagen crosslinking-mediated mechanosensing pathways. Surprisingly, the percentage of *multi-acinar* structures was not dependent on culture condition, an unexpected result considering that two of these culture conditions were without dimerizer. Consistent with our finding, it has been shown that MCF10A.ErB2 cultured in OP without dimerizer spontaneously form *multi-acinar* structures[31]. However, the relative incidence of these structures as a function of the presence or absence of dimerizer has not been previously reported.

The values for the area of *normal* acini were independent of culture condition and homogeneous while the values for the areas of *disrupted, invasive* and *multi-acinar* colonies were significantly greater and more heterogeneous for *ErbB2 + ribose* compared to any other culture

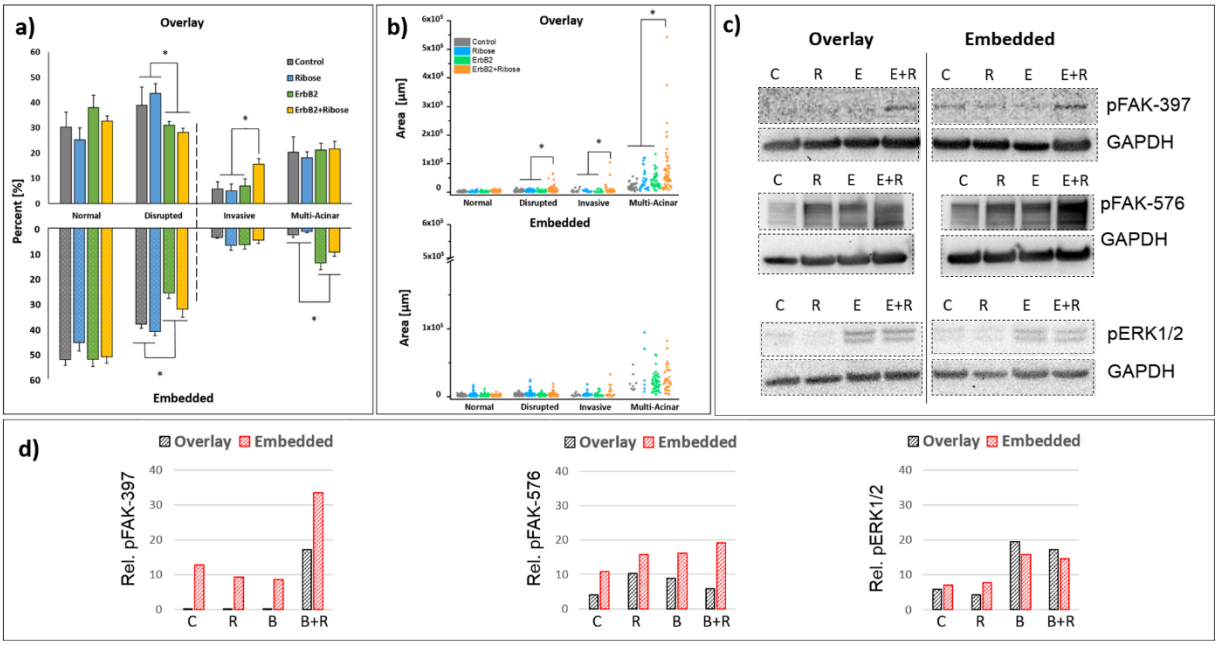

Figure 3.5: *Acinus phenotype for control, ribose, ErbB2 and ErbB2 + ribose conditions.* ***(a)*** *Percentage of acini adopting normal, disrupted, invasive, and multi-acinar morphologies for OP* (top) *and EP* (bottom). *The vertical dashed line separates similar* (left of the line) *and different* (right of the line) *outcomes between the two protocols.* ***(b)*** *Area of acini in the four categories for OP (top) EP (bottom). Horizontal bars indicate grouping of conditions for statistical testing. For percentage of acini, differences were considered significant if p values <.0125 to account for multiple comparisons using a one-sided student's t-test. For area, differences were considered significant for p values <0.05 using a one-sided Mann-Whitney U test. Sample size for EP and OP: 1141 acini and 791 acini, respectively, counted across 3 repeat experiments.* ***(c)*** *Western blot analysis of lysates from MCF10A.ErbB2 cells grown in OP or EP under control [C], ribose [R], ErbB2 [E], and ErbB2 + ribose [E+R] conditions. pFAK-397* (top row), *pFAK-576* (middle row), *and pERK1/2* (bottom row). *Extracts were probed for GAPDH to normalize sample input. p-ERK 1/2 was probed using the streptavidin-biotin sandwich method and the other two with secondary antibodies. Chemiluminescence was used to detect all bands. Experimental conditions were the same across all samples. Blots were cropped for clarity of presentation* (hashed boxes). *Full-length blots are presented in Supplementary Figure 1.* ***(d)*** *Relative expression of each phosphorylated protein normalized to GAPDH from* ***(c)****. At least two blots were analyzed to assess the phosphorylation status of each protein.* ***(c)*** *and* ***(d)*** *are representative of one of the data sets.*

condition (**Fig. 3.5b**, *top*). Larger acini attested to more proliferation in the *ErbB2 + ribose* conditions, further supporting the theory of cooperation between matrix crosslinking and ErbB2 activation in driving tumor growth.

Matrix crosslinking coupled with ErbB2 activation in EP does not promote invasion or growth

As in OP, the percentage of *normal* acini in EP was independent of culture condition and the percentage of *disrupted* acini decreased with ErbB2 activation (**Fig. 3.5a**, *bottom*).

Interestingly, we observed two striking differences in acinus phenotype between EP and OP. First, in contrast with OP, the percentage of *invasive* colonies in EP under the *ErbB2 + ribose* condition did not increase as compared to the three other conditions. Second, the percentage of *multi-acinar* colonies increased significantly with ErbB2 activation as compared to those conditions without ErbB2, only in EP. Additionally, the percentage of *multi-acinar* colonies in the control condition was lower for EP than OP, as previously observed in a study of colonies of MCF10AT cells with activated H-Ras[32]. We speculate that the lower percentage of *multi-acinar* colonies in EP is due, in part, to increased mechanical stresses (relative to colonies grown in OP) resulting from physical confinement within the ECM, as supported by our FEA models. As seen with OP, the area of *normal* acini in EP was independent of culture condition (**Fig. 3.5b,** *bottom)*. However, in contrast to OP, the areas of *disrupted*, *invasive*, *multi-acinar* colonies were not significantly greater for *ErbB2 + ribose* compared to the other culture conditions combined (compare **Fig. 3.5a**, *bottom* to **Fig. 3.5b**, *top*). The differential sensitivity to collagen crosslinking and ErbB2 activation for OP and EP indicates a significant role of the physical asymmetry in determining acinus phenotype, where that role may be more potent than the chemical perturbations.

FAK but not ERK signaling differs between OP and EP

The observations above led us to predict that differences in mechanotransduction-related signaling would be observed between OP and EP. To investigate whether such differences would occur across experimental conditions we monitored expression levels of activated states of key effectors in canonical signaling pathways (**Fig. 3.5c,d**). First, we assayed Focal Adhesion Kinase phosphorylated at Y397 (pFAK-397) and Y576 (pFAK-576) as read-outs of stretch-mediated integrin clustering during the formation of focal contacts, a hallmark of mechanotransduction[33]. FAK is recruited to focal contacts through interaction with the cytoplasmic tails of β1, β3 and β5-

integrins[33]. Once recruited, FAK clusters and is autophosphorylated at Y397[34]. Thus, pFAK-397 is a good indicator of adhesion-mediated mechanotransduction. In OP, pFAK-397 levels were too low to be detected in *control*, *ribose,* or *ErbB2* conditions, but was detectable in the *ErbB2 + ribose* condition (**Fig. 3.5c**, *top*). In contrast, pFAK-397 levels were detected for all four conditions in EP, with the strongest level found in the *ErbB2 + ribose* condition (**Fig. 3.5d**, *left*). pFAK-397 has increased affinity to the SH2 domain of Src, promoting binding to Src, which in turn mediates several additional tyrosine phosphorylation events on FAK, including phosphorylation at Y576 and Y577[34]. Phosphorylation of FAK at these tyrosine residues is actually required to transform the FAK-Src complex into its highest signaling state[35]. Therefore phosphorylation of FAK at Y576 and Y577 is indicative of the full engagement of downstream mechanotransduction-dependent signaling. Similar to our observations with pFAK-397, pFAK-576 levels were greater in EP across all conditions as compared to OP (**Fig. 3.5d**, *middle*). Taken together, these differences in phosphorylation events of FAK support increased adhesion-mediated mechanotransduction in EP as predicted by our model.

We also examined the activation of extracellular regulated signaling kinase 1 and 2 (ERK1/2), which is known to regulate cell proliferation, cell migration[1] and acinus disruption[36]. ERK1/2 is also necessary for the onset of epithelial to mesenchymal transition and invasion in cancer[37]. Levels of pERK1/2, the activated state of ERK1/2, were not different between OP and EP across all conditions (**Fig. 3.5c**, bottom), which was surprising considering differences in colony size (**Fig. 3.4b**). Nevertheless, pERK1/2 levels were low in *control* and *ribose* conditions as compared to *ErbB2* and *ErbB2+Ribose* conditions in both OP and EP (**Fig. 3.5d**, *right*). Matrix crosslinking seemed to play a minor role since acini grown in the *ErbB2* condition already showed maximal pERK1/2 phosphorylation. Together, these data supported a predominant role for

growth-factors in engagement of ERK signaling. In line with our finding, Raghavan et al. have reported that ERK activation in Madin-Darby canine kidney epithelial cells-derived acini does not depend on culture condition dimensionality (monolayer culture or 3D) but rather on the addition of exogenous growth factors[11, 38].

3.4 Discussion

Here we investigated OP and EP for any protocol-dependent effect on acini formation that may impact mechanical hypotheses testing. While it has previously been speculated that OP may result in altered phenotypes as compared to EP[9], our study provides direct evidence for phenotypic differences and for the differences being due to the geometry of the culture system. A novel insight is provided by our data where three independent variables (ECM crosslinking, ErbB2 activation and ECM dimensionality) were tested. Strikingly, our data suggest that ECM dimensionality is the dominant determinant of acini phenotype in our experiments. This is exemplified by the observations that the percentages of *multi-acinar* colonies were independent of culture conditions only in OP and that cooperation between ErbB2 signaling and matrix crosslinking to drive invasion was lost when switching from OP to EP.

The observed phenotypical differences are interesting considering the important roles played by integrins and cadherins in establishing and maintaining MEC polarization and homeostasis[9]. These two molecular families contribute to protein complexes known to transduce forces acting along radial and circumferential axes, respectively. Therefore, cells grown according to OP or EP would be expected to develop into different phenotypes. This expectation follows our finite element analysis which shows that the circumferential and radial forces required to maintain

acinar architecture are very different between OP and EP, even if the material properties of the ECM are identical. In particular, the thin coating of ECM in OP is easily deformed by the contracting acinus, thus maintenance of acinar shape requires small magnitude mechanical stresses as compared to EP. Consequently, stresses acting through integrins and cadherins are dissimilar for otherwise identical OP and EP experiments, and likely lead to differential signaling. This is consistent with our observations of differences in integrin-mediated signaling between OP and EP. Indeed, colonies in OP exhibited lower levels of pFAK-397and pFAK-576 than in EP, indicating that the potential of the ECM to store elastic energy as well as ECM physical symmetry are predominant determinants of force-mediated integrin signaling.

In addition to integrin-mediated signaling, we examined levels of activated ERK (pERK), since ERK activation is often associated with tumorigenesis and cancer progression in humans[39]. Our results support that, in our experimental conditions, adhesion signaling alone is a weak activator of ERK1/2, while ErbB2 signaling remained a potent activator as expected. It has been previously shown that p-ERK levels increase with ErbB2 activation in MCF10A.ErbB2 cells[40], as observed here in both OP and EP across all conditions. Because ERK activation plays a key role in promoting proliferation, we expected the percentage of multi-acinar colonies (**Fig. 3.5a**) to reflect higher p-ERK1/2 levels (**Fig. 3.5d**). While this correlation was confirmed in EP, in contrast, the percentage of multi-acinar colonies in OP was insensitive to ERK1/2 activation and consistently showed high percentages of multi-acinar colonies as compared to EP control.

Of particular note, we also monitored the activation of AKT, which acts downstream of the PI-3 kinase (PI3K) pathway to enhance cell survival[41]. Surprisingly, levels of pAKT, the activated state of AKT, could not be detected by western blot analysis in any of the conditions tested (our unpublished data). It has been extensively documented that the PI3K/AKT pathway is often used

by cancer cells as a back-up to drive tumor progression when the MAPK/ERK pathway is no longer active or is blocked with therapeutics[42, 43].

In conclusion, even though OP has been used to study mechanics in tumor progression using various ECMs[2, 4, 9, 22, 44, 45], EP is more appropriate when considering a model more representative of the relatively homogeneous mechanical environment of the breast. While it is granted that neither method fully recapitulates physiological conditions, the geometry of EP better captures the 3D physical environment in comparison to OP and therefore should be employed when investigating matrix mechanics under uniform mechanical conditions. On the other hand, OP is a superior choice when investigating matrix asymmetry. It is well documented that whereas stiffness is relatively homogeneous in disease-free breast tissue or breast tissue with benign lesions, one can observe steep gradients of stiffness within a tumor[46-48]. In that respect, characterizing the physical differences between an embedded "model" and an overlay "model" is an important component of our understanding of disease progression using 3D culture models.

3.5 Materials and methods

Cell Culture

MCF10A.ErbB2 cells were cultured in 3D conditions with appropriate media formulations[20]. Briefly, cells were first cultured in plastic dishes with Growth medium (5% horse serum, 0.5 μg/ml hydrocortisone, 20 ng/ml human epidermal growth factor (HEGF), 10 μg/ml Insulin, 100 ng/ml cholera toxin, and 100 units of Penicillin/Streptomycin in DMEM/F-12 media). Cells were trypsinized at 70% confluency for 3D culture experiments using a 50/50 Matrigel/Collagen ECM (BD Biosciences). The final collagen concentration was 1.6 mg/ml. Assay

medium (same as Growth medium except 2% instead of 5% horse serum) was mixed with 5 ng/ml HEGF and 2% Matrigel to make OM[9]. For EP, 300 μl of cell suspension (at 70,000 cells/ml ECM) per well was plated in 12-well glass bottom plates (*In vitro* Scientific) and fed with OM. For OP, 2 ml of OM was mixed with 20,000 cells and plated in each well on top of 200 μl of pre-polymerized ECM.

ECM was gelled for 45 minutes in a standard 37°C humidified cell culture incubator with a 5% CO_2 environment. Both EP and OP cell cultures were fed every four days with fresh OM. For the ErbB2 condition, HEGF in assay medium was replaced with 1 μM dimerizing ligand (B/B Homodimerizer, Clontech). For the ribose condition, 15 mM Ribose (Sigma) was added to the assay medium. In the ErbB2+Ribose condition, HEGF was replaced with B/B Homodimerizer and ribose was added to the assay medium. Both dimerizing and ribose media were added starting at week 3 to appropriate dishes with media changes every four days.

Immunocytochemical staining of β-4 integrin was conducted as previously described[20] using a primary mouse anti-human β-4 integrin antibody (Millipore) and a secondary goat anti-mouse antibody coupled to Alexa 488 (Life Technologies). Nuclei were stained with DAPI (Life Technologies). Blocking and antibody incubation were all conducted overnight for EP. Western blots were conducted as described in supplementary materials.

Chimaeric ErbB2 Receptor Dimerizer

MCF10A.ErbB2 cells were obtained from the Muthuswamy laboratory[22]. These cells express a synthetic chimeric transmembrane receptor consisting of a low-affinity growth factor receptor extracellular domain and the cytoplasmic domain of the ErbB2 receptor. The cytoplasmic domain is conjugated to the ligand binding domain of the FK506 binding protein (FKBP), which can be induced to dimerize upon the addition of a synthetic ligand to the culture medium [22]. We

used the B/B dimerizer (Clonetech), also known as AP20187 in place of AP1510 because AP1510 was no longer commercially available. AP20187 was originally synthesized to dimerize Fv domains, which are FKBP proteins bearing a $Phe^{36} \rightarrow Val$ mutation[49]. Although AP20187 binds weakly to FKBP domains, 1μM AP20187 was shown to induce FKBP domain dimerization to a similar extent than that observed with AP1510[49]. We therefore used this 1μM AP20187 concentration to activate dimerization of the chimeric ErbB2 receptor.

Western blot analysis

The protein extraction protocol was adapted from a previously described method[50]. Briefly, after four weeks of 3D culture as described in the methods, culture medium was aspirated from wells and cells were treated with pre-warmed Collagenase Release Solution, consisting of DMEM: F12 (Life Technologies) supplemented with 0.05%Trypsin (Life Technologies), 1% FBS, 200 U/ml Collagenase IV (Life Technologies) and 50 U/ml Dispase (Corning) for 15 minutes at 37°C followed by rigorous pipetting and further incubation for 15 minutes at 37°C. Pipetting and incubation cycle was repeated 3-5 times until a uniform slurry was obtained. The slurry was centrifuged, the supernatant discarded and the pellet resuspended in ice cold PBS containing a cocktail of protease and phosphatase inhibitors (cOmplete ULTRA and phosSTOP tablets, Roche) and centrifuged for 5 minutes at 4°C. This process was repeated twice. The pellet was resuspended in freshly prepared lysis buffer (50 mM Tris-HCl, pH 7.5 (Life Technologies), 150 mM NaCl, 1% v/v IGEPAL CA-630 (Sigma), 5mM EDTA (Life Technologies), and cocktails of protease and phosphatase inhibitors (described above) and incubated on ice for 30 minutes followed by rapid trituration using a 25G x 5/8 syringe needle (Sigma). The obtained cell lysates were centrifuged. The supernatants were reduced with 1mM DTT (Life Technologies), and denatured in NuPAGE® LDS Sample Buffer (Life Technologies) at 100°C for 2 minutes. Cell extracts were loaded in equal

amounts in 4-12% Bis-Tris Plus Gels (Bolt® Life Technologies) and subjected to electrophoresis at 150V for 1.5 hours. Separated proteins were transferred onto PVDF membranes (Bolt®, Life Technologies) overnight at 60mA. Membranes were probed with antibodies against phosphorylated ERK1/2 diluted 1/1000, phosphorylated FAK Y397 diluted 1/1000, phosphorylated FAK Y576 diluted 1/1000 (all from Molecular Probes), or glyceraldehyde 3-phospho dehydrogenase diluted 1/2000 (GAPDH; Cell Signaling) used to normalize sample input. Primary antibodies were either detected with secondary antibodies (**Supplementary Fig. 3.1a, b**) or by employing biotinylated secondary antibody sandwich method (**Supplementary Fig. 3.1c**) for increased signal strength. All blots were detected by enhanced chemiluminescence using ChemiDoc XRS+ (Biorad). A pre-stained molecular weight marker (SeeBlue®; Life Technologies) was used and imaged with epi-white illumination in ChemiDoc.

Active Microrheology

Optical tweezers active microrheology (AMR) was performed as previously described[24]. Briefly, 2 μm diameter carboxylated beads (Bangs Laboratory) were trapped within a focused 1064 nm laser microbeam (IPG Photonics) and oscillated at different frequencies. A 785 nm (World Star Tech) non-steered detection microbeam is deflected by the movement of the bead and corresponds to bead position in time, which is detected by a position sensitive quadrant photodiode. A complex shear modulus can be determined by analyzing the phase-amplitude relationships between the trapping laser and the detection laser positions.

Beads were either embedded within 200 μL of Matrigel or mixed with OM (2.2 ml assay medium + 2% Matrigel) in a 35 mm glass bottom dish. 2 ml of assay medium was added to Matrigel to keep it hydrated. 10-13 beads were measured by AMR at frequencies of 10, 20, 30, 40,

50, 70, 80, 90 and 100 Hz. A custom-built on-stage incubator was used to maintain a temperature of 34°C.

Finite Element Analysis

Numerical estimates of cell-cell and cell-ECM stresses were obtained by Finite Elements analysis. All simulations were performed with the commercial software ABAQUS Standard (Dassault Systemes, US). The acinus was modelled as a thick spherical shell, with internal diameter D=100μm and thickness t=10 μm. In the first set of simulations, an acinus was embedded in a spherical Matrigel shell of thickness ranging from 1 to 100 μm. In the second set of simulations, an acinus was coated with a 1 μm-thick Matrigel layer and partially submerged in a deep Matrigel bed. The penetration depth, *d*, ranged between 0 (acinus just touching the Matrigel bed) and 2 x *D* (acinus deeply submerged in Matrigel bed).

2D axisymmetric quadratic elements were used for both the acinus and the Matrigel, in all simulations. That is, only one quadrant of the circular domain was modelled for EP simulations, with symmetry boundary conditions applied to the symmetry axis (**Fig. 3.2b**). For OP simulations, the bottom side of the block was allowed to deform horizontally, but not vertically. No pressure was allowed to build up during deformation for either simulations since tight junctions of an acinus have been shown to be leaky and allow for transport of interstitial fluid (with the exception of the lactation phase, when a positive pressure can be maintained within the lumen[51, 52]). Both the acinus and the ECM are modelled as linear elastic materials, with a Young's modulus of 720 Pa and 450 Pa, respectively. These values were based on AFM measurements reported in the literature for MCF10A cells[53] and Matrigel[54]. A Poisson's ratio of 0.5 was used for both materials, to simulate a soft incompressible solid.

Contraction of the acinus was simulated by imposing a fictitious coefficient of thermal expansion to the acinus only and prescribing a temperature drop, resulting in a tendency to contract by 10% in all directions. This free contraction is resisted by the constraining effect of the Matrigel, albeit by different amounts in OP and EP simulations. In both cases, a stress field develops in the acinus and Matrigel. Radial and circumferential stresses in the acinus at different locations were extracted and plotted.

MATLAB Acinus Classification Routine

Images were acquired using an Olympus IX81 FluoView 1000 laser scanning confocal microscope. We coded a custom MATLAB (Mathworks) script for classification of acini according to their transmitted light images. The script was designed to blind the user to the experimental conditions the images originated from by randomly calling each image. The graphical user interface (GUI) presents each image to the user who can trace the periphery of each acinus and classify it as *normal*, *disrupted*, *invasive* or *multi-acinar*, visually, using an attached tablet (Wacom Technologies). From each trace, acinus area as well as major axis and minor axis lengths were calculated. Only colonies with areas greater or equal to 490 μm^2 were counted, corresponding to a minimum colony diameter of 25 μm^2. The code then calculates the ratio of major/minor axis length for each *normal* acinus and reclassifies it as d*isrupte*d if the ratio is > 1.3.

Statistical Analysis

Experiments were conducted in triplicates with approximately 60-100 acini counted for each condition. A total of 1411 acini were analyzed across all four experimental conditions for the embedded protocol (EP). An average of 110.3 $\pm$ 31.3 acini per experimental condition were analyzed with 3 replicates. A total of 791 acini were analyzed across all four experimental

conditions for the overlay protocol (OP). An average of 65.9 $\pm$ 19.9 acini per experimental condition were analyzed with 3 replicates.

Differences in rheology, roundness, and colony size were tested for statistical significance using a one-sided Mann-Whitney U test. Differences in percent of acini in each category were tested for statistical significance using one-sided student's T-test. To account for multiple two-sample tests within the same data set, we utilized the Bonferroni correction and divided the alpha value by the number of tests conducted. For testing of the percentage of *disrupted*, *invasive*, and *multi-acinar* colonies, $p < 0.0125$ were considered significant. For testing of G' and G'' values of $p < 0.025$ were considered significant. Roundness and area differences were considered significant for a value of $p < 0.05$.

3.6 References

1. Provenzano, P.P., Inman, D.R., Eliceiri, K.W. & Keely, P.J. Matrix density-induced mechanoregulation of breast cell phenotype, signaling and gene expression through a FAK-ERK linkage. *Oncogene* **28**, 4326-4343 (2009).
2. Paszek, M.J. & Weaver, V.M. The tension mounts: mechanics meets morphogenesis and malignancy. *J. Mammary Gland Biol. Neoplasia* **9**, 325-342 (2004).
3. Seewaldt, V. ECM stiffness paves the way for tumor cells. *Nat. Med.* **20**, 332-333 (2014).
4. Kumar, S. & Weaver, V.M. Mechanics, malignancy, and metastasis: the force journey of a tumor cell. *Cancer Metast Rev* **28**, 113-127 (2009).
5. DuFort, C.C., Paszek, M.J. & Weaver, V.M. Balancing forces: architectural control of mechanotransduction. *Nature reviews. Molecular cell biology* **12**, 308-319 (2011).
6. Lamouille, S., Xu, J. & Derynck, R. Molecular mechanisms of epithelial-mesenchymal transition. *Nature reviews. Molecular cell biology* **15**, 178-196 (2014).
7. Huang, S. & Ingber, D.E. Cell tension, matrix mechanics, and cancer development. *Cancer Cell* **8**, 175-176 (2005).
8. Mizejewski, G.J. Role of integrins in cancer: survey of expression patterns. *Proc. Soc. Exp. Biol. Med.* **222**, 124-138 (1999).
9. Hebner, C., Weaver, V.M. & Debnath, J. Modeling morphogenesis and oncogenesis in three-dimensional breast epithelial cultures. *Annu Rev Pathol* **3**, 313-339 (2008).
10. Ladoux, B. *et al.* Strength dependence of cadherin-mediated adhesions. *Biophys. J.* **98**, 534-542 (2010).
11. Desai, R.A., Gao, L., Raghavan, S., Liu, W.F. & Chen, C.S. Cell polarity triggered by cell-cell adhesion via E-cadherin. *J. Cell Sci.* **122**, 905-911 (2009).
12. Avvisato, C.L. *et al.* Mechanical force modulates global gene expression and beta-catenin signaling in colon cancer cells. *J. Cell Sci.* **120**, 2672-2682 (2007).
13. Ibbetson, S.J., Pyne, N.T., Pollard, A.N., Olson, M.F. & Samuel, M.S. Mechanotransduction pathways promoting tumor progression are activated in invasive human squamous cell carcinoma. *Am. J. Pathol.* **183**, 930-937 (2013).

14. Benton, G., George, J., Kleinman, H.K. & Arnaoutova, I.P. Advancing science and technology via 3D culture on basement membrane matrix. *J. Cell. Physiol.* **221**, 18-25 (2009).
15. Pampaloni, F., Reynaud, E.G. & Stelzer, E.H. The third dimension bridges the gap between cell culture and live tissue. *Nature reviews. Molecular cell biology* **8**, 839-845 (2007).
16. Kunz-Schughart, L.A., Freyer, J.P., Hofstaedter, F. & Ebner, R. The use of 3-D cultures for high-throughput screening: the multicellular spheroid model. *J Biomol Screen* **9**, 273-285 (2004).
17. Griffith, L.G. & Swartz, M.A. Capturing complex 3D tissue physiology in vitro. *Nature reviews. Molecular cell biology* **7**, 211-224 (2006).
18. Bhatia, S.N. & Ingber, D.E. Microfluidic organs-on-chips. *Nat. Biotechnol.* **32**, 760-772 (2014).
19. Fey, S.J. & Wrzesinski, K. Determination of drug toxicity using 3D spheroids constructed from an immortal human hepatocyte cell line. *Toxicol. Sci.* **127**, 403-411 (2012).
20. Debnath, J., Muthuswamy, S.K. & Brugge, J.S. Morphogenesis and oncogenesis of MCF-10A mammary epithelial acini grown in three-dimensional basement membrane cultures. *Methods* **30**, 256-268 (2003).
21. Beck, J.N., Singh, A., Rothenberg, A.R., Elisseeff, J.H. & Ewald, A.J. The independent roles of mechanical, structural and adhesion characteristics of 3D hydrogels on the regulation of cancer invasion and dissemination. *Biomaterials* **34**, 9486-9495 (2013).
22. Muthuswamy, S.K., Li, D., Lelievre, S., Bissell, M.J. & Brugge, J.S. ErbB2, but not ErbB1, reinitiates proliferation and induces luminal repopulation in epithelial acini. *Nat Cell Biol* **3**, 785-792 (2001).
23. Juncker-Jensen, A. *et al.* Tumor MMP-1 activates endothelial PAR1 to facilitate vascular intravasation and metastatic dissemination. *Cancer Res.* **73**, 4196-4211 (2013).
24. Kotlarchyk, M.A., Botvinick, E.L. & Putnam, A.J. Characterization of hydrogel microstructure using laser tweezers particle tracking and confocal reflection imaging. *J Phys Condens Matter* **22**, 194121 (2010).
25. Brau, R.R. *et al.* Passive and active microrheology with optical tweezers. *Journal of Optics a-Pure and Applied Optics* **9**, S103-S112 (2007).
26. Levental, K.R. *et al.* Matrix crosslinking forces tumor progression by enhancing integrin signaling. *Cell* **139**, 891-906 (2009).
27. Erler, J.T. *et al.* Lysyl oxidase is essential for hypoxia-induced metastasis. *Nature* **440**, 1222-1226 (2006).
28. Girton, T.S., Oegema, T.R. & Tranquillo, R.T. Exploiting glycation to stiffen and strengthen tissue equivalents for tissue engineering. *J. Biomed. Mater. Res.* **46**, 87-92 (1999).
29. Cox, T.R. *et al.* LOX-mediated collagen crosslinking is responsible for fibrosis-enhanced metastasis. *Cancer Res.* **73**, 1721-1732 (2013).
30. Baker, E.L., Lu, J., Yu, D., Bonnecaze, R.T. & Zaman, M.H. Cancer cell stiffness: integrated roles of three-dimensional matrix stiffness and transforming potential. *Biophys. J.* **99**, 2048-2057 (2010).
31. Rolland, Y. *et al.* The CDC42-interacting protein 4 controls epithelial cell cohesion and tumor dissemination. *Dev Cell* **30**, 553-568 (2014).
32. Imbalzano, K.M., Tatarkova, I., Imbalzano, A.N. & Nickerson, J.A. Increasingly transformed MCF-10A cells have a progressively tumor-like phenotype in three-dimensional basement membrane culture. *Cancer Cell Int* **9**, 7 (2009).
33. Mitra, S.K. & Schlaepfer, D.D. Integrin-regulated FAK-Src signaling in normal and cancer cells. *Curr. Opin. Cell Biol.* **18**, 516-523 (2006).
34. Westhoff, M.A., Serrels, B., Fincham, V.J., Frame, M.C. & Carragher, N.O. SRC-mediated phosphorylation of focal adhesion kinase couples actin and adhesion dynamics to survival signaling. *Mol. Cell. Biol.* **24**, 8113-8133 (2004).
35. Wang, W., Liu, Y. & Liao, K. Tyrosine phosphorylation of cortactin by the FAK-Src complex at focal adhesions regulates cell motility. *BMC cell biology* **12**, 49 (2011).
36. McHenry, P.R. *et al.* P190B RhoGAP has pro-tumorigenic functions during MMTV-Neu mammary tumorigenesis and metastasis. *Breast cancer research : BCR* **12**, R73 (2010).
37. Debnath, J. & Brugge, J.S. Modelling glandular epithelial cancers in three-dimensional cultures. *Nature reviews. Cancer* **5**, 675-688 (2005).
38. Raghavan, S. *et al.* Decoupling diffusional from dimensional control of signaling in 3D culture reveals a role for myosin in tubulogenesis. *J. Cell Sci.* **123**, 2877-2883 (2010).
39. Adeyinka, A. *et al.* Activated mitogen-activated protein kinase expression during human breast tumorigenesis and breast cancer progression. *Clinical cancer research : an official journal of the American Association for Cancer Research* **8**, 1747-1753 (2002).

40. Seton-Rogers, S.E. *et al.* Cooperation of the ErbB2 receptor and transforming growth factor in induction of migration and invasion in mammary epithelial cells. *Proceedings of the National Academy of Sciences* **101**, 1257-1262 (2004).
41. Guo, W. & Giancotti, F.G. Integrin signaling during tumor progression. *Nature reviews. Molecular cell biology* **5**, 816-826 (2004).
42. Hu, C. *et al.* Opposite regulation by PI3K/Akt and MAPK/ERK pathways of tissue factor expression, cell-associated procoagulant activity and invasiveness in MDA-MB-231 cells. *Journal of hematology & oncology* **5**, 16 (2012).
43. Uzgare, A.R. & Isaacs, J.T. Enhanced redundancy in Akt and mitogen-activated protein kinase-induced survival of malignant versus normal prostate epithelial cells. *Cancer Res.* **64**, 6190-6199 (2004).
44. Lopez, J.I., Mouw, J.K. & Weaver, V.M. Biomechanical regulation of cell orientation and fate. *Oncogene* **27**, 6981-6993 (2008).
45. Yu, H., Mouw, J.K. & Weaver, V.M. Forcing form and function: biomechanical regulation of tumor evolution. *Trends Cell Biol.* **21**, 47-56 (2011).
46. Samuel, M.S. *et al.* Actomyosin-Mediated Cellular Tension Drives Increased Tissue Stiffness and β-Catenin Activation to Induce Epidermal Hyperplasia and Tumor Growth. *Cancer Cell* **19**, 776-791 (2011).
47. Vincent, J.P., Fletcher, A.G. & Baena-Lopez, L.A. Mechanisms and mechanics of cell competition in epithelia. *Nature reviews. Molecular cell biology* **14**, 581-591 (2013).
48. Plodinec, M. *et al.* The nanomechanical signature of breast cancer. *Nature nanotechnology* **7**, 757-765 (2012).
49. Clackson, T. *et al.* Redesigning an FKBP-ligand interface to generate chemical dimerizers with novel specificity. *Proc. Natl. Acad. Sci. U. S. A.* **95**, 10437-10442 (1998).
50. Johnson, K.R., Leight, J.L. & Weaver, V.M. Demystifying the Effects of a Three-Dimensional Microenvironment in Tissue Morphogenesis, in *Methods in Cell Biology*, Vol. Volume 83. (eds. W. Yu-Li & E.D. Dennis) 547-583 (Academic Press, 2007).
51. Shennan, D.B. & Peaker, M. Transport of milk constituents by the mammary gland. *Physiol. Rev.* **80**, 925-951 (2000).
52. Peaker, M. The effect of raised intramammary pressure on mammary function in the goat in relation to the cessation of lactation. *J Physiol* **301**, 415-428 (1980).
53. Nikkhah, M., Strobl, J.S., Schmelz, E.M. & Agah, M. Evaluation of the influence of growth medium composition on cell elasticity. *J. Biomech.* **44**, 762-766 (2011).
54. Soofi, S.S., Last, J.A., Liliensiek, S.J., Nealey, P.F. & Murphy, C.J. The elastic modulus of Matrigel as determined by atomic force microscopy. *J. Struct. Biol.* **167**, 216-219 (2009).

Chapter 4

Method to measure pericellular stiffness in natural extracellular matrices

Abhishek Kurup[1, †], Mark Keating[1, †], Martha Alvarez-Elizondo[2], Elliot L. Botvinick[1,]

[1] University of California, Irvine, Department of Biomedical Engineering, Irvine, 92617, USA
[2] Technion, Israel Institute of Technology, Department of Biomedical Engineering, Technion City, 32000, Israel
[†] These authors contributed equally to this work;

4.1 Introduction

Interactions between cells and their extracellular matrix (ECM) are bi-directional. On one hand, the mechanical properties of the ECM have been shown to regulate key processes in cells; for example, increasing bulk ECM stiffness can promote invasion of mammary epithelial cells[1], differentiation of mesenchymal stem cells[2, 3], and maturation of cardiomyoctes[4]. On the other hand, cells actively alter their ECM through context-dependent degradation, remodeling, and deposition of new ECM[5]. Thus, quantifying the mechanical interactions between the cell and ECM both spatially and temporally is imperative in understanding how cells are regulated in physiological and pathological processes.

One piece of the puzzle in cell-ECM physical interactions is the distribution of traction forces exerted by cells onto their local ECM. 3D traction force microscopy (TFM) has been developed for cells fully embedded within a linear, homogenous, nano-porous, synthetic PEG hydrogel[6, 7], which can be modified to contain sites for cell adhesion and cell-mediated degradation[8]. Because these hydrogels have homogenous stiffness, cell-mediated traction forces can be computed from the displacement of embedded tracer beads using finite element analysis.

However, these gels do not share the native architecture, pore size, or nonlinear properties of natural matrices[9], potentially causing cells to remodel these ECMs differently than they would natural ones. Efforts to extend TFM to natural matrices have been hindered by heterogeneities in local stiffness, particularly in the pericellular space. It has been reported that stresses cannot be determined from bead displacements alone under the assumption of homogenous mechanical properties[7] or without accounting for local degradation[10]. Furthermore, stiffness of natural fibrous matrices increases non-linearly with deformation, and cannot be determined from collagen concentration alone[7, 11]. Stiffness can be potentially determined from strain if the nonlinear relationship between strain and stiffness is known for the material. However, this requires knowledge of the current stress free state, which is dynamic with cell remodeling. Thus, the instantaneous distribution of ECM stiffness remains elusive. Moreover, the stress free state may not be determinable at arbitrary time points without sacrificing the tissue culture via a detergent[6] or trypsin[12] to remove residual stresses, thus precluding longitudinal study.

We assert the dynamic measurement of pericellular stiffness in natural fibrous matrices will reveal important new insights regarding roles of cell contractility, degradation, and remodeling on the distribution of ECM stiffness and regulation of cells. In support of this claim, we have previously used a rudimentary form of the method presented in this paper to measure changes in pericellular stiffness[13, 14]. At the time, our method was highly technical and laborious, but nonetheless critical to gaining new insights into morphogenesis. For example, we found that during capillary morphogenesis the pericellular space surrounding the tip of a sprouting capillary had increased stiffness as compared to distal regions, and that stiffness correlated with increased local ECM deformation[13]. We also showed that mouse skeletal stem cells required MMP14 activity

to stiffen the pericellular space within 3D collagen gels, a result that was associated with osteogenic fate commitment *in vivo*[14].

4.2 Development and validation

We have developed a new tool we call automated active microrheology (aAMR) based on the method used in those studies. aAMR delivers real-time measurement of pericellular ECM shear modulus around cells cultured within natural ECMs. It relies on optical tweezers active microrheology (AMR), which directly measures the complex valued material properties within natural ECMs[15, 16]. In our method, cells are embedded within an ECM that also contains a dispersion of 2 μm diameter silica microbeads. Each microbead is bound within the hydrogel and oscillated by optical tweezers forces (**Fig. 4.1a**). Our optical tweezers system is integrated into a laser scanning confocal microscope so that the sample can be imaged by trans illumination (brightfield) microscopy to visualize cells and their surrounding beads (**Fig. 4.1b**) as well as confocal microscopy, which, by back-reflection, provides label-free images of cells and ECM architecture (**Fig. 4.1c-d**).

In AMR, both the real and imaginary components of the complex material response function α are computed from experimental data with no simplifying assumptions regarding thermodynamic equilibrium. The real component of α relates to the stiffness, whereas the imaginary to viscous losses. In contrast to AMR, commonly used methods of passive microrheology operate on the thermally driven motion of beads from which only the imaginary component of α can be directly determined. However, the calculation of the real component of α only holds for samples in thermodynamic equilibrium[17], which is not the case for live cells exerting forces on the ECM. In fact, it has been shown that passive microrheology overestimates

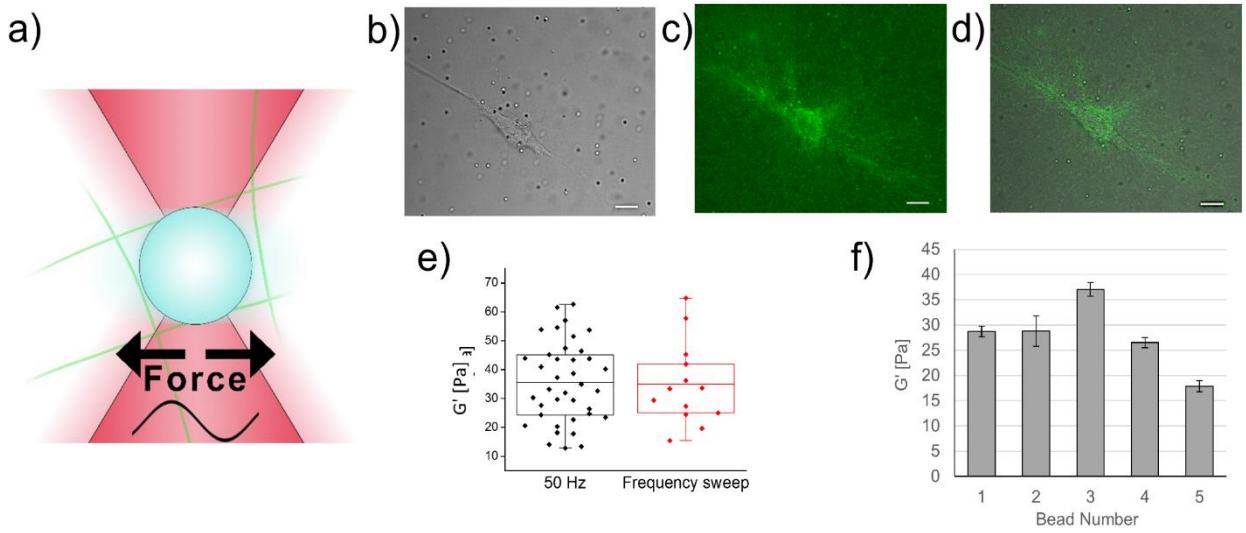

Figure 4.1: *Automated optical tweezers active microrheology* (aAMR). ***(a)*** *The optical tweezers microbeam (red) is spatially oscillated to exert oscillatory forces on a microbead (cyan) and forces are resisted by local extracellular matrix (green) elastic and viscous forces. Signals are analyzed to compute the complex valued shear modulus G.* ***(b)*** *Brightfield image of an isolated HAoSMC cultured in a 2.0 mg/ml type 1 collagen gel embedded with 2 µm diameter silica microbeads.* ***(c)*** *Reflection confocal microscopy image of the region in* ***(b)*** *showing both the cell and the fibrous collagen matrix.* ***(d)*** *Merged brightfield and confocal images.* ***(e)*** *G' measured in a 2.0 mg/ml collagen gel as determined by either* (i) *oscillating the optical tweezers at single oscillation frequency (50 Hz, n = 37) or* (ii) *as the average G' across a frequency sweep of 10, 20, 50, 75, and 100 Hz (n = 13). No significant differences were detected between the two measurements (p > 0.8).* ***(f)*** *G' values for five beads chosen at random in 2.0 mg/ml collagen gel and separated by at least the range of the piezoelectric x-y stage (~100um). The automation system cycled between the five beads five times. Scale bars are 20 µm.*

compliance for hydrogels not in thermodynamic equalibrium[18] and consequently underestimates ECM stiffness. Therefore, passive microrheology for measurement of pericellular stiffness has been limited to either detection of the formation or dissolution of a hydrogel[19] or to ECMs that are orders of magnitude softer than *in vivo*[20, 21]. Important to our method, AMR does not require the system to be in thermodynamic equilibrium[17] and can measure samples with stiffness up to 1000 Pa. Furthermore, if the continuum assumption is applied to the local ECM, then the shear modulus G can be computed from α using the generalized Stokes Equation (**Chapter 2.4**), as previously reported[17]. It must be noted that the continuum assumption breaks down in porous fibrous natural materials using micron-diameter probe particles. However, because the conversion between α and

G is reversible (**Chapter 2.4, eq. 6**), and *G* is a ubiquitous parameter in the study of soft tissue mechanics, we choose to report *G*.

Our method of aAMR implements robotic control of a standard microscope and opto-electronic components for AMR measurements of pericellular stiffness (**Chapter 2**). aAMR reduces the time required to probe each bead by a factor of 10, specifically from 2-3 minutes per bead to approximately 20 seconds per bead. The reduction in time is achieved in two ways. First, and primarily, time is reduced by robotic control of imaging and microscope hardware components for determination of bead centroid coordinates in 3D and movement of the two microscope stages to precisely place each bead in the optical trap. Secondly, time is reduced by only oscillating each bead at 50 Hz as opposed to the commonly implemented frequency sweep. In support of probing at 50 Hz alone, previous studies have reported that *G'* is frequency independent in type 1 collagen gels at frequencies <100 Hz [22] and we further determined no difference in *G'* measured by frequency sweep or at 50 Hz alone (**Fig. 4.1e**).

To validate aAMR we first conducted AMR in water at room temperature with a frequency sweep at [10 20 50 75 100] Hz. Viscosity, η, in water is empirically known to be 0.001 Pa s and can be determined by AMR using the relationship $\eta = G''/2\pi f$, where f is the frequency of oscillation[23]. We measured viscosity to be $0.001 \pm 5.76 \times 10^{-5}$ Pa s, which agrees with the empirical value ($n_{beads}=5$; $p = 0.975$). We next investigated potential sources of error originating from hardware automation by probing beads in a hydrogel (type 1 collagen). Each bead was positioned at laser focus using both a course (stepper stage, approximately 1 μm resolution) and fine (piezoelectric stage, < 1 nm resolution) microscope XY-stage as well as the motorized objective turret of the microscope stand, as guided by image processing. We randomly selected beads ($n = 5$) separated from each other by at least 75 μm. At this distance the automation system must move

both the long-range stepper motor stage as well as the piezoelectric stage to center a bead within the optical trap with 0.10 μm repeatability. The aAMR system cycled between all beads five times (**Fig. 4.1f**) to measure *G'*. On average, the percent error between the standard deviation and the mean of *G'* across all five measurements was 5.5%, demonstrating the small error introduced by our automation.

4.3 Measurement of pericellular stiffness reveals significant cellular remodeling

To demonstrate measurement of pericellular stiffness we cultured Human Aortic Smooth Muscle Cells (HAoSMCs) in type 1 collagen gels (2 mg/ml) containing 2 μm diameter microbeads at 0.8 mg/ml. On average, each bead was located approximately 13 μm from its neighbors. aAMR measurements were conducted approximately 30 μm above the glass coverslip in a 350 x 280 μm^2 region surrounding HAoSMCs. **Figure 4.2a** shows two cells surrounded by significantly stiffened regions (*blue box*; $n_{beads} = 42$) compared to cell-free regions (*yellow box*; $n_{beads} = 30$) within the image montage ($p = 1.4 E-7$). We next investigated if inhibition of cell contractility would result in pericellular softening. We treated these cell with the ROCK inhibitor Y27632, previously shown to result in a significant loss in contractility (within 15-30 minutes) for human uterine smooth muscle cells[24]. aAMR was conducted on the same beads (see conditions for excluding beads in **Chapter 4.9**) probed in **Figure 4.2a** following a one hour on-stage incubation with Y27632-supplemented media (**Fig. 4.2b**). Measurements show a notable loss in spatial heterogeneity of *G'* as compared to pre-treatment as well as a significant decrease in the mean value of *G'* (213 ± 65 Pa and 65 ± 60 Pa, before and after treatment respectively; $p < 0.001$; **Fig. 4.3**). Note the handful of beads between cells 2 and 3 that reported stiff ECM before treatment (**Fig. 4.2c**), but did not soften as compared to their neighbors after Y27632 treatment (**Fig. 4.2d**). We imaged this region

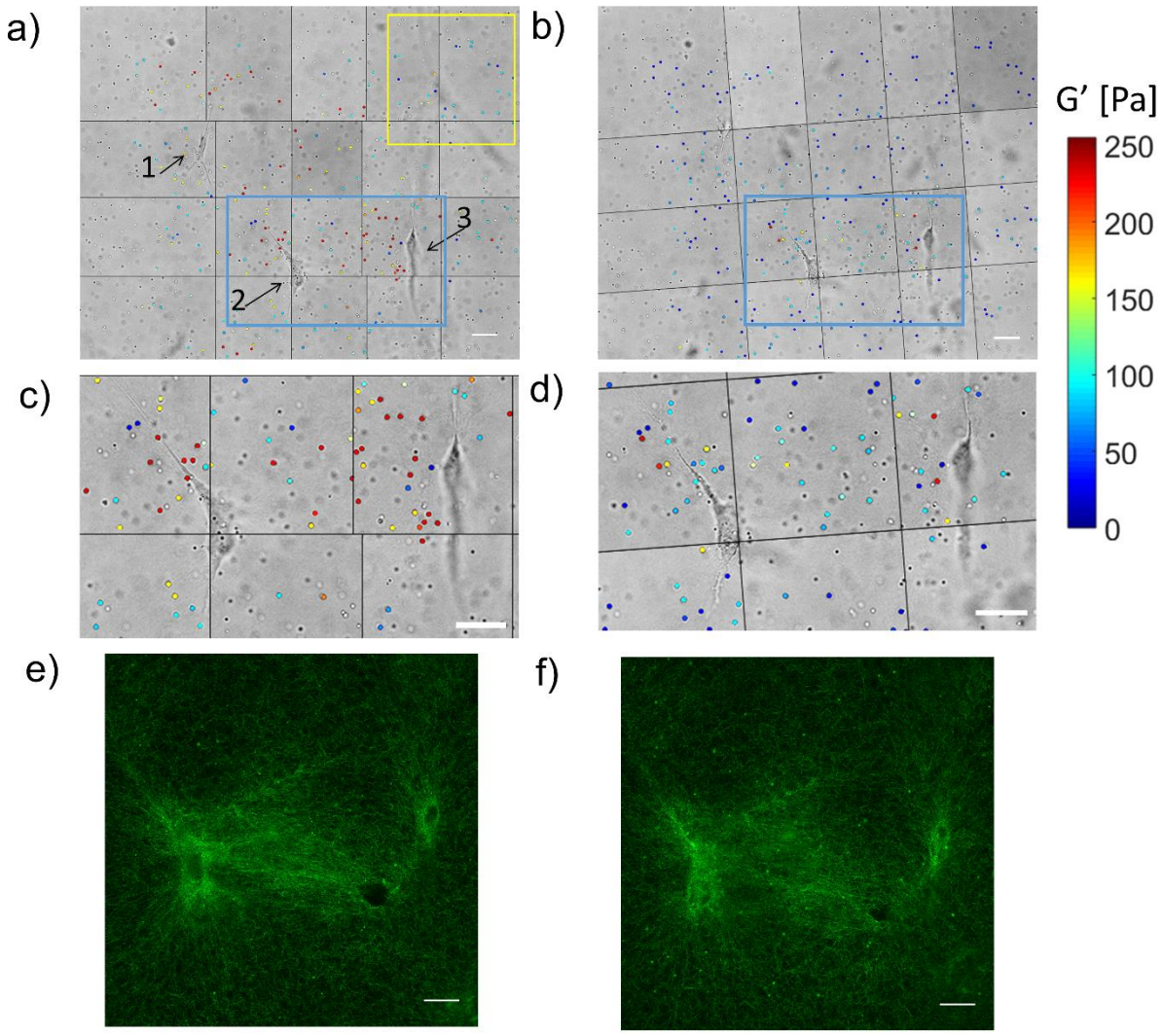

Figure 4.2: *Mapping pericellular stiffness with aAMR.* ***(a)*** *Montage of multiple fields of view in a 2 mg/ml type 1 collagen gel embedded with 2 µm diameter microbeads and containing HAoSMCs (labeled 1, 2, and 3). Microbeads probed for aAMR are overlaid with a colored circle corresponding to the measured G'.* ***(b)*** *G' decreased significantly between control (n = 288 beads) and Y27632 (n = 279 beads) treatment (p << 0.001).* ***(c, d)*** *Cropped and zoomed-in region bound by blue rectangle in* ***(a)*** *and* ***(b)****, respectively.* ***(e, f)*** *Reflection confocal images between cells 2 and 3 before and after treatment with Y27632, respectively. Scale bars are 20 µm.*

by reflection confocal microscopy and observed fiber alignment pre-treatment (**Fig. 4.2e**). Confocal imaging after treatment (**Fig. 4.2f**) shows that the 3-fold decrease in average ECM stiffness correlated with relaxation, but not abatement, of fiber alignment (**Fig. 4.2f**). In fact, the collagen density between the two cells remained high after treatment suggesting roles for cell-

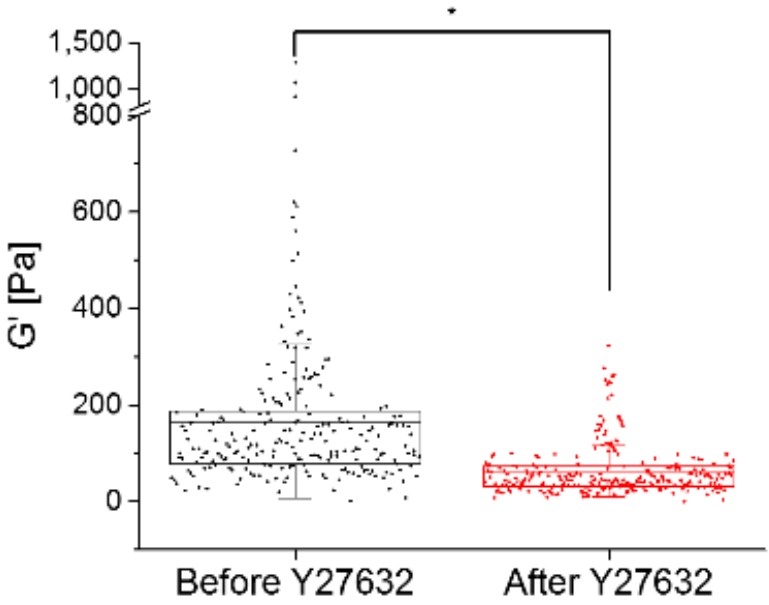

Figure 4.3: *aAMR measurements of G' in 2 mg/ml type 1 collagen gels around multiple HAoSMCs. G' values significantly decreased after treatment ($p << 0.001$; $n=279$) as compared to before treatment ($n=288$). Note the break in the y-axis at 800 Pa.*

mediated local remodeling and providing direct evidence that stiffness may be insensitive to collagen concentration.

4.4 Average pericellular stiffness depends on MMP activity and cell contractility

We next studied effects of cell contractility and local remodeling on pericellular stiffness. aAMR was conducted around isolated HAoSMCs in control conditions as well as those treated with Y27632 and Batimastat (aka BB94), a wide-spectrum inhibitor of matrix metalloproteinases (MMPs). To determine any direct effects of the drugs on the matrix, we first conducted aAMR in cell-free gels. No significant changes in *G'* were measured in gels treated with Y27632 for one hour ($p = 0.44$) or gels treated with Y27632 after overnight treatment with BB94 ($p = 0.74$) as compared to control gels (**Fig 4.4a**).

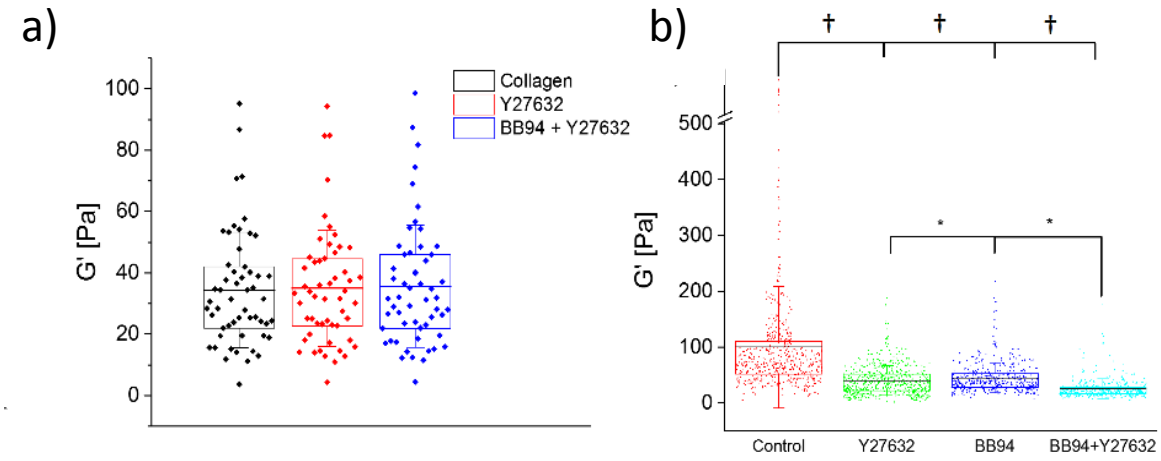

Figure 4.4.: aAMR measurements in type 1 collagen gels. ***(a)*** *aAMR measurements of G' in cell-free 2 mg/ml type 1 collagen gels under control conditions (n = 58), as well as treatment conditions Y27632 (n= 58) and BB94+Y27632 (n= 58). Control conditions were not significantly different from Y27632 (p = 0.44) or BB94+Y27632 (p = 0.74) conditions.* ***(b)*** *aAMR measurements of G' in a ~280 x 280 μm^2 region surrounding isolated HAoSMCs in control conditions (n_{cells} = 3; n_{beads} = 506) as well as treatments with Y27632 (n_{cells} = 4; n_{beads} = 583), BB94 (n_{cells} = 3; n_{beads} = 428) and BB94+Y27632 (n_{cells} = 3; n_{beads} = 417). Each experimental condition was significantly different as compared to control (†, p << 0.001). Additionally, BB94+Y27632 was different as compared to Y27632 and BB94 (*, p << 0.001). Statistical testing was conducted with Mood's Median test and alpha values 0.025 and 0.083 for* ***(a)****, and* ***(b)*** *respectively to account for multiple comparisons via the Bonferroni correction.*

The pericellular stiffness surrounding isolated HAoSMCs was measured in four conditions: *(1)* control, *(2)* Y27632, *(3)* BB94 or *(4)* both BB94 and Y27632. For each condition pericellular stiffness was measured for at least three isolated cells. For conditions *(3)* and *(4)*, BB94 was added just after gelation before overnight incubation. For conditions *(2)* and *(4)*, Y27632 was added after overnight incubation one hour prior to measurements. As compared to control, average *G'* in the probed region decreased in all three experimental conditions ($p < 0.001$; **Fig 4.4b**). Additionally, average *G'* for condition (4) was lower than that for conditions (2) and (3) ($p < 0.001$), showing that dual-inhibition was most effective at softening the pericellular ECM relative to control.

4.5 Spatial distributions of pericellular stiffness provide new insights regarding roles of MMP activity and cell contractility in elastic and plastic ECM deformation

In order to aggregate pericellular stiffness distributions across multiple cells we first, transformed the Cartesian coordinates of each bead into a polar coordinate system (r, θ), with origin at the cell centroid. Then, all points were rotated such that the major axis of the cell (determined by a bounding ellipse) pointed along $\theta = 0$. Pericellular stiffness for all cells in each condition could be a spatially aggregated this way for statistical analysis (**Fig. 4.5a-d**). The decrease in stiffness and loss in spatial heterogeneity as compared to control is evident for all three treatment conditions. Differences in the distribution of *G'* are emphasized in 3D surface plots generated by interpolation between probed beads using the MATLAB *griddata* function, which implements triangulation-based linear interpolation with 1 μm node spacing (**Figures 4.5e-h)**. We next computed S_d, the shortest distance between each probed microbead and the boundary of its corresponding cell. **Figures 4.5i-*l*** show *G'* plotted on a (S_d ,θ) coordinate system to visualize relationships between ECM stiffening, cell orientation, and distances from cells across experimental conditions.

G' was elevated under control conditions (**Fig. 4.5i**), in a continuous region found within $S_d < 50$ μm and $-90° < \theta < +90°$, which contains the leading edge of each cell. Discrete punctate regions of elevated *G'* values were also found in this angular region for values of $S_d > 50$ μm, demonstrating that long range stiffening may not be a spatially continuous process, but dependent on the fibrous network[25] and/or the asymmetry[26] by which cells contract against their matrix. Supporting this hypothesis, inhibition of cell contractility by Y27632 (**Fig. 4.5b,f,j**) resulted in a significant decrease in pericellular stiffness and stiffness asymmetry as compared to control (**Fig. 4.5a,e,i**). Note the region for $S_d < 50$ μm is no longer stiffened compared to regions for $S_d > 50$ μm

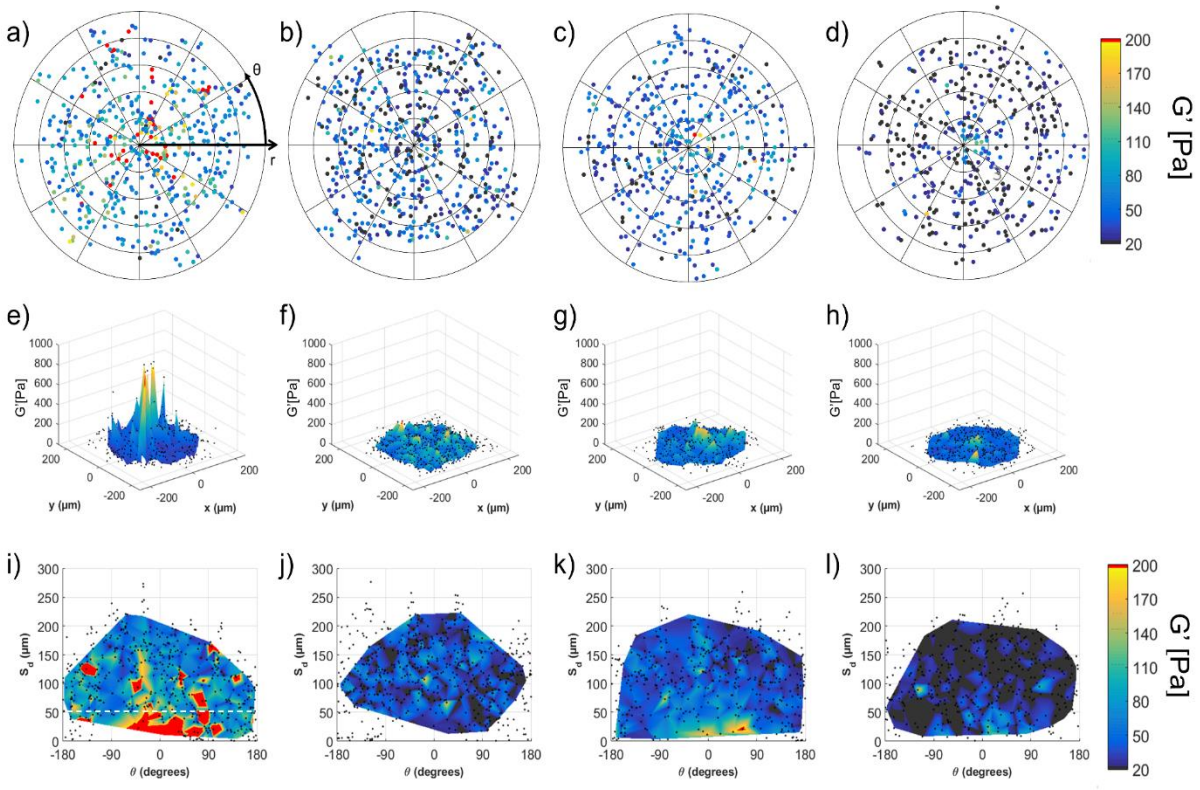

Figure 4.5: *Characterization of pericellular stiffness for multiple isolated cells. Polar plots of G' surrounding isolated cells for **(a)** control (n= 3), **(b)** Y27632 (n = 4), **(c)** BB94 (n = 3) and **(d)** BB94+Y27632 (n = 3) conditions. Concentric lines are drawn in 50 µm increments of r. **(e-h)** 3D surface plots of the aggregate data in **(a-d)**, respectively. **(i-l)** Data in **(a-d)** mapped to a Cartesian plot of θ vs. distance from cell boundary, S_d. White dotted line in **(i)** marks S_d = 50 µm. Probed beads are denoted by black dots. Display of interpolated data is confined to regions containing data from all cells, per condition. Color maps in (**a-d** and **i-l**) range approximately from the average G' value of BB94+Y27632 to the average G' value plus one standard deviation of the control condition.*

(**Fig. 4.5j**). Together, these observations implicate the important role of cell contractility-mediated strain hardening in determining the mechanical landscape in the pericellular space.

We also found that inhibition of MMP activity by BB94 (**Fig. 4.5c,g,k)** lowers *G'* values relative to control but preserves asymmetry (**Fig. 4.5k**), with larger values of *G'* also located between S_d < 50 µm and -90° < θ < +90°. This result is consistent with the action of BB94, which does not target actin-myosin interactions and thus should not directly inhibit contractility. Subsequent incubation with Y27632 (**Fig. 4.5l**) abolishes the stiffened regions observed for cells

incubated in BB94 alone (**Fig. 4.5k)**, suggesting stiffening was elastic and likely tension mediated. The results also show that MMP activity (**Fig. 4.5b,f,j**) or cellular contractility (**Fig. 4.5c,g,k**) alone are insufficient in creating asymmetric and long range stiffening as observed in control (**Fig. 4.5a,e,i**). Rather, it is the cooperation between both MMPs and cellular contractility that are required for creating a normal mechanical topography.

4.6 Considerations regarding stiffness heterogeneity

If cellular traction forces and pericellular stresses are to be computed from bead displacements, then values of *G'* at all points must be interpolated between probed beads. In light of the stiffness heterogeneity observed in **Figure 4.5**, we analyzed the absolute differences in *G'* between neighboring beads. For each bead, we determined d_i, the center-to-center distance to its closest neighbor (eliminating redundant pairs), and $\Delta G'$, the difference in *G'* reported by those beads **(Fig. 4.6a)**. The lower limit of *d* is 2 μm, which occurs only if two beads are in contact. Histograms of $\Delta G'$ (**Fig. 4.6b-f**) demonstrate the effects of cell contractility and MMPs on local stiffness variability in the pericellular space. The third quartile for a cell-free collagen gels was found to be 20 Pa (**Fig. 4.6b)** as compared to 60 Pa for control cells (**Fig. 4.6c**, a factor of 3 increase). Notice the outliers for control cells showing that the stiffness reported by neighboring beads can be different by as much as 700 Pa. In contrast, while the pericellular $\Delta G'$ for cells treated with Y27632 **(Fig. 4.6d)**, BB94 **(Fig. 4.6e)** or both **(Fig. 4.6f)** have outliers as high as 150 Pa, the third quartile values were found to be 30, 30 and 10 Pa respectively.

We next examined whether the distance of a bead from the cell affects the relationship between $\Delta G'$ and d_i (**Fig. 4.6g-k**). In control conditions, even bead pairs found within 50 μm of the cell boundary (**Fig. 4.6g,** *red markers*) that are separated by 5 μm or less, report $\Delta G'$ values as

large as 200 Pa. Such large values of $\Delta G'$ are also found beyond 50μm from the cell boundary (**Fig. 4.6g**, *black markers*), indicating that long-range stiffening also generates large local differences in G'. Cells treated with Y27632 (**Fig. 4.6h),** BB94 (**Fig. 4.6i),** or both **(Fig. 4.6j)** had reduced values of pericellular $\Delta G'$. Furthermore, $\Delta G'$ values for small d_i were well below 100 Pa and independent of bead location, as also observed in cell-free gels **(Fig. 4.6k)**.

The impact of G' differentials can be understood by estimating the force magnitude, F, required to displace a bead by distance x, where $F = x/\alpha$. We estimated values of F under a simplifying assumption that α, and therefore G', will not change for small bead displacements. Although we have data to contradict this assumption (not shown), our analysis will still provide insight into the importance of observed $\Delta G'$ values. We also ignore the effects of viscoelastic creep and stress relaxation, again only for the purposes of this quasi-quantitative analysis. In **Table 4.1**, we tabulated estimated force magnitudes acting on a bead for all values of $G' \in$ [10, 30, 50, 100, 1000] Pa, a range observed for control cells (**Supplemental Fig. 4.1c**), which also corresponds to $1/\alpha \in$ [0.2, 0.4, 1, 2, 13, 19] nN/μm.

The estimates of F for x = 1 μm and 5 μm are consistent with previously reported bead displacements surrounding single HT-1080 cells in a 2 mg/ml type 1 collagen gel[10]. F ranged from 0.2 to 95 nN around a single cell (Supplementary Table 1), which spans the range of traction forces reported from experiments using the two-dimensional (2D) micropillar technique[27, 28]. Jin et al. computed cell contractile forces in 3D ECMs by monitoring the contraction of a 1.8 mg/ml type 1 collagen gel seeded with human aortic adventitial fibroblasts. They estimated the average cell contractile force was approximately 1.5 nN, which is well within our range of estimated forces[29].

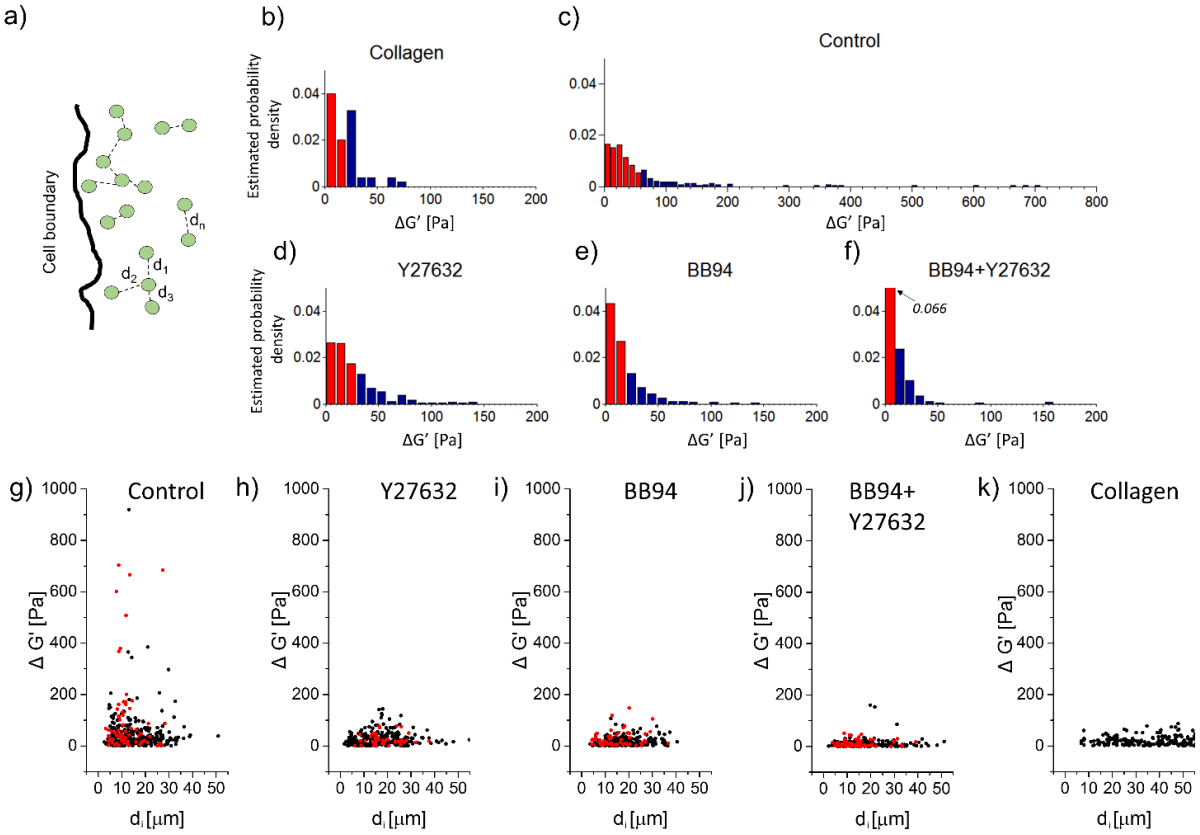

Figure 4.6: *Variability in stiffness between adjacent beads.* ***(a)*** *For each bead, d_i is the distance to its closest neighbor. Estimated probability density of ΔG' in* ***(b)*** *cell free collagen and collagen gels containing HAoSMCs under* ***(c)*** *control conditions or treatment with* ***(d)*** *Y27632,* ***(e)*** *BB94 or* ***(f)*** *both. Area under the red bars = 0.75.* ***(g-h)*** *Scatter plots of d_i and ΔG' for HAoSMCs under* ***(g)*** *control conditions or treatment with* ***(h)*** *Y27632,* ***(i)*** *BB94 or* ***(j)*** *both. Red dots indicate beads within $S_d \leq 50$ μm and black dots indicate beads within $S_d > 50$ μm.* ***(k)*** *Scatter plots of d_i and ΔG' for a cell-free collagen gel.*

Bloom et al. tracked displacements of 3.6 μm diameter beads around HT-1080 cells in a 2.0 mg/ml type 1 collagen gel. They estimated that a 4 nN force is required to displace a bead by 5 μm[10]. Both studies assume *G'* is homogenous and equal to bulk values. But, as seen in our experiments, *G'* ranged from tens to one thousand Pa around a single cell, meaning the estimated magnitude of force required to displace a bead by 5μm could range between 1 and 95 nN. This demonstrates forces calculated from bead displacement under the assumption of homogenous stiffness can be incorrect by at least one order of magnitude. Given this new insight, we caution the use of bead-

based TFM in fibrous gels unless stiffness is determined continuously throughout the pericellular space.

Table 4.1: *Estimates of force magnitude required to displace a bead by 1 or 5 μm in a gel with given G' and α'.*

$G'[Pa]$	$1/\alpha'\ [nN/\mu m]$	$F\ [nN]$	
		$\Delta x = 1\mu m$	$\Delta x = 5\mu m$
10	0.2	0.2	1
20	0.4	0.4	3
50	1	1	5
100	2	2	10
200	4	4	20
1000	20	20	100

4.7 Discussion

Quantification of the effects of cell contractility, remodeling, and fiber mesh architecture on the pericellular stiffness in a natural fibrous ECM at physiological concentration has only been modeled[30] or qualitatively assessed[19] within the volume of a fibrous hydrogel, but not directly measured as is possible with aAMR. Our method and analyses are generalizable to many tissue engineering systems because they are independent of ECM composition and cell type. Additionally, universal metrics such as cell migration velocity, morphology, live-protein localization, and fiber matrix architecture can be easily incorporated into our method. aAMR is

ultimately limited by the maximum detectable stiffness (~1 kPa) as well as bead density, which is not only restricted by pore structure and bead size, but also by the fact that the ECM properties will change with excessive loading of microbeads. Importantly, because our technique was designed to work in natural fibrous ECMs, we have enabled new studies of cell-matrix physical interactions previously restricted to non-physiological, synthetic, nano-porous ECMs.

There is a growing literature reporting correlations between bulk ECM stiffness and cell phenotype in tissue models including progenitor cell differentiation[31], regulation of cell colony size[32], and signaling pathways that regulate tumor growth[33]. Cells in these experiments are seeded within a set of ECMs, each with unique but homogenous bulk stiffness. Remarkably, the entire range of those stiffness values was observed surrounding a single cell in a collagen gel as measured by aAMR. This begs the question: which stiffness value is important? We speculate that no single value of stiffness guides cells in physiological conditions, rather it is the evolution and distribution of stiffness that is important. These processes can be studied in tissue models by aAMR, which any laboratory having skills in microscopy and photonics can replicate.

4.8 Materials and methods

Cell Culture

Human Aortic smooth muscle cells (HAoSMCs) were acquired from ATCC (PCS-100-012) and the media plus bullet kit (CC-3182) from Lonza. 2 mg/ml collagen (Corning) samples were prepared with 10x PBS (Life technologies), 1N NaOH (Fisher), DI H_20, 2 μm beads (0.8 mg/ml, Bangs Laboratories) and HAoSMCs (100 k/ml) in 35 mm glass bottom dishes (MatTek). The polymerization process was conducted in a standard tissue culture incubator at 37 °C (except for **Figure 4.1e**, which was gelled at 27 °C) for 40 minutes, after which media was added to each

dish. Control conditions were fed with normal media at the time of gelation. BB94 conditions were fed with normal media supplemented with 10 μM Batimastat (Sigma) after gelation. All dishes were incubated overnight in a standard tissue culture incubator. On the day of the experiment, sample media was supplemented with HEPES (25 mM) and the dish placed within the microscope piezo-electric insert. A custom-built incubation system plus an objective heater maintained temperature in the dish at 34 °C. Gels were allowed to equilibrate to temperature for at least 1 hour to prevent focus drift[34]. Y27632 conditions were supplemented with 20 μM Y27632 (Sigma) during this incubation period.

Statistical Analyses

All statistical analyses were conducted in OriginPro using the Mood's median test because data was not normally distributed. The alpha value used to determine statistical significance was adjusted in the cases of multiple comparisons according to the Bonferroni correction, where alpha is divided by the number of multiple comparisons. For the case of viscosity measurement in water, comparison was made by the Student's T-test.

4.9 AMR automation algorithm

All software modules of aAMR were developed in LabVIEW2012 with the NI Vision package. A screenshot of the automation software interface is shown in **Figure 4.7a** and a flow chart of the automation sequence is depicted in **Supplementary Figure 4.7b**. The automation software is broken down into modules explained below.

Module 1: Coarse centering of beads in the optical trap

At the start of experiments the user uses a mouse to manually click on all the beads to be probed. To convert the clicked positions into the precise (x,y) coordinate of each bead, a 60 pixel

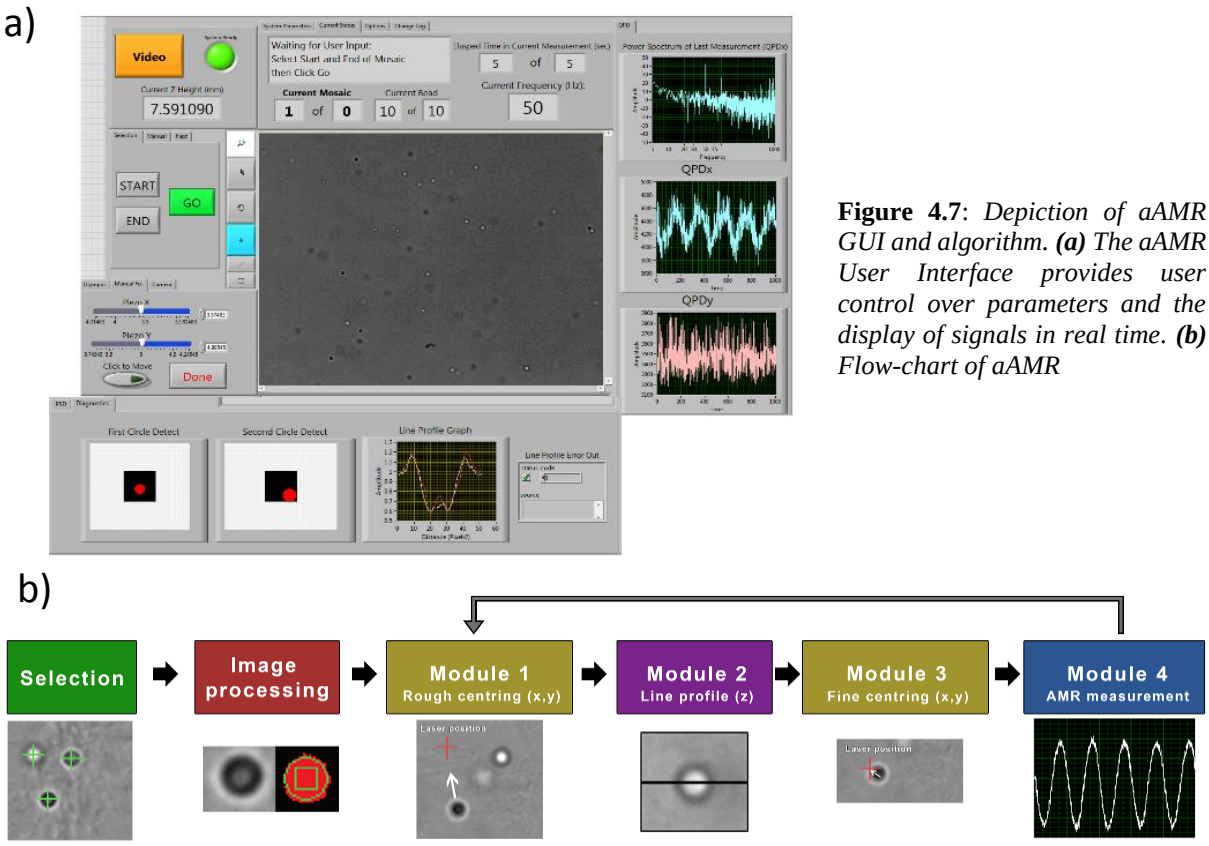

Figure 4.7: *Depiction of aAMR GUI and algorithm.* ***(a)*** *The aAMR User Interface provides user control over parameters and the display of signals in real time.* ***(b)*** *Flow-chart of aAMR*

x 60 pixel region of interest (ROI) is programmatically cropped around each mouse click (**Fig. 4.8a**). The size of the ROI was chosen to be large enough to ensure the entire 2µm bead (diameter ~ 20 pixels) is within the ROI. An edge-enhanced image is computed using the Sobel edge detection algorithm (**Fig. 4.8b**) from which a binary image mask is computed using the *NI IMAQ Background Correction* algorithm with a 32x32 window. Pixels in the outer edge of the bead diffraction pattern are 'true' in the resulting binary image (**Fig. 4.8c**). The binary image often contains pixel noise which is removed by the *NI IMAQ RemoveParticle* algorithm (**Fig. 4.8d**). Next, the mask is filled in using the *NI IMAQ Convex Hull* tool (**Fig. 4.8e**). The *NI IMAQ Find Circles* algorithm detects the centroid of the circle corresponding to the bead center in the (x,y) plane (**Fig. 4.8f**). If multiple beads are in the ROI, we only consider the detected circle closest to

the center of the ROI. The algorithm quickly analyses all ROIs and generates a matrix of bead centers relative to the top left corner of the field of view. The piezoelectric stage is moved to bring each bead center near to the optical trap. Multiple fields of view can be stitched together by moving the stepper motor stage. In the next modules, the bead is finely centered in the optical trap, along all three coordinate axes.

Module 2: Line Profile Algorithm for Axial Centering

The bead is brought into focus using a custom line-profile algorithm adapted from a previously described method[10]. Microbead diffraction patterns in brightfield illumination change with axial position relative to the microscope objective plane. Example planes and their corresponding intensity line profiles are shown in **Figure 4.8g-j**. For each grayscale bead image, we compute the mean square error between a line profile through the center of the bead and each of the 111 line profiles extracted from a reference image stack. The reference image stack is a z-series through a reference bead in a hydrogel taken with a 0.05μm step size. The axial position of the reference line scan that minimizes the mean square error is the axial distance between the bead current focal position and true focus. The objective lens is moved by this distance. To compensate for error in the microscope focus motor, this process is repeated iteratively until the axial distance between the bead and true focus is less than 0.05 μm. Typically 3 to 4 iterations are necessary. If the criteria cannot be achieved within 10 iterations, the bead is removed from data analysis.

Module 3: Image Processing Algorithm for Fine 2D Centering

Once a bead is placed into focus by Module 2, its (x,y) position relative to the laser focus can then be optimized by deliberately shifting the focus by exactly 2 μm (empirically determined) and repeating Module 1. The 2 μm shift generates a high contrast bead diffraction pattern, and thus a high contrast line scan. To compensate for errors in stage motion Module 1 is iterated until the

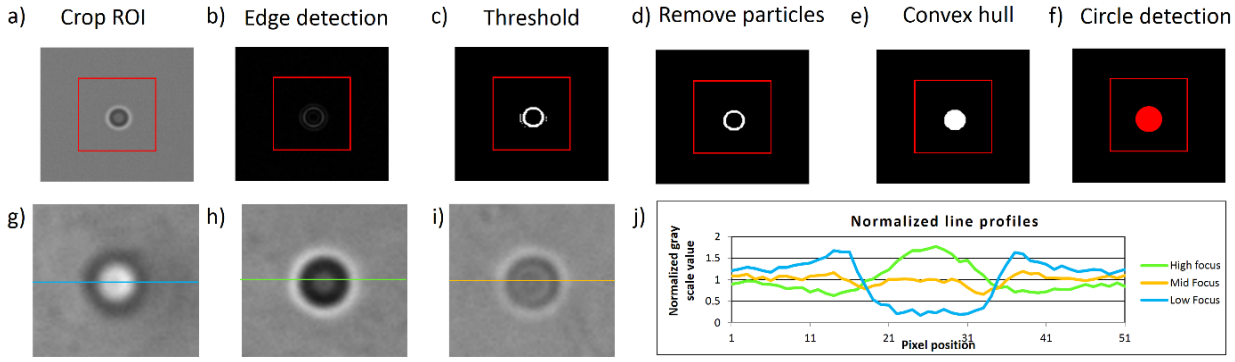

Figure 4.8: Algorithm for c*entering a microbead in the optical trap.* ***(a)*** *First an region of interest is automatically created around each bead (graphically displayed by red box). Then the National Instruments* (NI) *Vision toolkit implements* ***(b)*** *edge detection,* ***(c)*** *binary thresholding,* ***(d)*** *removal of small particles,* ***(e)*** *a convex hull operation and* ***(f)*** *circle detection to determine the bead center coordinates. Centering a bead within the focal plan is accomplished using a custom line-profile algorithm. A line profile through a bead is compared to a reference stack of profiles to determine the focal position of that bead. Representative images of beads below* ***(g),*** *above* ***(h),*** *and at focus* ***(i)*** *are shown along with their normalized line profiles* ***(j)****.*

bead center is at the same pixel location as the laser focus. If the criteria cannot be achieved within 10 iterations, the bead is removed from data analysis.

Module 4: AMR

After centering the bead, AMR and data analysis is performed as described in **Chapter 2**.

4.10 References

1. Paszek, M.J. *et al.* Tensional homeostasis and the malignant phenotype. *Cancer Cell* **8**, 241-254 (2005).
2. Park, J.S. *et al.* The effect of matrix stiffness on the differentiation of mesenchymal stem cells in response to TGF-beta. *Biomaterials* **32**, 3921-3930 (2011).
3. Chaudhuri, O. & Mooney, D.J. Stem-cell differentiation: Anchoring cell-fate cues. *Nature materials* **11**, 568-569 (2012).
4. Young, J.L., Kretchmer, K., Ondeck, M.G., Zambon, A.C. & Engler, A.J. Mechanosensitive kinases regulate stiffness-induced cardiomyocyte maturation. *Sci Rep* **4**, 6425 (2014).
5. Kumar, S. & Weaver, V.M. Mechanics, malignancy, and metastasis: the force journey of a tumor cell. *Cancer Metast Rev* **28**, 113-127 (2009).
6. Legant, W.R. *et al.* Measurement of mechanical tractions exerted by cells in three-dimensional matrices. *Nat Methods* **7**, 969-971 (2010).
7. Gjorevski, N. & Nelson, C.M. Mapping of mechanical strains and stresses around quiescent engineered three-dimensional epithelial tissues. *Biophys J* **103**, 152-162 (2012).
8. Mann, B.K., Gobin, A.S., Tsai, A.T., Schmedlen, R.H. & West, J.L. Smooth muscle cell growth in photopolymerized hydrogels with cell adhesive and proteolytically degradable domains: synthetic ECM analogs for tissue engineering. *Biomaterials* **22**, 3045-3051 (2001).

9. Daley, W.P., Peters, S.B. & Larsen, M. Extracellular matrix dynamics in development and regenerative medicine. *J. Cell Sci.* **121**, 255-264 (2008).
10. Bloom, R.J., George, J.P., Celedon, A., Sun, S.X. & Wirtz, D. Mapping local matrix remodeling induced by a migrating tumor cell using three-dimensional multiple-particle tracking. *Biophys J* **95**, 4077-4088 (2008).
11. Licup, A.J. *et al.* Stress controls the mechanics of collagen networks. *Proc Natl Acad Sci U S A* **112**, 9573-9578 (2015).
12. Sabass, B., Gardel, M.L., Waterman, C.M. & Schwarz, U.S. High resolution traction force microscopy based on experimental and computational advances. *Biophys. J.* **94**, 207-220 (2008).
13. Kniazeva, E. *et al.* Quantification of local matrix deformations and mechanical properties during capillary morphogenesis in 3D. *Integrative Biology* (2012).
14. Tang, Y. *et al.* MT1-MMP-dependent control of skeletal stem cell commitment via a beta1-integrin/YAP/TAZ signaling axis. *Developmental Cell* **25**, 402-416 (2013).
15. Kotlarchyk, M.A. *et al.* Concentration Independent Modulation of Local Micromechanics in a Fibrin Gel. *PLoS One* **6**, e20201 (2011).
16. Velegol, D. & Lanni, F. Cell traction forces on soft biomaterials. I. Microrheology of type I collagen gels. *Biophys J* **81**, 1786-1792 (2001).
17. Mizuno, D., Head, D.A., MacKintosh, F.C. & Schmidt, C.F. Active and Passive Microrheology in Equilibrium and Nonequilibrium Systems. *Macromolecules* **41**, 7194-7202 (2008).
18. Mizuno, D., Tardin, C., Schmidt, C.F. & MacKintosh, F.C. Nonequilibrium Mechanics of Active Cytoskeletal Networks. *Science* **315**, 370-373 (2007).
19. Schultz, K.M., Kyburz, K.A. & Anseth, K.S. Measuring dynamic cell-material interactions and remodeling during 3D human mesenchymal stem cell migration in hydrogels. *Proc. Natl. Acad. Sci. U. S. A.* **112**, E3757-3764 (2015).
20. Nijenhuis, N., Mizuno, D., Spaan, J.A. & Schmidt, C.F. High-resolution microrheology in the pericellular matrix of prostate cancer cells. *Journal of the Royal Society, Interface / the Royal Society* **9**, 1733-1744 (2012).
21. Schultz, K.M. *et al.* Electrospinning covalently cross-linking biocompatible hydrogelators. *Polymer* **54**, 363-371 (2013).
22. Shayegan, M. & Forde, N.R. Microrheological characterization of collagen systems: from molecular solutions to fibrillar gels. *PloS one* **8**, e70590 (2013).
23. Brau, R. *et al.* Passive and active microrheology with optical tweezers. *Journal of Optics A: Pure and Applied Optics* **9**, S103 (2007).
24. Fitzgibbon, J., Morrison, J.J., Smith, T.J. & O'Brien, M. Modulation of human uterine smooth muscle cell collagen contractility by thrombin, Y-27632, TNF alpha and indomethacin. *Reprod Biol Endocrinol* **7** (2009).
25. Ma, X. *et al.* Fibers in the extracellular matrix enable long-range stress transmission between cells. *Biophys J* **104**, 1410-1418 (2013).
26. Winer, J.P., Oake, S. & Janmey, P.A. Non-linear elasticity of extracellular matrices enables contractile cells to communicate local position and orientation. *PLoS One* **4**, e6382 (2009).
27. Tan, J.L. *et al.* Cells lying on a bed of microneedles: an approach to isolate mechanical force. *Proc Natl Acad Sci U S A* **100**, 1484-1489 (2003).
28. Saez, A., Ghibaudo, M., Buguin, A., Silberzan, P. & Ladoux, B.Æ. Rigidity-driven growth and migration of epithelial cells on microstructured anisotropic substrates. *Proceedings of the National Academy of Sciences* **104**, 8281-8286 (2007).
29. Jin, T., Li, L., Siow, R.C. & Liu, K.K. A novel collagen gel-based measurement technique for quantitation of cell contraction force. *J R Soc Interface* **12** (2015).
30. Abhilash, A.S., Baker, B.M., Trappmann, B., Chen, C.S. & Shenoy, V.B. Remodeling of fibrous extracellular matrices by contractile cells: predictions from discrete fiber network simulations. *Biophys. J.* **107**, 1829-1840 (2014).
31. Kraehenbuehl, T.P. *et al.* Three-dimensional extracellular matrix-directed cardioprogenitor differentiation: systematic modulation of a synthetic cell-responsive PEG-hydrogel. *Biomaterials* **29**, 2757-2766 (2008).
32. Liu, J. *et al.* Soft fibrin gels promote selection and growth of tumorigenic cells. *Nat Mater* **11**, 734-741 (2012).
33. Chaudhuri, O. *et al.* Extracellular matrix stiffness and composition jointly regulate the induction of malignant phenotypes in mammary epithelium. *Nat Mater* **13**, 970-978 (2014).

34. Frigault, M.M., Lacoste, J., Swift, J.L. & Brown, C.M. Live-cell microscopy - tips and tools. *Journal of Cell Science* **122**, 753-767 (2009).

Chapter 5

Conclusions

5.1 Summary, conclusions, and implications

AMR has largely been used to characterize the material properties of different fluids and gels[1-4], but only recently extended to measure pericellular stiffness by our lab[5]. I used this technology to first investigate how MT1-MMP WT or KO SSCs isolated from mice interacted with their local ECM (**Chapter 2**). My work led to the discovery that stem cells can control lineage commitment by remodeling their ECM and increasing pericellular stiffness. By doing so, the cells were able to engage β-1 integrins, leading to focal adhesion formation, and activate mechanotransduction effectors such as Rho and YAP. In turn, Rho and YAP affect cellular contractility and transcriptional activity, respectively[6].

Next, I changed directions and focused on how ECM mechanics mediated changes in cellular behavior. In **Chapter 3**, I demonstrated that the asymmetric distribution of ECM stiffness can affect cellular morphology, signaling and invasive potential. Our FEA models provided insight into the likely different force balances in OP and EP that arise from their asymmetric and uniform stiffness distribution, respectively[7]. To determine whether the different stress profiles of acini that resulted from our model had any effect on acini behavior, we analyzed colony geometry, signaling, and phenotype. In the end, the results demonstrated that the asymmetric distribution itself played a dominant role in determining invasive phenotype, colony size, and adhesion mediated signaling, thus supporting the model. The finding that on-top and embedded culture models results in different phenotypes had also manifested itself in **Chapter 2**, where we showed that MT1-MMP

KO SSCs isolated from mice only demonstrated preferential differentiation towards adipogenesis and reduced differentiation towards osteognesis, as found *in vivo*, when embedded within collagen but not when cultured on top of collagen[6]. Embedded models can better recapitulate the 3D environment found in the body because they provide both a chemical and mechanical 3D context. Importantly, the differences observed in OP and EP may cast doubt on previous results and cautions researchers against the OP when trying to recapitulate normal physiological conditions.

The experiments detailed in **Chapter 2** and **Chapter 3** led us to appreciate the importance of cell-ECM interactions, both in terms of tensional homeostasis and pericellular stiffness control. Therefore, in **Chapter 4**, we developed aAMR to better quantify cell-mediated changes to pericellular stiffness. The automated system can quickly make large quantitative stiffness maps in the entire pericellular space, no longer limiting the user to *near* and *far* comparisons. With aAMR we quantified the collaborative role of MMPs and cellular contractility in plastically deforming the matrix[8]. Specifically, MMPs were necessary for locking in changes to stiffness. Additionally, we found that cells could generate a range of stiffness spanning two orders of magnitude within their pericellular space. This observation is especially relevant to the biophysical community because it emphasizes that cell-ECM communication likely relies on the distribution of the ECM stiffness. Yet, many groups still correlate cellular phenotypes with bulk values of ECM stiffness[9-13] without considering its distribution at the micro level. Fortunately, the need to measure both the heterogeneities of the ECM as well as cell-mediated changes to it is now apparent[14, 15]. aAMR fulfills this need that was otherwise not satisfied. Of course, we are still far from understanding how cells process the heterogeneous stiffness distributions around them and utilize the information to make decisions, but with aAMR we can now begin to make such correlations. Importantly, we plan to publish the code along with our results and setup so others can build their own aAMR

systems to study cell-ECM hypotheses that have thus far been limited to qualitative assessments of the ECM mechanics[15, 16].

In conclusion, my dissertation offers new insight into cell-ECM interactions, by establishing that the widely used 3D culture method for breast cancer research can itself bias the resultant phenotypes, by quantifying the contributions of MMP and contractility in changing pericellular stiffness, and by providing tools to the community for accurate measurements of cell-ECM interactions. Additionally, my work highlights the necessity to consider mechanical properties and architecture when working with 3D tissue culture models. For a systems approach to studying cellular processes *in vivo*, we must allow cells to deform and change the matrix as they would *in vivo*. By doing so, we can achieve maximal physiological relevance and be able to study how cells process this stochastic information for decision making in processes like migration direction, branching morphogenesis etc.

5.2 Preliminary studies

Acinar-ECM interactions

Much like aAMR has provided insight into cell-ECM interactions with single cell systems, it can also provide insight for how colonies interact with their ECM. aAMR can be conducted around acini during development to see how cell-ECM interactions change from the single cell phase, the growth phase, the apoptosis phase, and finally the growth arrested phase. Additionally, the same can be done to study disease progression. In fact, aAMR around acini of different phenotypes may reveal signature markers that can predict the final phenotype. For instance, it can be speculated that multi-acinar colonies degrade the matrix in all directions, whereas invasive acini may focus MMP activity to specific area.

Lastly, revisiting OP and EP models to study such interactions may, for instance, provide a useful opportunity to investigate how cell colonies regulate size. There is considerable evidence and conjecture that forces may be used as cues for growth and polarization in organogenesis[17]. For future work, the roles of actin cytoskeleton tension and contractility can be studied in conjunction with pericellular stiffness to determine whether acini in OP grow larger to achieve a level of internal tension similar to EP models.

Nevertheless, AMR measurements made with our 60x TIRFM objective only allow trapping as deep as 40 μm with trap linearity only valid for a 10 μm window (data not shown). Thus, most of the measurements are conducted around 30-35 μm. Acini, on the other hand, can be greater than 100 μm in diameter. Thus, we need to upgrade our aAMR system to trap deeper and with greater range of trap stability. To accomplish this, I switched from the 60x objective to a 40x silicone objective (Olympus). The lower numerical aperture and greater working distance allows for trapping as deep as 150 μm with linear stability over 30 μm. Importantly, with good calibrations factors, the galvanometer values can be shifted at 30 μm increments depending on measurements opening up the entire 150 μm range for measurements. To take advantage of this possibility, we have also added in a functionality to allow users to create measurement z-stacks. As a bonus, the decrease in magnification increases the field of view making it easier to make measurements around the large colonies. Of course, there is a tradeoff. The image processing algorithm had to be made more robust because fewer pixels accounted for a bead. I fixed the image processing algorithm and Mark Keating adjusted the volts to meter calibration as well as the image stitching factors to compile a new version of aAMR. To test the accuracy of the new system, we cycled between 25 beads 3 times in a 2 mg/ml collagen gel and found that the error rate (std/mean) was

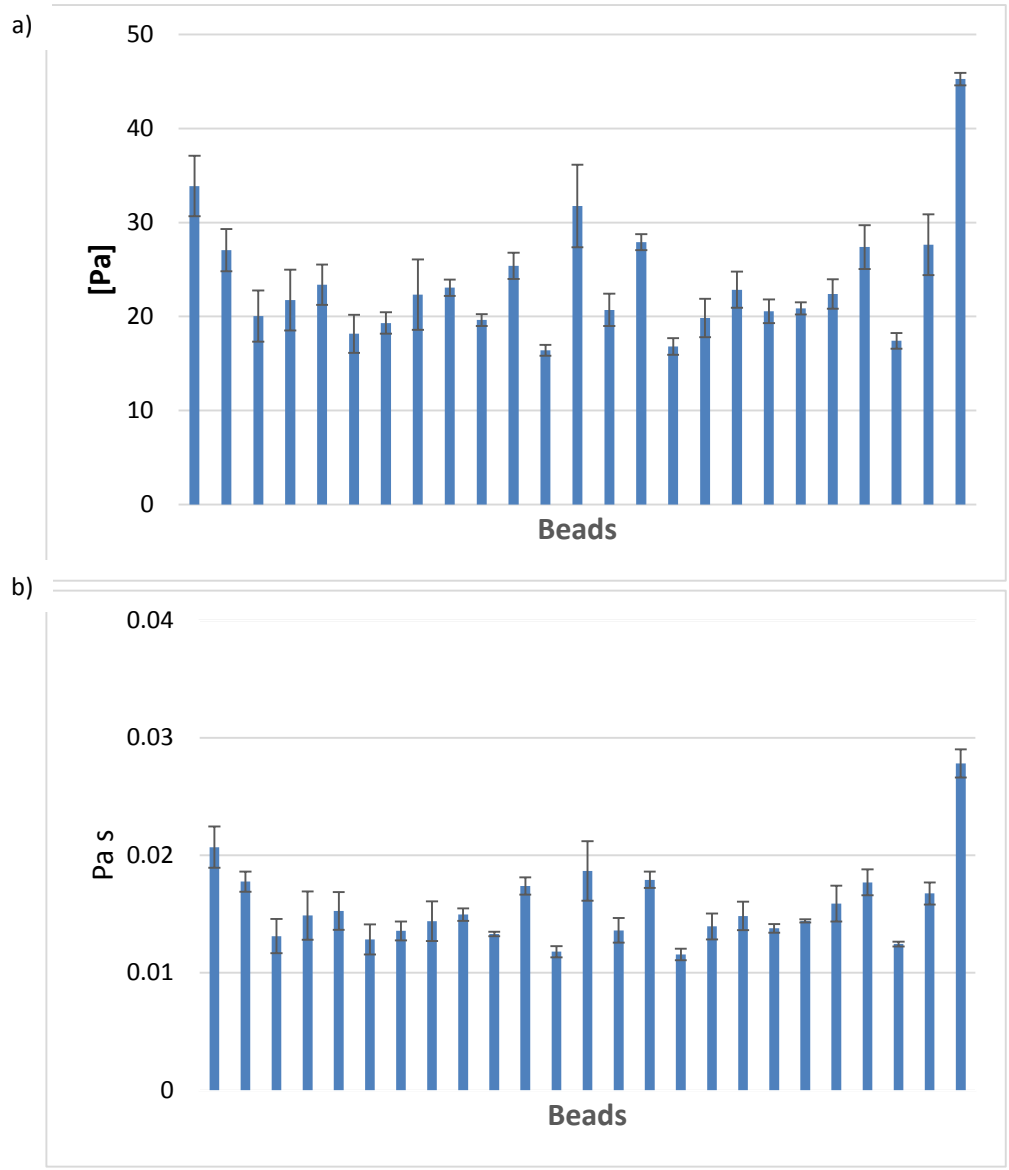

Figure 5.1: *Repeatability of measurements in 40x aAMR.* ***(a)*** *G' and* ***(b)*** *viscosity measurements for 25 beads chosen at random in 2.0 mg/ml collagen gel and separated by at least the range of the piezoelectric x-y stage (~100um). The automation system cycled between the beads three times.*

less than 8% for both G' and viscosity calculations (**Fig. 5.1**). The error rate is comparable to the 5.5% of 60x rheology.

I next conducted a proof of concept by measuring the stiffness distributions around acini on day 7 and day 13 (**Fig. 5.2**). A normal looking acinus was chosen for day 7 to capture the interactions between the cell-ECM during normal development. On day 13, around the time when

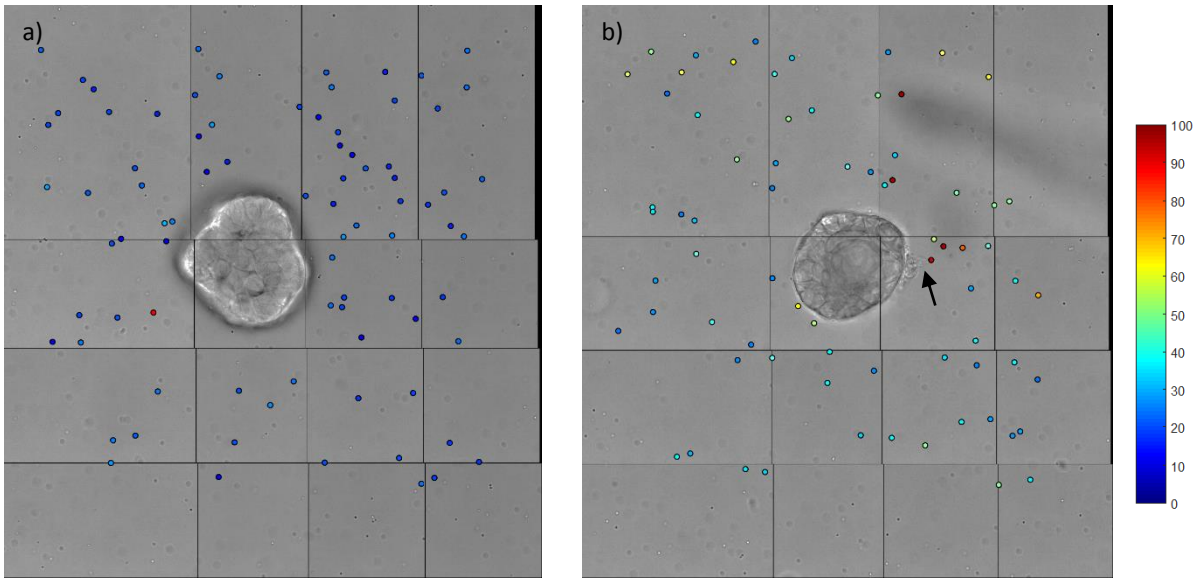

Figure 5.2: *40x aAMR rheology around acini.* ***(a)*** *Beads were measured around acini at* ***(a)*** *day 7 and* ***(b)*** *day 13. Day 13 acini was chosen because of its protrusion (arrow). Beads are pseudo colored based on the G' values according to the color map displayed.*

acini should be growth arrested, an abnormal acinus with a protrusion was selected. aAMR revealed a quiescent relationship between the day 7 acinus and its pericellular matrix (**Fig. 5.2a**), however the abnormal acinus displayed marked heterogeneities (**Fig. 5.2b**). These results show that we can now measure pericellular stiffness around acini and dig deeper into these interactions to learn more about physiological and pathological processes.

Stem cells control of pericellular stiffness

Previously, Engler et al. showed that matrix stiffness alone can drive cell differentiation in 2D conditions and that lineage commitment was dependent on the elasticity of the matrix[18]. Our results agree with these findings but demonstrate that cells can actively change their local stiffness to achieve this. An interesting hypothesis for future work is whether stem cells cultured in 3D matrices and exposed to different fate commitment signals in the media tune their ECM differently to match the physiological stiffness of their specified lineage.

Migration mechanics

How cells migrate in 3D is not well understood. In the past decade, two prominent labs have published conflicting theories on the roles of MMPs in migration. Friedl's lab published that fibrosarcoma cells (HT1080) exhibit a "supramolecular plasticity mechanism in cell migration" [19]. Specifically, they observed that HT1080s could migrate in an MT1-MMP independent fashion by switching from a mesenchymal (spread) morphology to an amoeboid (rounded) one, which can squeeze and propel through existing gaps in the matrix[19]. In contrast, the Weiss lab published a follow up paper showing that HT1080 cell migration was completely abolished with MT1-MMP inhibition and pointed out that the collagen Friedl used was pepsin extracted from bovine dermis[20]. Pepsin extraction causes the removal of collagen telopeptides, which are responsible for interfibrillar crosslinking[21]. Thus, the pore size in pepsin extracted collagen is much larger than the acid extracted rat-tail collagen that Weiss uses, which maintains the ability to form interfibrillar crosslinks like collagen tissue found *in vivo*.

If crosslinking is different, then the mechanical properties of the ECM are also likely different. It stands to reason that the cells may alter their local ECM differently in the different gels. In a preliminary study aimed at understanding whether cell-ECM interactions can unveil the switch between mesenchymal and amoeboid morphologies, we first quantified *G'* in cell free collagen gels that were extracted from the Weiss lab or purchased from BD. Weiss lab collagen was either acid extracted (HM) or pepsin extracted (PEP). BD collagen is also acid extracted, but the complete process of extraction is a trade secret, thus we expected there to be differences in the final gel. The different collagen gels were prepared at 37 °C and exhibited very different mechanical environments (**Fig. 5.3, *black bars***). Additionally, gelation of HM and BD at lower

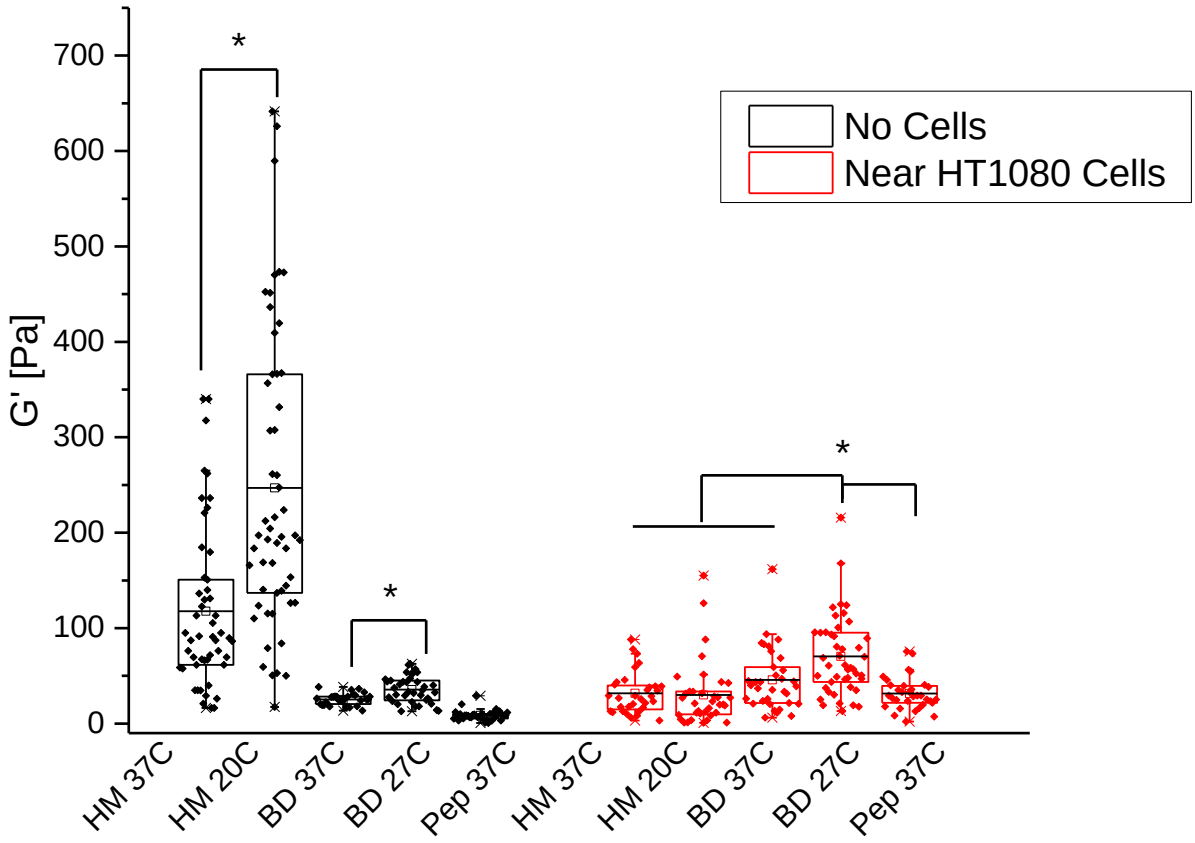

Figure 5.3: *Changes in collagen as a result of temperature, preparation, and HT1080 cell intervention. Collagen was either extracted commercially (BD) or extracted in lab via acid treatment (HM) or pepsin treatment (Pep). aAMR was conducted in cell free 2 mg/ml collagen gels prepared at 37C or at predetermined lower temperatures. Significant differences were observed when gelation temperature was lowered. HM collagens displayed the highest G' values and distribution and Pep collagen the lowest. When aAMR was conducted in the same gels with HT1080 cells, G' values converged to the same G' values, except for the case of BD 27C.*

temperatures (20 °C and 27 °C, respectively) resulted in a significant *G'* increase compared to the higher temperature counterpart.

Fascinatingly, when HT1080 cells were cultured in the same cells, the resulting pericellular rigidity of all the gels was significantly tuned to approximately the same values, with the exception of BD 27 °C (**Fig. 5.3, *red bars***). This result is a beautiful embodiment of the theory of tensional homeostasis[22], and has never been measured in this manner before. The dramatic change in stiffness values is especially of interest considering the architecture is very different across all the conditions (**Fig. 5.4**). Moreover, it seems that cells in different gels use different strategies to tune

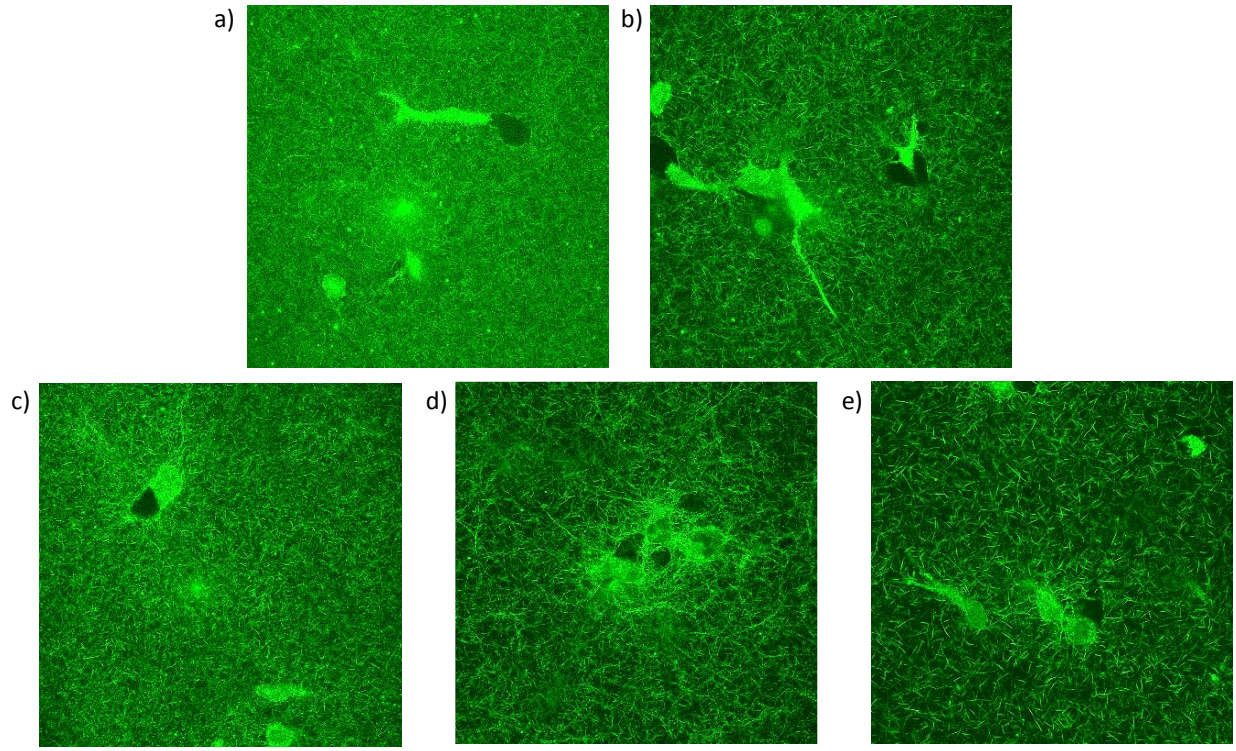

Figure 5.4: *ECM architecture of different collagen gels.* ***(a)*** *HM 37C,* ***(b)*** *HM 27C ,* ***(c)*** *BD 37C,* ***(d)*** *BD 20C,* ***(e)*** *Pep 27C*

their stiffness. For example, whereas gels like HM 20 °C would need to be significantly degraded, gels like PEP 37 °C would have to be considerably stiffened. I speculate the different strategies would require different signaling states and this may be one reason why cells migrate differently. For future work, careful experimentation must be conducted to test this hypothesis and changes in stiffness must be monitored.

Tracking the evolution of pericellular stiffness

In the work presented thus far, cell-ECM interactions were measured at single time points. But, studying the evolution of pericellular stiffness can provide insight into how cell reach and breach homeostasis. For example, consider **Figure 5.5**, where, in collaboration with Dr. Farideh Sabeh of the Weiss lab, I measured pericellular stiffness around fibroblasts isolated from mice that

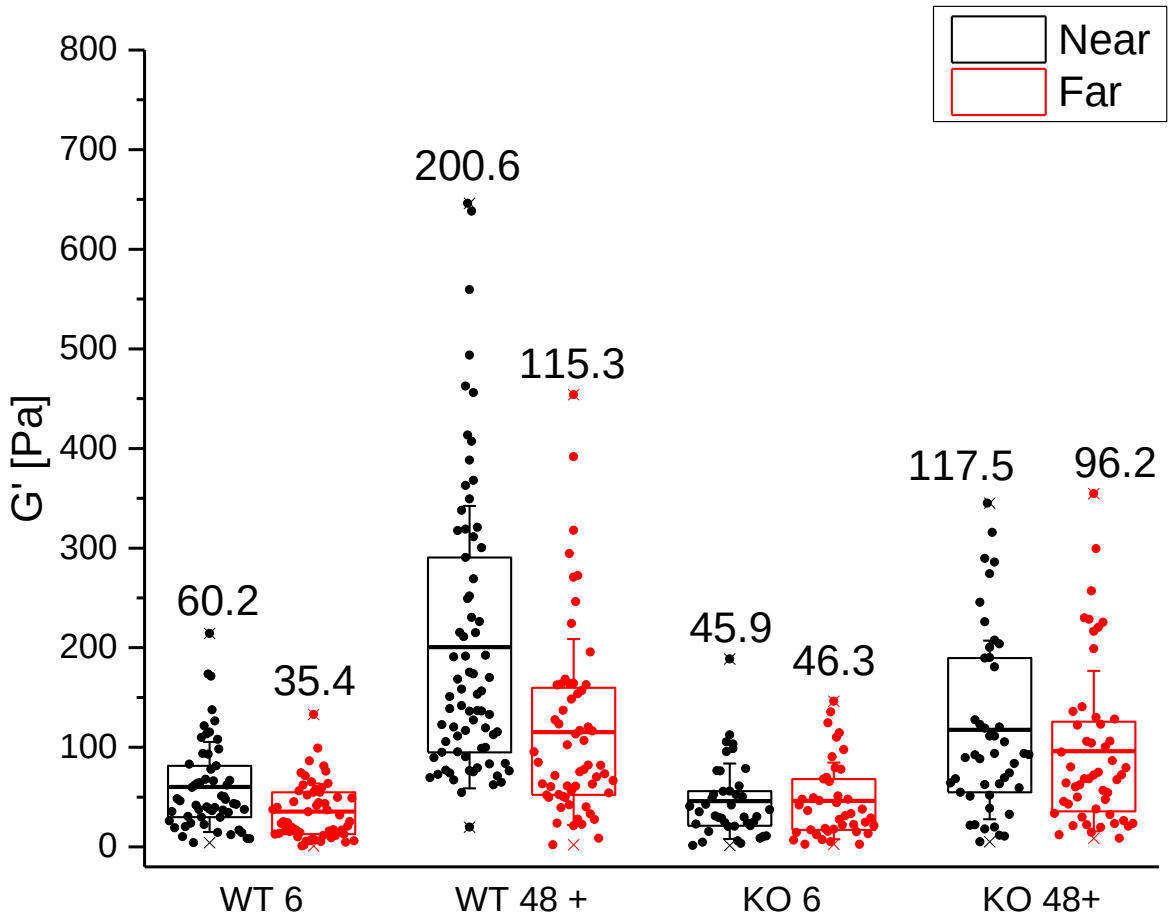

Figure 5.5: *G' measurements in 2mg/ml collagen gels near and far from fibroblast WT or KO for MT1-MMP. Measurements were made at 6 hours or 48 hours.*

were either wildtype (WT_f) or knockout (KO_f) for MT1-MMP with aAMR. These cells were cultured within HM matrices. We performed aAMR *near* and *far*, as before, but this time measurements were made at two time points – 6 hours and 48 hour after gelation. As expected, WT_f cells were able to significantly stiffen the pericellular matrix compared to regions *far* from WT_f after 48 hours. This observation was not mimicked in KO_f cells. However, measurements at the 6 hour time points exposed differences in the evolution of pericellular stiffness. Specifically, both KO_f and WT_f cells significantly stiffened regions *near* and *far* over time. The increase in stiffness in KO_f suggests that the increase is mediated in an MT1-MMP independent manner. Interestingly, the KO_f values *near* and *far* are of similar magnitude as WT_f, which may suggest

that part of the increase in stiffness WT_f is also MT1-MMP independent. Of course, the most likely candidate is contractility, but a thorough analysis of the pericellular space with the addition of pharmacological inhibitors is necessary to investigate further the factors involved.

The evolution of pericellular rigidity can also be measured at shorter time scales to better understand cell migration and mechanical homeostasis in 3D. **Figure 5.6** shows continuous quantification of *G'* for a small set of beads surrounding a single HAoSMC as it *wakes up* in a 2 mg/ml collagen gel with aAMR from the time of gelation. This study serves as a proof of concept and provides a strong example of the utility of such work. Bead trajectories can be tracked overtime and provide inputs for new or simplified mathematical models to calculate traction forces. In future work, measurements can be made around many individual cells with new metrics developed depending on the hypothesis being tested. For example, finding correlations between changes in cell migration direction and the stiffness distribution in those location may hold important

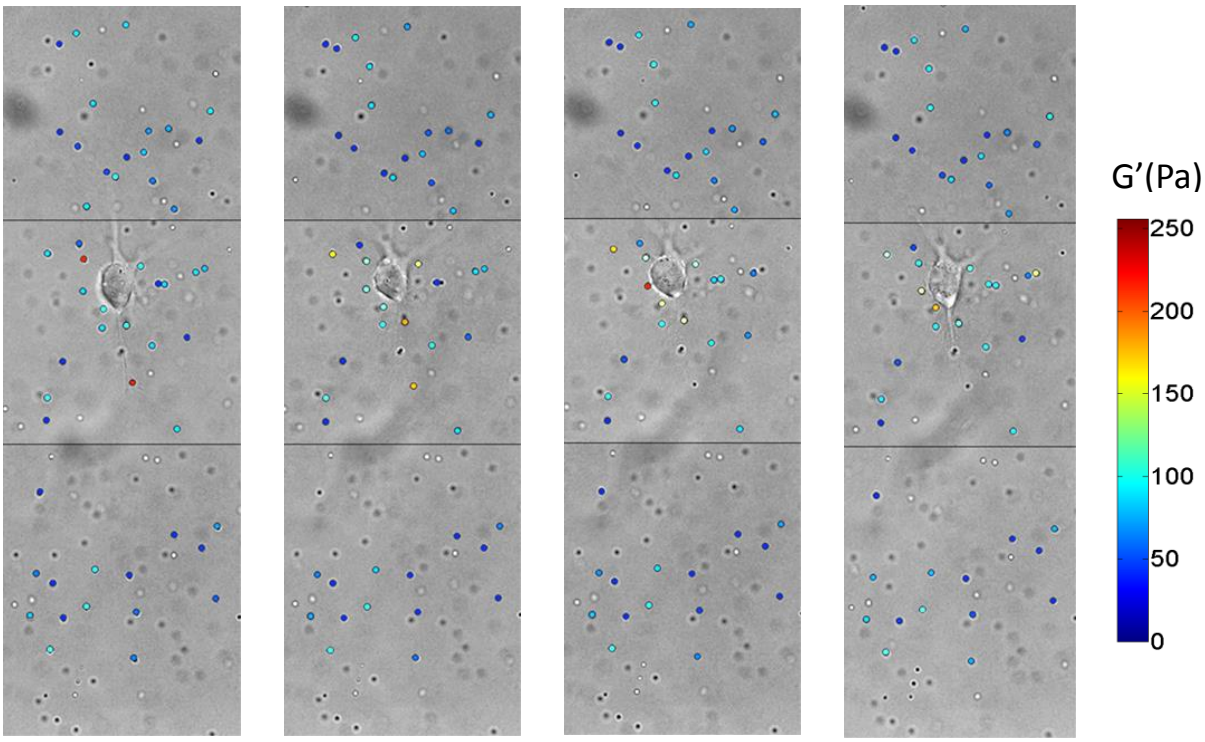

Figure 5.5: *Time lapse measurement of G' around an HAoSMC in 2mg/ml collagen gels. Each frame is approximately one hour apart.*

information. Confocal reflection microscopy can complement these measurements providing information on the fibrous architecture.

5.3 References

1. Mizuno, D., Head, D.A., MacKintosh, F.C. & Schmidt, C.F. Active and Passive Microrheology in Equilibrium and Nonequilibrium Systems. *Macromolecules* **41**, 7194-7202 (2008).
2. Brau, R.R. *et al.* Passive and active microrheology with optical tweezers. *Journal of Optics a-Pure and Applied Optics* **9**, S103-S112 (2007).
3. Choi, S.Q., Steltenkamp, S., Zasadzinski, J.A. & Squires, T.M. Active microrheology and simultaneous visualization of sheared phospholipid monolayers. *Nature communications* **2**, 312 (2011).
4. Shayegan, M. & Forde, N.R. Microrheological characterization of collagen systems: from molecular solutions to fibrillar gels. *PloS one* **8**, e70590 (2013).
5. Kniazeva, E. *et al.* Quantification of local matrix deformations and mechanical properties during capillary morphogenesis in 3D. *Integr Biol (Camb)* **4**, 431-439 (2012).
6. Tang, Y. *et al.* MT1-MMP-dependent control of skeletal stem cell commitment via a beta1-integrin/YAP/TAZ signaling axis. *Dev Cell* **25**, 402-416 (2013).
7. Kurup, A., et al. Novel Inisghts from 3D models: the pivotal role of physical symmetry in epithelial organization. *Sci Rep* (In Review).
8. Kurup, A., Keating, M., Alvarez-Elizondo, M., Botvinick, E. Method to measure pericellular stiffness in natural extracellular matrices. *Proc. Natl. Acad. Sci. U. S. A.* (Submitted).
9. Paszek, M.J. *et al.* Tensional homeostasis and the malignant phenotype. *Cancer Cell* **8**, 241-254 (2005).
10. Karamichos, D., Brown, R.A. & Mudera, V. Collagen stiffness regulates cellular contraction and matrix remodeling gene expression. *Journal of biomedical materials research. Part A* **83**, 887-894 (2007).
11. Haage, A. & Schneider, I.C. Cellular contractility and extracellular matrix stiffness regulate matrix metalloproteinase activity in pancreatic cancer cells. *FASEB J.* **28**, 3589-3599 (2014).
12. Hadjipanayi, E., Mudera, V. & Brown, R.A. Guiding cell migration in 3D: a collagen matrix with graded directional stiffness. *Cell Motil. Cytoskeleton* **66**, 121-128 (2009).
13. Provenzano, P.P., Inman, D.R., Eliceiri, K.W. & Keely, P.J. Matrix density-induced mechanoregulation of breast cell phenotype, signaling and gene expression through a FAK-ERK linkage. *Oncogene* **28**, 4326-4343 (2009).
14. Gjorevski, N. & Nelson, C.M. Endogenous patterns of mechanical stress are required for branching morphogenesis. *Integrative Biology* **2**, 424.
15. Bloom, R.J., George, J.P., Celedon, A., Sun, S.X. & Wirtz, D. Mapping Local Matrix Remodeling Induced by a Migrating Tumor Cell Using Three-Dimensional Multiple-Particle Tracking. *Biophys. J.* **95**, 4077-4088.
16. Schultz, K.M., Kyburz, K.A. & Anseth, K.S. Measuring dynamic cell-material interactions and remodeling during 3D human mesenchymal stem cell migration in hydrogels. *Proc. Natl. Acad. Sci. U. S. A.* **112**, E3757-3764 (2015).
17. Mammoto, T. & Ingber, D.E. Mechanical control of tissue and organ development. *Development* **137**, 1407-1420 (2010).
18. Engler, A.J., Shamik, Sweeney, H.L. & Discher, D.E. Matrix Elasticity Directs Stem Cell Lineage Specification. *Cell* **126**, 677-689.
19. Wolf, K. *et al.* Compensation mechanism in tumor cell migration: mesenchymal-amoeboid transition after blocking of pericellular proteolysis. *J. Cell Biol.* **160**, 267-277 (2003).

20. Sabeh, F. *et al.* Tumor cell traffic through the extracellular matrix is controlled by the membrane-anchored collagenase MT1-MMP. *J. Cell Biol.* **167**, 769-781 (2004).
21. Demou, Z.N. *et al.* Lack of telopeptides in fibrillar collagen I promotes the invasion of a metastatic breast tumor cell line. *Cancer Res.* **65**, 5674-5682 (2005).
22. Provenzano, P.P. & Keely, P.J. Mechanical signaling through the cytoskeleton regulates cell proliferation by coordinated focal adhesion and Rho GTPase signaling. *J. Cell Sci.* **124**, 1195-1205 (2011).